Optical Second Harmonic Generation Measurements for Characterization of Amorphous Silicon Interfaces

by

Long He

B.S., Nankai University (China), 2007

M.S., University of Colorado at Boulder, 2011

A thesis submitted to the

Faculty of the Graduate School of the

University of Colorado in partial fulfillment

of the requirements for the degree of

Doctor of Philosophy

Department of Physics

2014

This thesis entitled:
Optical Second Harmonic Generation Measurements for Characterization of Amorphous Silicon Interfaces
written by Long He
has been approved for the Department of Physics

_____
Prof. Charles T. Rogers

_____
Dr. Charles W. Teplin

Date _____

The final copy of this thesis has been examined by the signatories, and we find that both the content and the form meet acceptable presentation standards of scholarly work in the above mentioned discipline.

He, Long (Ph.D., Physics)

Optical Second Harmonic Generation Measurements for Characterization of Amorphous Silicon Interfaces

Thesis directed by Prof. Charles T. Rogers

Hydrogenated amorphous silicon films (a-Si:H) have a long history of application in opto-electronic devices, in part due to their low cost and compatibility with large area substrates. Recently, crystal silicon/a-Si:H heterojunction(SHJ) photovoltaic cells have demonstrated extremely high open circuit voltages (V_{OC} = 750 mV) and photo-conversion efficiencies (24.7%). In SHJ PVs, the amorphous-crystalline silicon (a-Si:H/c-Si) interface is the critical aspect of the device to optimize for high efficiency. The understanding of defects and transport at the a-Si:H/c-Si junction has been slow to develop due to a dearth of optoelectronic measurements able to distinguish the unique interface physics from effects in the bulk a-Si:H and c-Si volumes.

Optical second harmonic generation (SHG) has been extensively used to selectively characterize surfaces and interface in a variety of materials, including semiconductors. In SHG experiments, interfaces and surfaces can be probed selectively: One focuses a pulsed laser beam (frequency ω) onto the sample and detects second harmonic light (frequency 2ω) generated at optically accessible surfaces and interfaces in the sample. SHG elucidates the important interface properties because the bulk "background" is mostly forbidden by symmetry in cubic and amorphous materials, leaving only interface contributions.

In this thesis, I have demonstrated that SHG is a sensitive tool for probing strong electric field present in the 10 nm a-Si:H layer in SHJ solar cells. To study the electric-field induced SHG (EFISH) in a-Si:H, we measure SHG from ITO/a-Si:H/ITO sandwich structures at different biases and polarization geometries. In this "simple" structure, we quantitatively separate interface SHG and EFISH. We also directly probe carrier dynamics in the depletion region of a ITO/a-Si:H junction with time-resolved optical second-harmonic generation. Through fitting of the time-resolved SHG

data and current data simultaneously, we are able to show that slow carrier dynamics that are visible in the device current are actually taking place within the ITO/a-Si interfacial region. In summary, SHG is proven to be a promising diagnostic method to characterize the interface electrostatics and charge transport at the amorphous silicon interfaces.

Dedication

This thesis is dedicated to

my parents, whose affection and love made who I am.

my wife, whose gives me a home.

my grandpa, who taught, inspired me and guided me to physics.

my father, the closest friend to me, a soul lives in my mind.

Acknowledgements

Seven years, Boulder, Physics. It is easy to cover this period in graduate school with a few words if anyone asks after. But, it takes me years to remember every moments through this journey. At the end of this journey, I want to thank all those who helped me.

One paragraph is definitely not enough to express my appreciation to my advisors, Chuck Rogers and Chaz Teplin. I bet Chuck is the most humorous physicist in the department. He taught me how to think as a physicist, how to build as an engineer. It is his patient guidance help me grow from student to an experimental physicist. Chaz Teplin is my secondary advisor. I can not imagine finishing this project without his support. His unselfish support rendered me countless resources and opportunities in the solar cell community. Chuck and Chaz are not only my teachers, but also my best friends in Boulder. What is more, I would also want to thank my colleagues in Chuck's lab, Joshua Montague, Jason Gray, Jack Houlton and Ke Zhao. They make our lab a warm family.

People in Physics department also help me a lot. I need to thank Jixia Dai and Eddie Calleja in McElory group for helping my problems. I want to thank my classmates, Hsiang-sheng Ku, Jianfeng Xie, Yue Cao, Ke Ke, Shuming Li, Edwin Widjonarko, Will Kindel, Jeanne Hallow... I can not list all your names here. I felt so lucky for being able to meet you guys at this wonderful place. I would also like to thank my friends I met in CU past and now, Hongyu Zhou, Chengyuan Ding, Pai Wang, Qi Hu, Geruo A, Jianhua Cheng, Yuchen Zhang, Yacheng Sun... Thank you for the good time we have spent together. Thank you for making my life in Boulder a unique memory.

I want to thank my grandpa, Junyu He, an earnest physicist who has guided me into the world of physics. I would like to specially thank my wife, soul mate, Ruo Du. It is her to support

me through some most difficult time in my life. Finally and importantly, I want to acknowledge my parents for their continuous support and love every now and then. None of my achievements is possible without you.

Contents

Chapter

Tables

Table

Figures

Figure

Chapter 1

Introduction

1.1 Interfaces in silicon solar cells: relevant to both amorphous and crystal silicon heterojunction solar cells

A photovoltaic cell (also called solar cell) is an electrical device that converts the energy of light directly into electricity by the photovoltaic effect. The photovoltaic effect was first discovered and experimentally demonstrated by French physicist A. E. Becquerel as early as 1839 [1, 2]. When the light is incident upon the device, the electrons present in the valence band absorb energy and are excited. They jump to the conduction band and create electron-hole pairs or excitons. Then the electron-hole pairs are separated by the spatial electric field present in the device. The separated charges can generate and support an current flow in an external circuits without being attached to any external voltage source. By far, the most prevalent bulk material for solar cells is crystalline silicon. In these device, charges are separated by electric fields associated with p-n junctions. Figure 1.1 shows the picture of a typical monocrystalline solar cell. Its p-n junction is formed by diffusion of dopants creating a spacial charge region separating the excited electron-hole pairs(see Figure 1.2).

While numerous PV materials have been tested, those that rely on silicon have inherent advantages: silicon is abundant, non-toxic and supported by mature manufacturing technology. The existing knowledge base for silicon allows PV research to focus only on aspects specific to PV, as material properties related to computer chips, memories and display technologies have already been addressed in the scientific literature. Generally, solar cells must generate charge carriers by

Figure 1.1: A solar cell made from a monocrystalline silicon wafer with contact grid [3].

Figure 1.2: The spacial charge region diagram for the p-n junction inside a monocrystlline silicon solar cell [4].

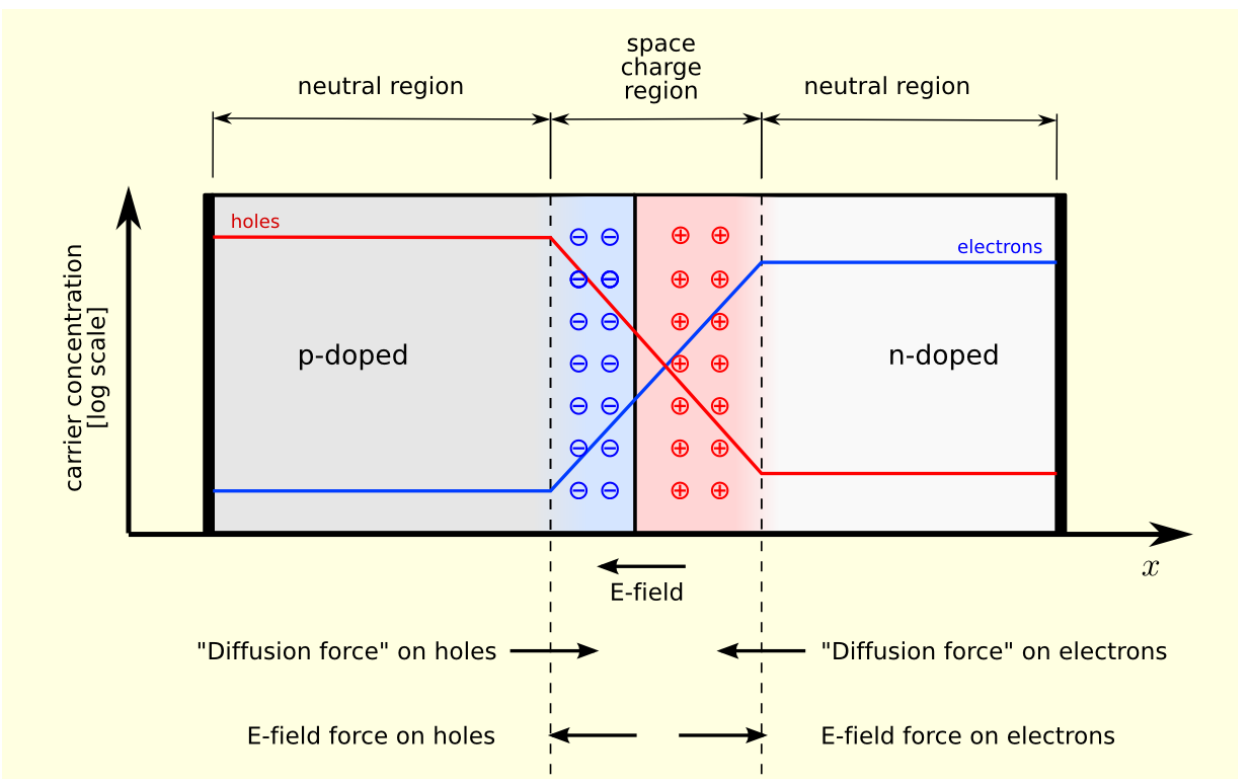

optimal absorption of the spectrum of the sun. At the same time, these excess charge carriers need to be efficiently collected with minimal recombination on their way to the terminals of the device. A bare silicon surface has many dangling silicon bonds that act as free charge carrier recombination centers due to the discontinuous lattice structure. High recombination rates at the top surface can degrade V_{OC} dramatically. Lowering the surface recombination is typically accomplished by reducing the number of dangling silicon bonds at the top surface by using a passivating layer. The best known passivation layer in the electronics industry is thermally grown silicon dioxide layer for low defect states at the interface [5]. Since this passivating layer is an insulator, any region which has an ohmic metal contact cannot be passivated using silicon dioxide. A spiky metal through the passivation layer is usually made between the emitter metal and the absorber material to provide channels for carrier extraction. Recombination at the metal/silicon contacts remains the efficiency limitation for the c-Si solar cell. A doping structure around the emitter can be achieved to minimise this recombination, but the manufacture cost increase for this design is not tolerable [6].

The silicon heterojunction(SiHJ) is the ideal solution to replace the silicon dioxide passivation layer by simultaneously fulfilling the passivation and contacting roles [6, 7]. It separates highly recombination-active ohmic contacts from the crystalline surface by insertion of a passivating, semiconducting film with a wider bandgap. Thin-film hydrogenated amorphous silicon (a-Si:H) of a few nanometers thickness is a suitable material for SiHJ because the amorphous silicon bandgap is slightly wider than that of c-Si and it can be doped relatively easily. The first a-Si:H/c-Si heterostructures were studied in 1974 by Fuhs [8]. As early as 1991 [9, 10], the major breakthrough for SiHJ solar cell came with the introduction of a thin buffer layer of undoped a-Si:H between doped emitter and wafer, the so-called Heterojunction with Intrinsic Thin-layer (HIT) structure, to reduce the interface state density. Since about 2000, research accelerated and has deepened the fundamental knowledge about this structure [11, 12, 12, 13]. Figure 1.3 shows a typical HIT solar cell structure diagram. The thin intrinsic and doped amorphous silicon layers are deposited between the c-Si wafer and ITO layer on both side of the cell. This bifacial design provide effective passivation for surface dangling bond on the both side of the c-Si wafer. Meanwhile, the build-in electric

field around the heterojunction of c-Si/a-Si:H provides field effect passivation by electrostatically shielding the charge carriers from the interface [14, 15]. The thickness of a-Si:H layers is optimized for resistivity so that charge carriers pass through this a-Si:H layer fast enough to avoid carriers recombining before being collected. Therefore, this a-Si:H buffer layer could be considered as a semi-permeable membrane for carrier extraction [16].

The HIT solar cell was developed, commercialized and patented by Sanyo Electric Company. By the end of 2013, Sanyo claimed a 24.7% world efficiency record for such solar technology with a record high V_{OC} (750mV) [17], and this efficiency also features the highest record for silicon based solar cell of large area ($> 100cm^2$). While the c-Si wafer accounts for a large portion of the raw material cost, this record solar cell is based on a wafer only 98 μm thick, thereby saving about half of the cost of the current industrial standard for diffused-junction solar cells. Another major advantage of the HIT solar cell is that the deposition processing of a-Si:H layers saves thermal manufacturing budget by requiring much lower temperature ($< 200°$) than the silicon oxidization process($> 800°$) of diffused-junction solar cells. Sanyo has commercialized 235 Watt photovoltaic modules of a remarkable 18.3% conversion efficiency built on 72 individual HIT solar cells of 21.1% efficiency. Figures 1.3 and 1.4 show the structure diagram for the HIT solar cell and a actual picture of Sanyo's HIT photovoltaic module on the market [17, 18].

Overall, the HIT solar cell is a low-cost, promising technology of high conversion efficiency solar cells. The key to the success of HIT solar cell is the intrinsic a-Si:H/c-Si interface. It is crucial for improving the cell efficiency by reducing recombination losses at the hetero interface between a-Si and c-Si and optimization of the thicknesses in a-Si layers. Therefore, it provoked our interest to employ interface-sensitive optical Second Harmonic Generation to study this critical interface.

1.2 Second Harmonic Generation (SHG) for interface characterization

After the invention of the laser, the high intensity monochromatic light source, optical harmonic generation is first demonstrated by Franken et al. in 1961 by focusing a ruby laser into a quartz sample [19]. Soon afterwards, SHG was observed on the surface of inversion-symmetric

Figure 1.3: Heterojunction with Intrinsic Thin-layer (HIT) solar cell structure diagram. a-Si:H($i/n+/p+$) indicated the hydrogenated amorphous silicon of various doping type: "i" — intrinsic type or non doping; "$n+$" — heavily n-type doping; "$p+$" — heavily p-type doping. c-Si(n) means the n-type doped crystalline silicon wafer [17].

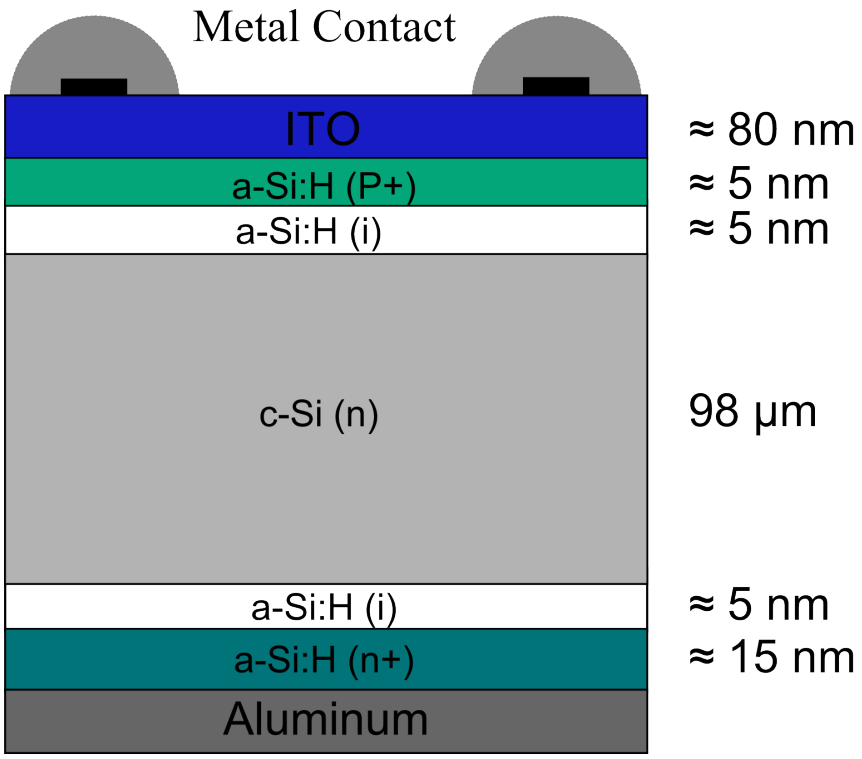

Figure 1.4: Picture of Sanyo's HIT photovoltaic 235 Watt module featuring 18.3% conversion efficiency consisting of 72 individual HIT solar cells of 21.1% efficiency. Demenstion: $1580mm \times 812mm \times 35mm$; Weight: 15 kg [18].

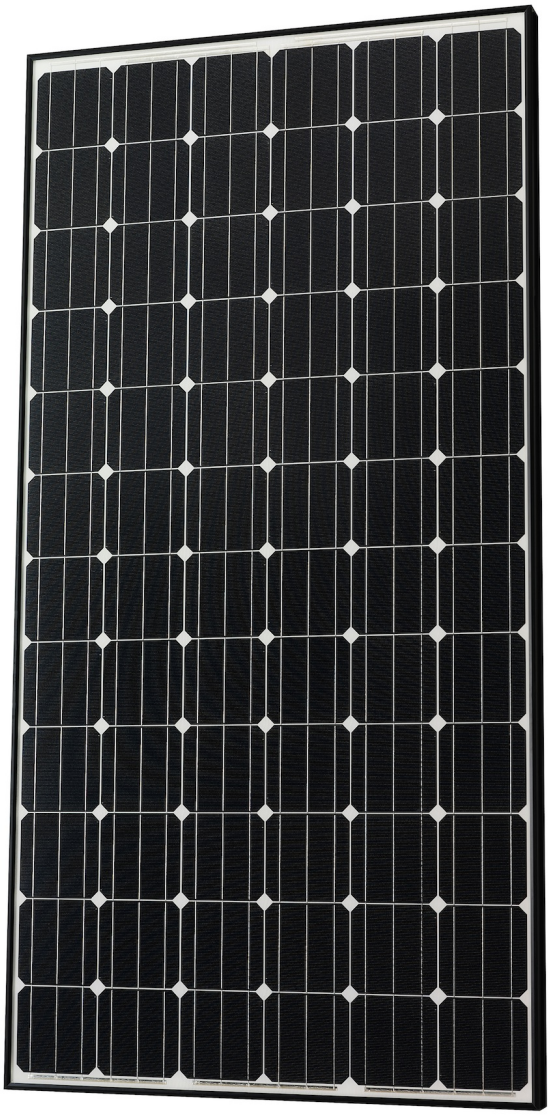

material, silver surface, in 1965 by Brown et al. [20]. Theoretical work was started by Bloembergen and Shen in 1966 by introducing the gaseous plasma model (free electron gas model) [21]. In 1982, the submonolayer sensitivity of SHG is demonstrated by Heinz and Shen by using SHG to probe molecular monolayers adsorbed to surfaces [22]. The capability of SHG as a surface-specific tool was fully studied by Shen and Richmond et al [23, 24, 25] in late eighties.

Second harmonic generation (SHG) is a nonlinear optical process and a special case of sum frequency generation, in which photons of frequency ω interacting with a nonlinear material generate new photons with twice the energy, and therefore twice the frequency 2ω. SHG, as an even-order nonlinear optical effect, is only allowed in media with broken inversion symmetry, which typically happens at the material surface or interface. Therefore, SHG is particularly useful for probing interfaces between media with inversion symmetry. In comparison with stimulated Raman gain techniques, SHG is superior with simpler experimental arrangement and much stronger output signal [26]. Surface second harmonic generation (SSHG) is usually observed when light of frequency ω is reflected off of surface or interface and SHG photons are detected in the reflected beam (see Figure 1.5).

From the point view of quantum mechanics, the SHG processes can be visualized by system energy-level diagrams and by considering the interaction between medium and photons. Figure 1.6 shows that two photons of the same frequency ω are absorbed by the excited states and a photon of frequency 2ω is simultaneously re-emitted in a quantum-mechanical relaxation process. The horizontal solid line represents the system ground state and dashed lines represent the virtual excited states. The SHG process can also be interpreted by treating the dipoles as classical oscillators. When light travels through dielectric matter, the electric field of the light imposes an oscillating force on the electric dipoles in the media. At low light intensity, the dipoles respond linearly to the driving force of light field and re-radiate the electric magnetic wave of the same frequency. The potential vs placement curve is then nearly parabola as indicated in left panel of Figure 1.7. However, when coherent light of high intensity is incident, the dipoles no longer respond linearly to the strong electric field and participate in anharmonic oscillation. The potential energy curve

Figure 1.5: Surface second harmonic generation schematically experimental diagram. The Material A and B are all inversion symmetric medium. The SHG photons are produced at the surface and interface.

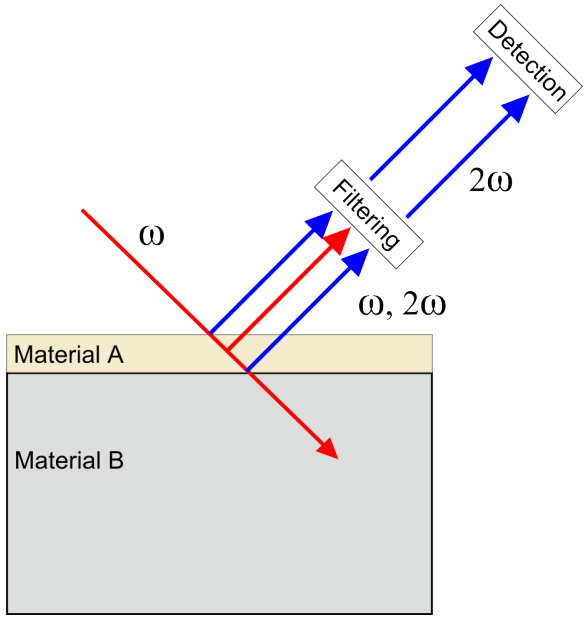

shape deviates from a parabolic bowl (mid and right panel of Figure 1.7). When the displacement from balance position is far, the potential of dipole is influences by its neighbor atoms. Therefore, the deviation of the energy curve from a perfect parabola depends on the lattice structure of the material itself. The mid and right panel of Figure 1.7 illustrate the potential deviation for two group of lattice structures: those with a center of symmetry (centrosymmetric) and those without (non-centrosymmetric). Now we can decompose the dipole polarization $P(t)$ in to the Fourier series:

$$\boldsymbol{P}(t) = \sum_{n=0}^{\infty} \boldsymbol{P}^{(n\omega)} \mathrm{e}^{in\omega t} \tag{1.1}$$

here, the $P^{(n\omega)}$ term would result in the nth order harmonic radiation, among which one would find the double frequency term (2ω) is zero for the system with inversion symmetry [27]. However, this term will be non-zero for interfacial atomic layers where the inversion symmetry is violated. In the nonlinear response of interfacial atomic layer, the asymmetry of the anharmonic dipole contributes to the doubled frequency signal in the reflected general polarization wave. This property makes SHG a promising surface probing tool for inversion symmetric materials. This second order harmonic process can be described by a non-linear tensor $\overset{\leftrightarrow}{\chi}$ convolving with the input light field. The properties of this tensor will be further discussed in the following chapter.

$$\boldsymbol{P}^{(2\omega)} = \chi^{(2)} : \boldsymbol{E}^{(\omega)} \boldsymbol{E}^{(\omega)} \tag{1.2}$$

Though the inversion symmetry violation at the surface or interfaces is commonly known to be responsible for optical SHG, a strong bulk electric field can also break the symmetry in the centrosymmetric materials, and produce bulk electric-field-induced SHG (EFISH) [29, 30, 31, 29]. EFISH was discovered by Lee [32] as early as 1967. EFISH allows for a contactless detection of internal electric fields, which can either be applied static fields or electric fields in semiconductor space-charge regions arising from interfacial charge separation. For example, the effect of EFISH has been used to study charge trapping and photo induced charge trapping in the c-Si/SiO2 system

Figure 1.6: Energy level diagram for second harmonic generation from quantum mechanics point of view.

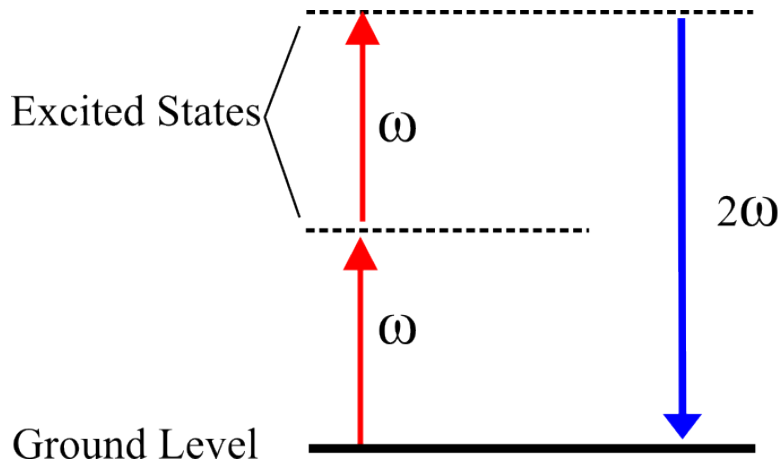

Figure 1.7: The response of different optical materials to an applied electric field varies with field strength and molecular structure [28].

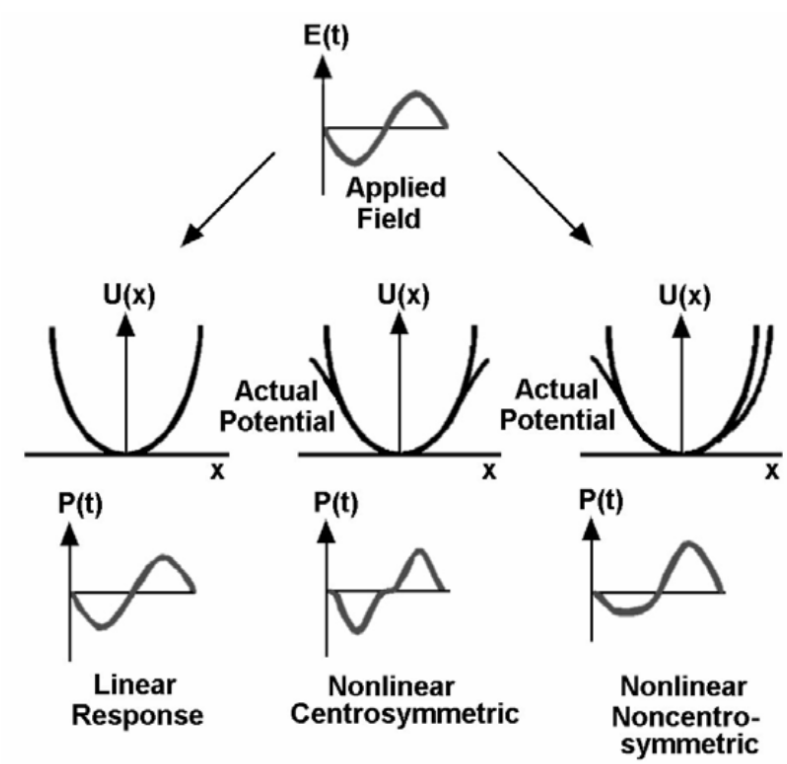

[33, 34, 35, 36, 37, 38]. Since the electric field provides the broken inversion symmetry which is necessary for SHG re-radiation, there is a linear relationship between the electric field strength E^{DC} and the second-order nonlinear susceptibility $\chi^{(2)}$, i.e. $\chi^{(2)} \propto E^{DC}$. Therefore, the re-radiated SHG field is proportional to the internal static electric field strength. This process can be viewed as a nonlinear process governed by a third-order nonlinear susceptibility as given by:

$$\boldsymbol{P}_{DC}^{(2\omega)} = \overset{\leftrightarrow}{\chi}^{(3)}(-2\omega;\omega,\omega,DC) : \boldsymbol{E}^{(\omega)}\boldsymbol{E}^{(\omega)}\boldsymbol{E}^{DC} \tag{1.3}$$

$\overset{\leftrightarrow}{\chi}^{(3)}$ is a third-order tensor describing the coupling between the electric field produced by the incident light $\boldsymbol{E}^{(\omega)}$ and the static electric field $\boldsymbol{E}^{DC}$ present in the media. In most semiconductor structures, there is a built-in electric field due to charges trapped at the defect centers or trap sites at the interface. Therefore, the measured SHG signal is often a superposition of the SSHG and EFISH. As a result, accurate interpretation of SHG signals requires careful separation of EFISH and interface contributions. For example, Rumpel [39] and Gielis [40] et al. use spectroscopic EFISH signatures in c-Si to qualitatively separate EFISH from other SHG signatures. In this thesis, we will focus on how SHG can be used to study the electric fields near the interfaces of a-Si:H, where bulk electric fields break the inversion symmetry and produce bulk electric-field-induced SHG (EFISH).

In comparison with the long history of EFISH, Current-Induced Second Harmonic Generation (CISH) is a newly discovered phenomenon of the inversion symmetry break as the result of an external electrical direct current (DC). Though this is not a topic covered by this thesis for completeness, I briefly introduce here. For the SHG study on complicated semiconductors, the SHG from interfaces, EFISH and CISH are all possible contributions in the total SHG signal. Therefore, in order to achieve more detailed quantitative description, it is necessary to incorporate and interpret any possible SHG sources when dealing with the complicated SHG signal. CISH is firstly introduced during the discussion about the CISH contribution to the nonlinear polarization for a direct band semiconductor by Khurgin in 1995 [41]. The CISH polarization can be quantified in a similar manner to the electric field induced SHG and given by: [42]

$$\boldsymbol{P}_{DC}^{(2\omega)} = \overset{\leftrightarrow}{\chi}^{(3)}(-2\omega;\omega,\omega,DC) : \boldsymbol{E}^{(\omega)}\boldsymbol{E}^{(\omega)}\boldsymbol{j}^{DC} \tag{1.4}$$

where $\boldsymbol{j}$ is the current density and $\overset{\leftrightarrow}{\chi}^{(3)}_{ijkz}$ is the dipole current-induced optical susceptibility. For direct semiconductors,CISH second-order susceptibility arises from an asymmetry of the electron quasi-pulse distribution which leads to a sharp resonance in the vicinity of the local Fermi level for majority carriers in the conduction band [42]. The first experimental observation of CISH in silicon is enabled by Aktsipetrov in 2009 [43]. Shortly afterward, more researchers made effort to understand the CISH in various material systems, including GaAs [44], spin currents [45] and graphene [46, 47, 48] etc. The detection scheme can be applied in a wide range of materials with different electronic band structures. Also, this phenomenon can be used for a real-space image of current density in semiconductor devices. CISH is a exciting new branch of non-linear optics field, becoming more and more popular in the semiconductor and graphene research community, and it could be a possible direction to explore using the current set up in Chuck's lab.

1.3 Motivation for this work

A common theme among next-generation photovoltaic technologies will be the importance of interfaces. Absorber layer thicknesses in all of these technologies are decreased in order to reduce material and deposition equipment costs. This leaves a high ratio of surface to bulk material, increasing the importance of surfaces. Mixed-phase materials are also becoming common and have high internal surface areas important to performance. Finally, nanoscale quantum dots used to exceed the Shockley-Queisser efficiency limit in third generation PV will inevitably be imbedded in a matrix, with enormous surface-to-volume ratios [49, 50]. Passiviation of these internal surfaces will be a critical need. While numerous PV materials have been tested, those that rely on silicon have inherent advantages: silicon is abundant, non-toxic and supported by mature manufacturing technology. We therefore begin our second harmonic generation studies of PV interfaces with the silicon heterojunction that is based on the c-Si/a-Si:H interface. This model system is critical to

present and future photovoltaic devices.

The potential of heterojunction contacts to solar cells was first described by Yablonovitch in 1985 [51], but its potential was realized in silicon only in the late 1990s, through the work of Sanyo Corp. As I described above, Sanyos HIT-cell has exploited the excellent passivation of crystal silicon by hydrogenated amorphous silicon to produce an easily manufactured 24.7% wafer-based solar cell. However, the underlying physics of passivation and of transport through the c-Si/a-Si:H heterojunction remains poorly understood. There have been successful microscopy studies that demonstrated the importance of an abrupt interface phase junction (i.e., immediate a-Si:H growth, with no local regions of epitaxy) for high voltage solar cells [52, 53], a careful examination of the dependence of surface recombination velocity at the heterojunction on a-Si:H deposition temperature and its annealing [12, 54] and an infra-red study that revealed much about hydrogen configurations in the first few a-Si:H monolayers deposited [55]. But attempts to measure the energies and densities of interface states in the electronic bandgap have been inconclusive [56] and even the factors controlling the widely-varying measurements of valence and conduction band offset are unknown. Clearly, an interface-sensitive probe is needed to unravel these mysteries.

The c-Si/a-Si:H heterojunction will play prominent roles in advanced film crystal silicon devices and in nanocrystalline (nc-Si:H) layers used in multi-junction amorphous silicon based devices. Wafer replacement film crystal silicon technology is under intense research at NREL [57]. The goal of wafer replacement silicon is to achieve wafer-like efficiencies at area costs comparable to low-cost a-Si:H. In wafer-replacement PV devices, only enough epitaxial crystal silicon is grown to enable adequate light absorption (5-20 μm), eliminating the immense material waste in wafer-based PV. For such devices, a-Si:H/c-Si heterojunctions are ideal for emitter formation and surface passivation because they efficiently use valuable epitaxial silicon.

Nanocrystalline silicon (nc-Si:H) is being used as a low-gap partner in high-efficiency multi-junction amorphous silicon based devices. Typical nc-Si:H material is comprised of 10-100 nanometer crystallites surrounded by thin amorphous tissue. Because of their nanoscale, the interface at the surfaces of the crystallites must play a crucial role in determining the materials surprisingly

good material properties. Improved knowledge of the a-Si:H/c-Si interface is needed to better understand this material.

The amorphous/crystalline interface will also play a key role in new nano-structured silicon materials, where <10 nm sized crystallites are embedded in an amorphous insulator in order to profit from quantum size effects such as an increase in the silicon band gap and multi-exciton generation. Because this material could be combined with single crystal silicon to make high-efficiency multi-junction devices, numerous researchers have initiated projects to fabricate and characterize nanoscale crystallites in an amorphous matrix. In such structures, the a-Si:H/c-Si:H interface will be key to a long recombination time for photogenerated carriers and to efficient carrier transport between crystallites.

Another potential target for interface specific characterization by SHG is organic photovoltaics. For example, many groups are targeting nanostructured inorganic materials filled with organic semiconductors in order to overcome the short exciton diffusion lengths in the organic absorbers. The interface is enormous and plays the critical role of separating the exciton into individual charge carriers. NREL group has contributed to studies of planar and nanostructured a-Si:H/polymer whose results showed a critical dependence upon the offset between the a-Si:H valence band edge and the polymer HOMO level [58]. There remain critical questions about the nature of this and other organic-inorganic and also about many organic-organic semiconductor interfaces in PV.

Interface optimization will be key to the successful development of the above materials. Unfortunately, techniques for measuring interface properties are currently limited because existing characterization tools are dominated by the bulk response. Our research will tackle this problem by developing SHG for characterizing the semiconductor interface properties relevant to PV. The ideal characterization of a semiconductor interface would reveal the density of interface traps, the trap distribution within the band gap, and the detrapping time that it takes carriers to be released. The standard technique for mid-gap defect measurements is deep level transient spectroscopy (DLTS). Indeed, DLTS measurements on silicon heterojunctions have been made at NREL. However, the

DLTS signal is sensitive to midgap defects in the bulk as well as the surface and the large number of defects in the bulk a-Si:H layer dominate the DLTS measurement. The bulk sensitivity has prevented successful DLTS interface measurements.

In comparison with DTSL, SHG could be the ideal tool for characterizing the semiconductor interface properties relevant to PV. A challenge with SHG, however, is that it does not measure an electronic signal directly. Rather, it measures changes through their affect on $\chi^{(2)}$. Thus, it is necessary to correlate changes in $\chi^{(2)}$ to the properties of interest. An advantage of SHG is that the relative changes in $\chi^{(2)}$ as the interface is altered are often large, even though the absolute signal intensity is very small. This thesis presents the correlated changes in $\chi^{(2)}$ with the local electric field perpendicular to the interface (E_z), and demonstrate the sensitivity of $\chi^{(2)}$ to the interface physics and shows how SHG measurement can provide insight into device operation.

1.4 Thesis outline

The remainder of the thesis is organized in the following structure. In Chapter 2, I will discuss the theory background for SSHG for isotropic materials and Electric Field Induced SHG. Chapter 2 will also present the experimental set up for SHG measurement and the Stokes optics theory for polarization information extraction. In Chapter 3 and 4, the interference theory for the SHG signal from the HIT solar cell device and ITO/a-Si:H interface will be illustrated. In Chapter 5, I will develop the new experimental system for SHG dynamics measurement, and an innovative method combining the Current-Voltage and SHG-Voltage measurement will be introduced. Chapter 6 is the summary of the thesis, and I will summarize the EFISH results for a-Si:H interfaces. Some of the preliminary SHG measurements for Organic Photovoltaic(OPV) device will also be introduced here. Finally, continuation experiments will be suggested.

Chapter 2

Surface Second Harmonic Generation (SSHG) Theory and Experiment

2.1 SSHG and EFISH theory

In this section, I will go through the general theory of surface second harmonic generation for surface and interface. The governing tensor elements and restrictions imposed by the symmetry of an isotropic interface for this nonlinear process will be discussed. Next, I will introduce the Electric Field Induced Second Harmonic (EFISH) theory. Finally, I will discuss the EFISH in Schottky junctions as a special case which is crucial to understand the SHG signal presented in Chapters 4 and 5.

2.1.1 SSHG theory

The surface second harmonic response is governed by the second order non-linear polarization $P^{(2\omega)}$. This polarization represents the dipole moment per unit surface area at the surface or interface.

$$\boldsymbol{P}^{(2\omega)} = \chi^{(2)} : \boldsymbol{E}^{(\omega)}\boldsymbol{E}^{(\omega)} \tag{2.1}$$

Since the incident electric fields and the surface polarization can be decomposed in any of three orthogonal directions of a Cartesian coordinate system, we write:

$$P_i^{(2\omega)} = \chi_{ijk}^{(2)} : E_j^{(\omega)} E_k^{(\omega)} \tag{2.2}$$

where i, j, and k can be any of the Cartesian directions x, y, or z The re-radiated second harmonic fields can be expressed in terms of the polarization s and p, where p-plane is defined in Figure 2.1 and s-plane is perpendicular to p-plane. We assume the p polarization plane lies in x-z plane in Cartesian coordinate system, and the s polarization direction is coincident with y axis. With the re-radiation factors "R", the second harmonic field will be:

$$E_s^{(2\omega)} = R_y P_y(2\omega) \tag{2.3a}$$

$$E_p^{(2\omega)} = R_x P_x(2\omega) + R_z P_z(2\omega) \tag{2.3b}$$

In Equation (2.2), $\chi_{ijk}^{(2)}$ is a third-rank tensor which describes the second-order nonlinear optical susceptibility of the material in Cartesian coordinate system. The i, j, and k can be any of the three orthogonal directions $\hat{x}$, $\hat{y}$, $\hat{z}$. For example, the tensor element $\chi_{xyz}^{(2)}$ convolving with electric field in y and z directions can produce a surface second harmonic polarization in the x-direction. Hence, $\chi_{ijk}^{(2)}$ consists of 3 by 3 by 3, total 27 elements. If we write this complex 3 dimensional tensor in a deformed 2-D matrix, it can list each element as:

$$\chi_{ijk}^{(2)} = \begin{pmatrix} \chi_{xxx}^{(2)} & \chi_{xxy}^{(2)} & \chi_{xxz}^{(2)} & \chi_{xyx}^{(2)} & \chi_{xyy}^{(2)} & \chi_{xyz}^{(2)} & \chi_{xzx}^{(2)} & \chi_{xzy}^{(2)} & \chi_{xzz}^{(2)} \\ \chi_{yxx}^{(2)} & \chi_{yxy}^{(2)} & \chi_{yxz}^{(2)} & \chi_{yyx}^{(2)} & \chi_{yyy}^{(2)} & \chi_{yyz}^{(2)} & \chi_{yzx}^{(2)} & \chi_{yzy}^{(2)} & \chi_{yzz}^{(2)} \\ \chi_{zxx}^{(2)} & \chi_{zxy}^{(2)} & \chi_{zxz}^{(2)} & \chi_{zyx}^{(2)} & \chi_{zyy}^{(2)} & \chi_{zyz}^{(2)} & \chi_{zzx}^{(2)} & \chi_{zzy}^{(2)} & \chi_{zzz}^{(2)} \end{pmatrix} \tag{2.4}$$

The tensor elements describe the SHG process and depends upon the symmetry system of the material. For example, the nonlinear response of the medium cannot distinguish the mathematical ordering of the input fields. This intrinsic requirement results in the permutation symmetry of $\chi_{ijk}^{(2)} = \chi_{ikj}^{(2)}$ which would decrease the 27 tensor elements to 16 independent elements. By such reasoning, we can determine the required number of elements in $\chi_{xyz}^{(2)}$.

We now consider the case of an incoming p-polarized light interacting with an isotropic surface. We establish the relative coordinate system with $\hat{z}$ as the surface normal and the film lying in the xy-plane as illustrated in Figure 2.1. The $\hat{x}$ axis is chosen that the incident light is

Figure 2.1: Schematic of p-polarized light interacting with an isotropic film surface resulting in the generation of second harmonic radiation. The relevant coordinate system is established with $\hat{z}$ as the surface normal and the film lying in the xy-plane. Notice that rotations about the z-axis and reflections through planes containing $\hat{z}$ will leave the system unchanged.

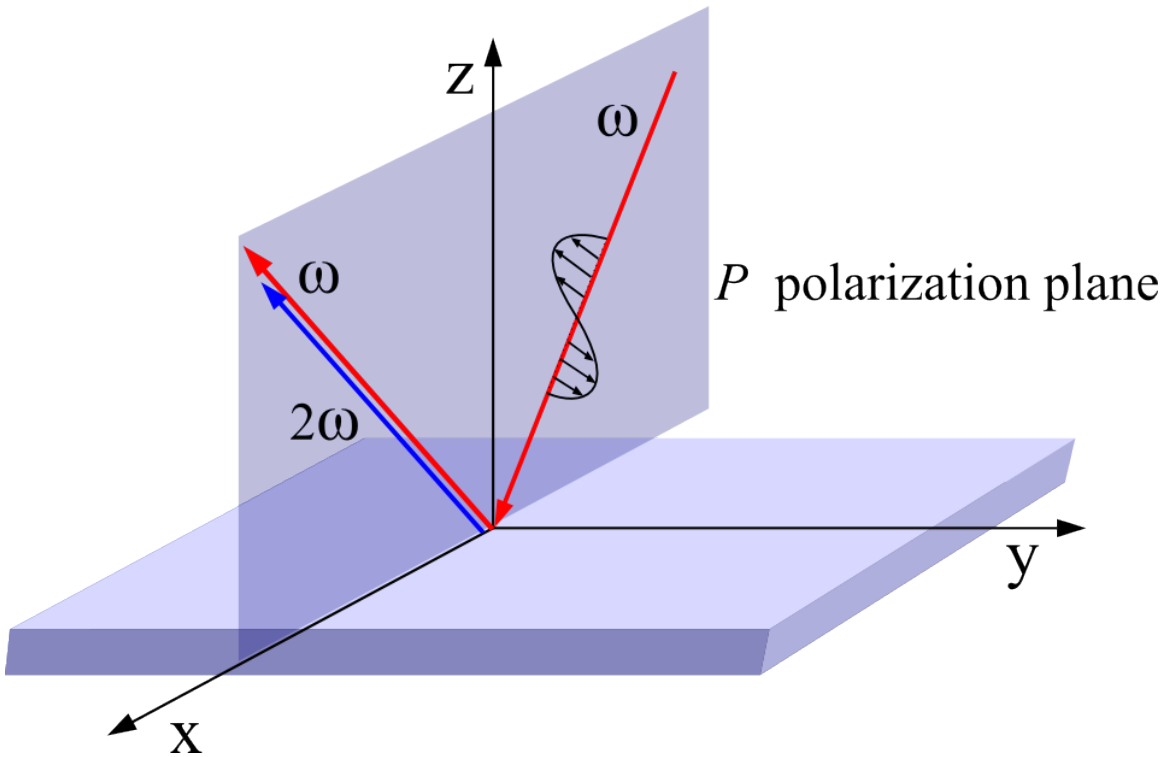

in the x-z plane. The reflection of the second harmonic generation beam is also in the x-z plane. Because of the assumed isotropic structure, a rotation of any angle about the surface normal ($\hat{z}$ axis) will yield the same SHG signal. Similarly, the SHG process should maintain unchanged after mirror transformation with respective to any plane involving z axis. For example, $\chi^{(2)}_{xyz}$ becomes $-\chi^{(2)}_{xyz}$ after the reflection through yz-plane. The unchanged SHG process demands $\chi^{(2)}_{xyz} = -\chi^{(2)}_{xyz}$ yielding $\chi^{(2)}_{xyz} = 0$. After considering the rotational and mirror transformation, the number of non-zero tensor elements is further decreased to 7, with only 3 of with are independent value. Therefore, the SHG surface polarization can be simplified to:

$$\begin{pmatrix} P^{(2)}_x \\ P^{(2)}_y \\ P^{(2)}_z \end{pmatrix} = \begin{pmatrix} 0 & 0 & \chi^{(2)}_{xxz} & 0 & 0 & 0 & \chi^{(2)}_{xzx} & 0 & 0 \\ 0 & 0 & 0 & 0 & 0 & \chi^{(2)}_{yyz} & 0 & \chi^{(2)}_{yzy} & 0 \\ \chi^{(2)}_{zxx} & 0 & 0 & 0 & \chi^{(2)}_{zyy} & 0 & 0 & 0 & \chi^{(2)}_{zzz} \end{pmatrix} \begin{pmatrix} E_xE_x \\ E_xE_y \\ E_xE_z \\ E_yE_x \\ E_yE_y \\ E_yE_z \\ E_zE_x \\ E_zE_y \\ E_zE_z \end{pmatrix}$$
$$= \begin{pmatrix} 2\chi^{(2)}_{xxz}E_xE_z \\ 2\chi^{(2)}_{yyz}E_yE_z \\ \chi^{(2)}_{zxx}E_xE_x + \chi^{(2)}_{zyy}E_yE_y + \chi^{(2)}_{zzz}E_zE_z \end{pmatrix} \tag{2.5}$$

with $\chi^{(2)}_{xxz} = \chi^{(2)}_{xzy} = \chi^{(2)}_{yyz} = \chi^{(2)}_{yzy}$, $\chi^{(2)}_{zxx} = \chi^{(2)}_{zyy}$ and $\chi^{(2)}_{zzz}$ are 3 undependable variables.

The polarizations of the input laser and output SHG light is one of the most important aspects in the SHG experiment. The different input laser polarizations can selectively excite different groups of tensor elements. According to the relative coordinate system indicated in Figure 2.1, the

s polarization corresponds to the y direction, while the p polarization consists of the electric field in x and z direction. From Equation (2.5), the only tensor elements that contribute to s-polarized SHG are $\chi^{(2)}_{yyz}$ and $\chi^{(2)}_{yzy}$, and they can be only active for mixed p and s-polarized input. For p-input polarization, only p-polarized second harmonic is produced by exciting three families of tensor elements $\chi^{(2)}_{xxz} = \chi^{(2)}_{xzx}$, $\chi^{(2)}_{zxx}$ and $\chi^{(2)}_{zzz}$. For s-input polarization, $\chi^{(2)}_{zyy}$ is the only tensor element been excited to produce the p-polarized second harmonic radiation in this geometry. This element also has terms contributed by the medium bulk SHG contribution which I describe next.

When solving the boundary value problem (see Chaz's thesis [59]), we would notice that quadrupolar contributions to the reradiated second harmonic light from nonlinear currents in the bulk of the material cannot be ignored. It leads to the bulk-term "γ" mixing in an indistinguishable manner with the surface terms $\chi^{(2)}_{ijk}$ during the SHG process. The bulk contributions to SHG signal becomes contamination when using surface SHG as a tool for interface diagnosis. Therefore, distinguishing the bulk and surface proportions of the total SHG signal become a important topic for interface study [26, 60, 61]. After taking this bulk term γ into account, the effective tensor elements for SHG polarization at the interfacial system would be:

$$\chi^{(2)}_{\parallel} \equiv \chi^{(2)}_{xxz} = \chi^{(2)}_{xzy} = \chi^{(2)}_{yyz} = \chi^{(2)}_{yzy} \tag{2.6a}$$

$$\chi^{(2)}_{\perp} \equiv \chi^{(2)}_{zzz} + \frac{\epsilon^{\star}_{2\omega}}{\epsilon_{2\omega}} \frac{i\gamma}{2\omega} \tag{2.6b}$$

$$\chi^{(2)}_{bulk} \equiv \frac{\epsilon_{2\omega}}{\epsilon^{\star}_{2\omega}} \chi^{(2)}_{zxx} + \frac{i\gamma}{2\omega} = \frac{\epsilon_{2\omega}}{\epsilon^{\star}_{2\omega}} \chi^{(2)}_{zyy} + \frac{i\gamma}{2\omega} \tag{2.6c}$$

where $\epsilon_{2\omega}$ is the dielectric function of the bulk material for 2ω light, and the $\epsilon^{\star}_{2\omega}$ is the average of dielectric function of the two materials on the two side of the interface where the SHG photons originate. I follow the name system developed by the precedent in this lab, Chaz Teplin [59], to rename independent tensor elements to ""$\chi^{(2)}_{\parallel}$", "$\chi^{(2)}_{\perp}$" and "$\chi^{(2)}_{bulk}$". This name system is derived for the SHG analysis for Aluminum surface. In order to maintain the terminology in Chuck's lab, we will still continue the same style as before. Here, $\chi^{(2)}_{\perp}$ is to indicate that this element is primarily from surface contributions oscillating perpendicular to the surface. $\chi^{(2)}_{\parallel}$ is to indicate that they

contribute to currents oscillating parallel to the surface. $\chi^{(2)}_{bulk}$ means this term is dominated by the bulk contribution.

2.1.2 Electric Field Induced Second Harmonic Generation (EFISH)

SHG is primarily a sensitive probe to study the interface, because it is forbidden in a bulk of a media with inversion symmetry. However, strong electric fields in the bulk can break the inversion symmetry and produce electric-field-induced SHG (EFISH). This phenomenon was discovered by Lee [32] and has been studied in various materials and devices [62, 30, 63, 64, 29, 65]. Numerous researchers have used EFISH to study near-surface electric fields in crystalline Si [29, 30, 31, 66, 67]. In SHG studies of semiconductor structures where electric fields are present, accurate interpretation of SHG signals requires careful separation of EFISH and interface contributions. For example, Rumpel [39] and Gielis [40] et al. use spectroscopic EFISH signatures in c-Si to qualitatively separate EFISH from other SHG signatures.

For an incident electromagnetic wave with electric field component, $E(\omega)$, at frequency ω, and with an additional constant electric field, E_z^{DC}, normal to the sample surface, EFISH can be viewed as a third order nonlinear process which is governed by third order tensor elements:

$$P_i^{(2\omega)} = \overset{\leftrightarrow}{\chi}{}^{(3)}_{ijkz}(-2\omega;\omega,\omega,DC) : E_j^{(\omega)} E_k^{(\omega)} E_z^{DC} \tag{2.7}$$

where z is the direction of the sample surface normal and $\overset{\leftrightarrow}{\chi}{}^{(3)}$ is the tensor that describes the third-order nonlinear response of the material. For z-directed dopant profiles and applied fields, the combination of $\overset{\leftrightarrow}{\chi}{}^{(3)}$ and the integral over E_z^{DC} behaves as an effective second harmonic tensor, $\chi^{(2)}_{EFISH}$, that operates only where E_z^{DC} is non-zero. $\chi^{(2)}_{EFISH}$ has the same three families of non-zero elements that describe SHG from the interfaces of cubic and amorphous materials [60].

The EFISH originates from the overlapping region of the beam path and the bulk electric field, and it is necessary to account for the summation and interference effect over this region. Akstipetrov et al. [30, 29] wrote the EFISH re-radiated electric field as integral over the infinitesimals in the effected region, according to:

$$E^{(2\omega)}_{EFISH,i} \sim \sum_{jk} \chi^{(3)}_{ijkz} E^{(\omega)}_j E^{(\omega)}_k \int \mathrm{e}^{[i(2k_{\omega,z}+k_{2\omega,z})z]} E^{DC}_z(z) dz \tag{2.8}$$

where $k_{\omega,z}$ and $k_{2\omega,z}$ are the z components of the wave vector at the probe and SHG frequencies in the bulk material, respectively.

2.1.3 EFISH from Schottky barrier

In solar cells, the transparent conducting layer is often deposited in contact with absorber layers to collect the excited charge carriers. This kind of contact is also present in HIT solar cell structures. ITO/a-Si:H is the last interface for the excited carrier to pass through before contributing the external current. When ITO is brought into contact with a-Si:H, the charge around the interface is forced to redistribute to bring the two Fermi energies in the two materials into alignment. The space charge in the ITO layer remains very close to the contact due to the high carrier concentration in the material. But the space charge region extends much farther in the amorphous silicon because of the low density of states in the band gap. According to the classical semiconductor textbook treatment [68, 69], this metal/semiconductor junction is usually described by Schottky physics. Because the EFISH induced by the strong electric field of the space charge region in ITO/a-Si:H junction could be a significant part of the total SHG signal for the following experiment, we will assume electric field profile in ITO/a-Si:H junction resembles Schottky physics and deduce the EFISH response for a Schottky junction.

Figure 2.2 shows a schematic diagram of a metal Schottky contact on a semiconductor. In the panel (a), the seperated metal and semiconductor have different work functions Φ_M and Φ_S. In the panel (b), when the materials are brought into contact, the Fermi energies in the two materials must be aligned by the transfer of charge from one one side of the interface to the other. The space charge layers around the interface introduce the band bending. This band bending develops only a few angstroms in the metal due to the high density of free electrons, while it can extend much further in the semiconductor(panel (b)). The potential barrier seen by electrons in the metal trying to pass through the interface is defined as Schottky Barrier Φ_{bn} with:

Figure 2.2: Schematic diagram of a Schottky barrier between metal and semiconductor, showing the charged depletion region in semiconductor, for the cases of (a) separated, (b) electrical contacts with no bias, (c) reverse biased, (d) forward biased [70].

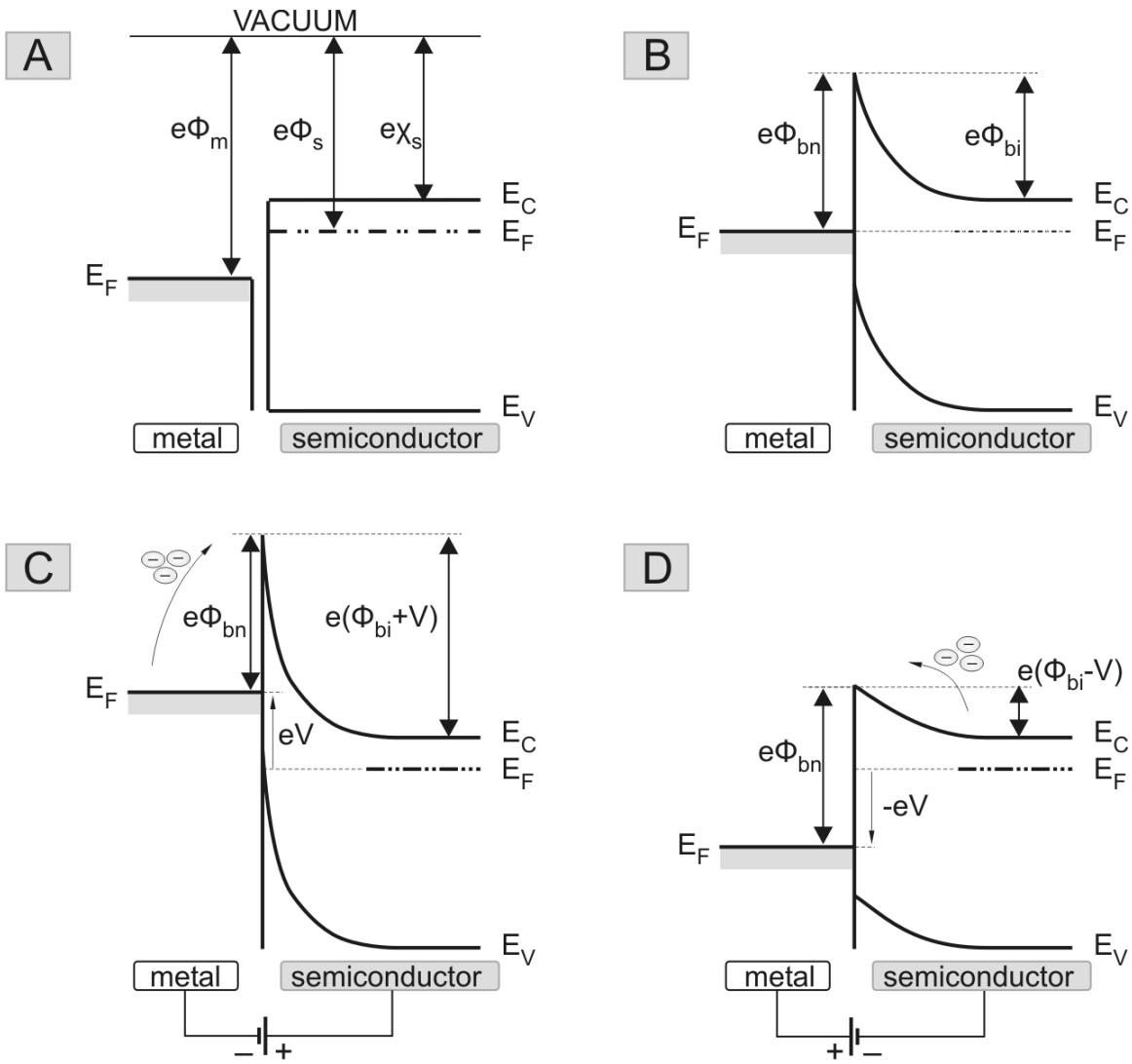

$$\Phi_{bn} = \Phi_m - \chi \tag{2.9}$$

where χ is the semiconductor electron affinity. In the reverse bias condition (panel (c)), a negative voltage V is applied to the metal with respect to the semiconductor, the semiconductor-to-metal barrier increases. In the forward bias condition(panel (d)), a positive voltage is applied to the metal with respect to the semiconductor and the semiconductor-to-metal barrier decreases allowing electrons to move easily from the semiconductor into the metal. However, ϕ_{bn} remains constant for those two conditions [71, 69].

In the semicondutor, the built-in potential barrier Φ_{bi} is the extra energy needed by the electrons in the conduction band trying to move into the metal:

$$\Phi_{bi} = \Phi_{bn} - \frac{E_c - E_F}{e} \tag{2.10}$$

where e is the electron charge.

The depletion region in the semiconductor is the area of particular interests for EFISH study because of the space charge induced the strong high electric field in this region. In order to understand the electric field profile, we can start from deriving the potential of the depletion layer $V(x)$ by solving the Poisson's equation:

$$\frac{d^2V(x)}{dx^2} = -\frac{\rho(x)}{\epsilon\epsilon_0} \tag{2.11}$$

where $\rho(x)$ is the space charge density in the depletion region. It arises from the ionization of band gap states by the band bending. We introduce the full depletion approximation which assumes that the semiconductor is fully depleted and the density of ionized states N_D is uniform over the depletion region. This approximation results a constant ρ in the depletion region. Hence, the solution to Equation (2.11) is:

$$V(x) = \frac{eN_D(W-x)^2}{2\epsilon\epsilon_0} \tag{2.12}$$

where the width of the depletion layer W is

$$W = \left[\frac{2\epsilon\epsilon_0(V_A + V_B)}{eN_D}\right]^{\frac{1}{2}} \tag{2.13}$$

Next, we can write down the electric field profile $E(x)$ by finding the derivative of $V(x)$:

$$E(x) = \frac{eN_D(x - W)}{\epsilon\epsilon_0} \tag{2.14}$$

The electric field profile has a linear relationship with the distance x from the physical border of metal and semiconductor(see Figure 2.3). The physical origin for this linear profile is the uniform charge density in the depletion region.

Figure 2.3: The electric field profile as a function of the distance in the direction of interface normal for a Schottky junction. We notice that the electric field is almost screened out in the metal, and the strength of the electric field peaks at the interface between the metal and semiconductor and only extend into the semiconductor bulk.

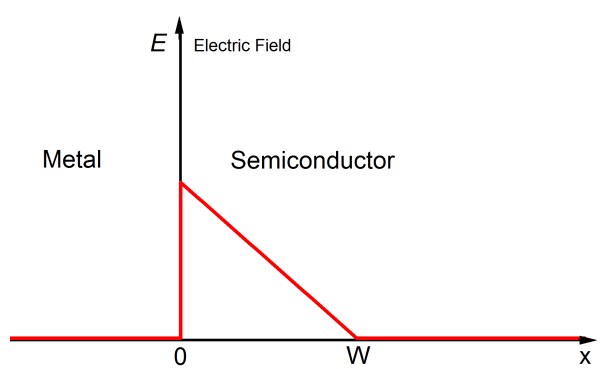

Now, we can calculate the EFISH from the depletion region in a-Si:H, by starting from the integral term in Equation (2.8). The algebra can be greatly simplified by ignoring the phaser term $e^{[i(2k_{\omega,z}+k_{2\omega,z})z]}$ for the a-Si:H samples and specific laser wavelength. This is because the a-Si:H layer strongly absorbs 410 nm SHG photons (penetration depth λ ~30 nm [72]). Therefore, the phase variation in EFISH originating area is less than 30°. Therefore, the interference effect and the phase term in the integral can be ignored within tolerated error, and the integral can be written

as:

$$E^{(2\omega)} = \int_{z=0}^{z=W} \frac{eN_D(x-W)}{\epsilon\epsilon_0} \mathrm{e}^{-\frac{z}{\lambda}} \tag{2.15}$$

After some algebra, we are able to work out the integral:

$$E^{(2\omega)} \propto -\frac{eN_D}{\epsilon\epsilon_0}[\lambda W - \lambda^2 + \lambda^2 \mathrm{e}^{-\frac{W}{\lambda}}] \tag{2.16}$$

When $\lambda \ll W$, the above result will become

$$E^{(2\omega)} \propto -\frac{eN_D}{\epsilon\epsilon_0} W^2 [\frac{\lambda}{W} - \frac{\lambda^2}{W^2}(1 - \mathrm{e}^{-\frac{W}{\lambda}})] \approx -\frac{eN_D}{\epsilon\epsilon_0}\lambda W \tag{2.17}$$

When $\lambda \gg W$, the above result will become

$$E^{(2\omega)} \propto -\frac{eN_D}{\epsilon\epsilon_0}\lambda^2 [\frac{W}{\lambda} - 1 + \mathrm{e}^{-\frac{W}{\lambda}}] \approx -\frac{eN_D}{2\epsilon\epsilon_0} W^2 \tag{2.18}$$

In the actual experiment, instead of the SHG light field($E^{2\omega}$), the SHG photon counts intensity ($I^{2\omega}$) is obtained by Photomultiplier Tube. It holds a relationship with $E^{2\omega}$ via $I^{2\omega} = |E^{2\omega}|^2$. After taking Equation (2.13) into account, the $I^{2\omega}$ for the above cases will be:

$$\text{For } \lambda \ll W \qquad I^{(2\omega)} \propto (-\frac{eN_D}{\epsilon\epsilon_0}\lambda W)^2 = \frac{\sqrt{2}eN_D}{\epsilon\epsilon_0}\lambda^2 (V_A + V_B) \tag{2.19}$$

$$\text{For } \lambda \ll W \qquad I^{(2\omega)} \propto (-\frac{eN_D}{2\epsilon\epsilon_0} W^2)^2 = (V_A + V_B)^2 \tag{2.20}$$

If $|V_A| \gg V_B$, the above relationships can be further simplified to $I^{2\omega} \propto |V_A|$ and $I^{2\omega} \propto |V_A|^2$. In other words, EFISH has predictable linear or square dependence with the applied bias under reserve biased condition. This relationship becomes a convenient signature to recognize the Schottky junction via a easy accessible experiment of "SHG vs Bias Sweeping" [73]. It also allows us to separate the EFISH for Schottky junction from other SHG contribution by introducing the interference theory. We will revisit these results again in Chapter 4.

2.2 SSHG Experimental Description

The experimental setup is primarily designed and constructed by James Walker [74] as illustrated in Figure 2.4. The pulsed laser generated from a Ti:Sapph oscillator with 76 MHz repetition rate and pulsewidth of 100 fsec is directed to the sample surface. The SHG photons are generated along with the reflected pulsed laser. This mix of SSHG and initial laser light is then separated by a prism/monochromator and the SSHG is detected by a photon counting system. The SHG light is analyzed by the polarimeter system consisting of quarter-wave plate (QWP) and polarizer to determine its polarization state, which includes the intensity of p- and s-polarized state as well as the relative phase between these two polarization state. The analysis method will detailed later.

The laser beam existing Ti:sapphire laser is linearly polarized in the p-direction at the percent level. A long-pass glass filter was used on the input beam to block the green light from pumping laser and second harmonic light generated in the Ti:Sapphire oscillator itself as well as at the turning mirrors shown in the figure. A fixed polarizer in p direction further eliminates the s state light in the input laser. The polarization of the p state input laser is then rotated by a rotating achromatic half-wave plate (HWP) to set the linear polarization direction from 0 to 360 degrees. Afterwards, the laser is focused on to the sample surface by lens on a translation stage, and the reflected beam is then collimated by another lens. After initial separation of the linear and second harmonic light by a UV-grade fused silica prism, the SHG photons are sent through a polarimeter. Before being collected by the photomultiplier tube, the SHG photons are further filtered by the 1/4 meter monochromator for eliminating the input laser light and dark laboratory unpolarized background light.

The polarimeter, consisting of a quarter wave plate (QWP), a p direction polarizer and intensity measurement, is the essential part for SHG photon analysis. The detailed configuration is shown in the dash line section of Figure 2.4. One full cycle rotation of the QWP can yield an "SHG Intensity vs Rotation Angle" trace from which the polarization state of the SHG light can be extracted. The full cycle rotation QWP is divided by 50 steps driven by a step motor, and

the SHG photons are counted for a 20ms time window at each QWP rotation angle. Each QWP revolution produce 50 data points of SHG counting for 50 consecutive QWP rotation angle. In order to increase the signal-to-noise ratio and build up statistically based error bars, many revolutions of the QWP were averaged together until the desired the signal quality is achieved. Thus, the measurement results in 50 data points and the associated statistical error. This data is then fitted in order to determine the polarization of the second harmonic light.

2.2.1 Stokes optics and polarimetry curve

Next, I show the equations based on Stokes parameters for extracting the polarization state of the SHG light from the "SHG Intensity vs QWP Angle" trace. Stokes parameters defined by George Gabriel Stokes in 1852 [75] describe the intensity and polarization of the light on the Poincare sphere. The Stokes parameters, S_0, S_1, S_2 and S_3 completely describe the intensity and polarization state of the light through the below relationships:

$$S_0 = I_P + I_S \tag{2.21a}$$

$$S_1 = I_P - I_S \tag{2.21b}$$

$$S_2 = I_{+45} - I_{-45} \tag{2.21c}$$

$$S_3 = I_{RHC} - I_{LHC} \tag{2.21d}$$

The I_p and I_s are the intensity of the p state and s state light; $I_{\pm 45}$ are the intensities of the light decomposed along ± 45 degree basis vectors; I_{RHC} and I_{LHC} are the light intensities decomposed using right-hand and left-hand circular basis vectors. S_0 is the Stokes parameter identifying the total intensity of the light with $S_0^2 = S_1^2 + S_2^2 + S_3^2 + I_{unpol}$. I_{unpol} is the unpolarized background light which is either small or indistinguishable from the zero.

We assume the input and out light are represented by Stokes Vector, $\vec{S}_{in}$ and $\vec{S}_{out}$. When the SHG light with polarization state of $\vec{S}_{in}$ passes through the QWP and polarizer, the polarization of output light is manipulated to be $\vec{S}_{out}$. This polarization manipulation process can be described

Figure 2.4: The general SSHG experimental setup. Ultrafast pulses of approximately 100 fsec in width from the Ti:Sapph laser oscillator are steered through polarization control optics and directed onto the sample in a UHV optical access cryostat. The surface generated second harmonic light is recolumnated and filtered from the reflected incident light using a UV-grade fused silica prism. The SSHG light is then passed through a rotating wave plate polarimeter which analyzes the 2ω polarization state. Further filtering of the incident light and stray background light is accomplished with a grating monochromator followed by a photo multiplier tube and associated photon counting electronics.

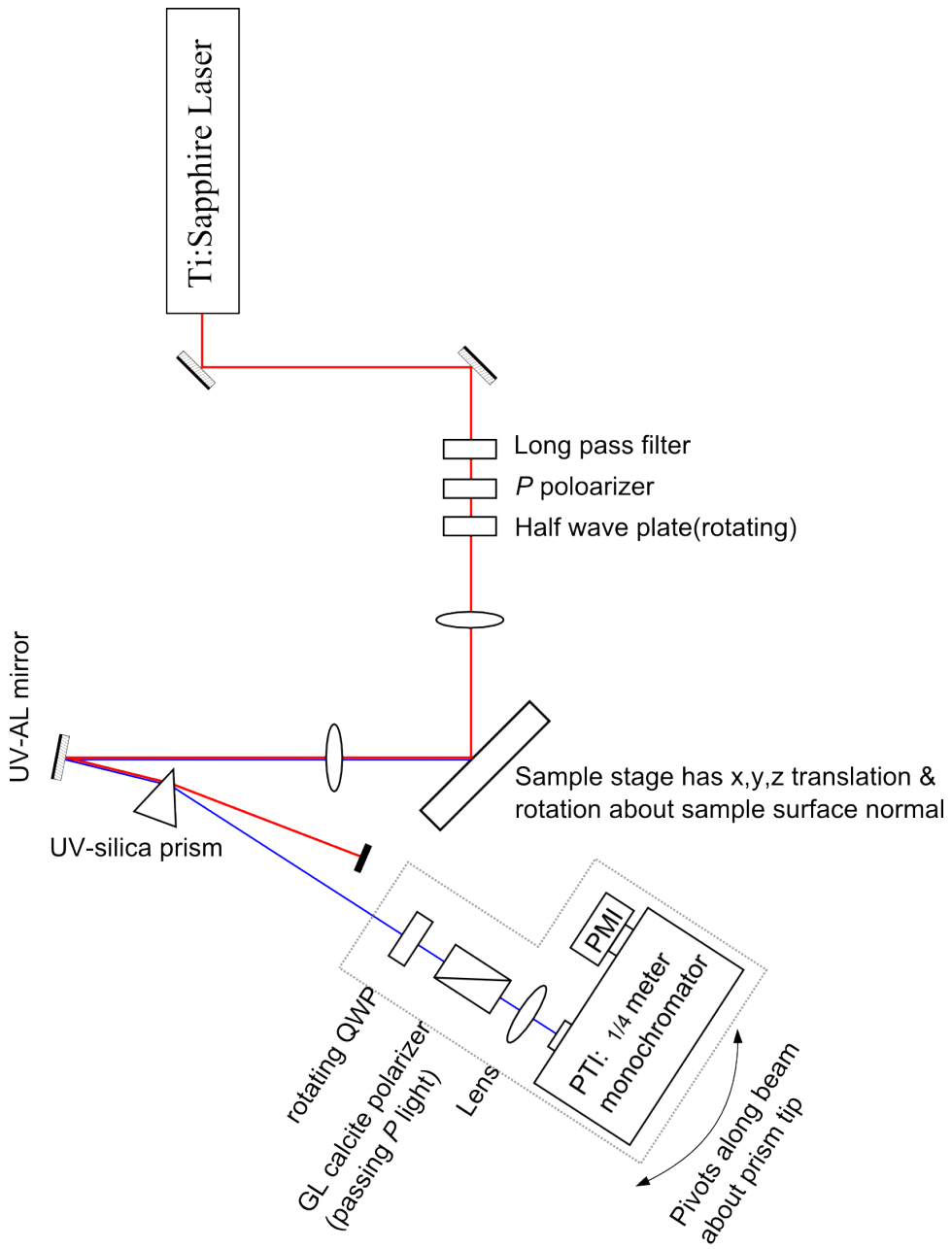

by Mueller matrices:

$$\vec{S}_{out} = \mathbf{M}\vec{S}_{in} \tag{2.22}$$

If a beam of light passes through optical element M1 followed by M2 then it is written

$$\vec{S}_{out} = \mathbf{M}_2(\mathbf{M}_1\vec{S}_{in}) \tag{2.23}$$

The Mueller matrix for a waveplate of retardance φ, with the fast axis parallel oriented to the p-polarized direction is:

$$\mathbf{M}_{\mathrm{WP}} = \begin{pmatrix} 1 & 0 & 0 & 0 \\ 0 & 1 & 0 & 0 \\ 0 & 0 & \cos\varphi & \sin\varphi \\ 0 & 0 & -\sin\varphi & \cos\varphi \end{pmatrix} \tag{2.24}$$

The Mueller matrix for a linear polarizer oriented to pass p-polarization is:

$$\mathbf{M}_{\mathrm{LP}} = \begin{pmatrix} \frac{1}{2} & \frac{1}{2} & 0 & 0 \\ \frac{1}{2} & \frac{1}{2} & 0 & 0 \\ 0 & 0 & 0 & 0 \\ 0 & 0 & 0 & 0 \end{pmatrix} \tag{2.25}$$

The Mueller matrices of optical component oriented at any angle(clock-wise) can be generated from the original matrix and the rotation operator R_ϕ and $R_{-\phi}$, by

$$\mathbf{M}(\phi) = \mathbf{R}(-\phi)\mathbf{M}\mathbf{R}(\phi)$$

where:

$$\mathbf{R}(\phi) = \begin{pmatrix} 1 & 0 & 0 & 0 \\ 0 & \cos\phi & -\sin\phi & 0 \\ 0 & \sin\phi & \cos\phi & 0 \\ 0 & 0 & 0 & 1 \end{pmatrix} \tag{2.26}$$

Therefore, the output SHG light $\vec{S}_{out}$ after passing through the QWP($\varphi = \frac{\pi}{2}$) and p oriented linear polarizer is formulated as:

$$\vec{S}_{out} = \mathbf{M}_{\mathrm{LP}}(\theta)\mathbf{M}_{\mathrm{QWP}}(\phi, \varphi = \frac{\pi}{2})\vec{S}_{in} = \mathbf{M}_{\mathrm{LP}}(\theta)\mathbf{R}(-\phi)\mathbf{M}_{\mathrm{QWP}}(\varphi = \frac{\pi}{2})\mathbf{R}(\phi)\vec{S}_{in} \tag{2.27}$$

When taking the SHG intensity trace, the QWP is rotated with a stepper-motor and controller so that one rotation corresponded to 50 intensity measurements. Therefore, for each intensity measurement with a full rotation of the wave plate, the rotational operator is written as $R(\phi = 2\pi t)$, where t varies from 0 to 1 in 50 steps. If we assume the QWP has accurate phase retardance ($\varphi = \pi/2$), linear polarizer is perfectly aligned ($\theta = 0$), and no offset in the quarter waveplate ($\phi = 2\pi t$), and the light intensity can be picked out from the Stokes vector by the vector (1,0,0,0), thus the fitting function for SHG intensity trace will be:

$$\begin{aligned} S_{0-out} &= (1,0,0,0)\mathbf{M}_{\mathrm{LP}}(0)\mathbf{R}(-2\pi t)\mathbf{M}_{\mathrm{QWP}}\mathbf{R}(2\pi t)\begin{pmatrix} S_0 \\ S_1 \\ S_2 \\ S_3 \end{pmatrix} \\ &= \frac{1}{2}(S_0 + S_1\cos^2 4\pi t - S_2\cos 4\pi t\sin 4\pi t + S_3\sin 4\pi t) \end{aligned} \tag{2.28}$$

In practice, that small errors in the actual QWP retardance φ, the alignment of the fast axis of the compensator and transimission axis of the polarizer to the laboratory frame are necessary to consider for accurate fits of the input SHG Stokes parameters. Therefore, I follow the work by Chaz

Teplin [59], the previous student in the lab, to calibrate these errors before the SHG measurement. Following the detailed procedure in Teplin's thesis, we are able to determine the initial offset of the QWP's fast axis orientation ϕ_0, the QWP's actual phase retardance for SHG light φ_0 and the linear polarizer's deviation θ_0 from p polarization direction. The general procedure for this calibration method is generating the pure p state SHG from the sample surface by p-polarized input laser. This p state SHG is converted into circularly polarized light using a variable waveplate set to be a quarter wave at 410 nm and tilted so that its fast axis made a 45° angle to the p-polarization direction. By fitting into the polrimetry curves from p-polarized and circularly polarized SHG light, we are able to determine the calibration parameters.

Once obtained the calibration parameters, we can proceed to fit the polarimetry data, i.e. the SHG intensity as a function of polarimeter QWP angle of a full rotation. In Figure 2.5, we show two examples of the polarmetry data at different input polarization from ITO/Glass sample. This sample is fabricated by depositing 70 nm Indium Tin Oxide (ITO) film on fused silica, and the device is transparent for the input laser and SHG light. The resulting SHG photons comes from the air/ITO and ITO/Glass interfaces. By fitting those polarimetry curves to Equation (2.28), the polarization information is extracted with fitted Stokes parameters listed in Figure 2.5. The light intensity at p, s state and their relative phase can be derived from the fitted Stokes parameters according to Equation (2.29). For the top panel of p input laser, the resulting $I_P = 54.69 \pm 0.10$ $I_S = 1.03 \pm 0.06$ and $\delta = -3.091 \pm 0.003$ indicate that 70 nm ITO film is a bright resource of p state SHG under p polarized input laser. For the bottom panel of mixed polarized input (65°) laser, the resulted SHG polarization is of $I_P = 0.427 \pm 0.012$, $I_S = 7.394 \pm 0.026$ and $\delta = -0.2685 \pm 0.0040$, which is much darker than the SHG intensity under p state input laser. In Chapter 3 and 4, the SHG intensity is measured in the unit of photon count/ms. In Chapter 5, the SHG intensity is measured with voltage pulse temporal integral. Therefore, the SHG intensity is defined in dimensionless unit through the thesis.

$$I_P = \frac{1}{2}(S_0 + S_1) \tag{2.29a}$$

$$I_S = \frac{1}{2}(S_0 - S_1) \tag{2.29b}$$

$$\delta = arctan(\frac{S_3}{S_2}) \tag{2.29c}$$

For any particularly interested samples, we can obtain the SHG polarimetry data at different polarization angle of the input laser, and this kind of measurement is named as "Input Polarization Scan". For this measurement, the HWP is rotated for a full cycle to the rotate the input laser polarization angle for 720°. Starting from p state, the input laser polarization sweeps through p-s-p quadrant for four times. This would help us to understand the isotropy of the sample interfaces. The HWP is rotated with a stepper-motor and controller so that one rotation corresponded to 100 polarimetry measurements.

2.2.2 HWP calibration

Before each Input Polarization Scan, we need to recalibrate the orientation of HWP fast axis to the p polarized plane relative the sample alignment. This is because the sample surface normal may be slightly changed after the mounting procedure; as a result, the p polarized plane waggles according the sample orientation. It is necessary for the Input Polarization Scan to start from p polarized state for each measurement. In order to calibrate the accurate p polarization angle of the input laser, we utilize the different reflectivity for s and p polarized light to locate the HWP position. According to the Fresnel equation, the reflectivity R_p and R_s for p and s polarized light are usually unequal. Because HWP only change the direction of the polarized field of the incoming linear polarized light, then the total reflection coefficient for the linear polarized light can be written as:

$$R = R_p \sin^2\phi + R_s \cos^2\phi \tag{2.30}$$

Figure 2.5: Measured SHG intensity as a function of polarimeter quarter waveplate angle for different input polarizations from ITO/Glass sample. Solid lines show the fit to the polarization state of the second harmonic beam. In the top panel, the incident beam is p-polarized and the fitting results is $S_1 = 53.66 \pm 0.08, S_2 = -15.01 \pm 0.11, S_3 = -0.76 \pm 0.05$ and $\chi^2 = 4.9$, meaning the resulting SHG is nearly p-state. In the lower panel, the incident beam is partly mixed polarized($65°$) and the fitting result is $S_1 = -6.967 \pm 0.025, S_2 = 3.428 \pm 0.028, S_3 = -0.942 \pm 0.012$ and $\chi^2 = 8.4$.

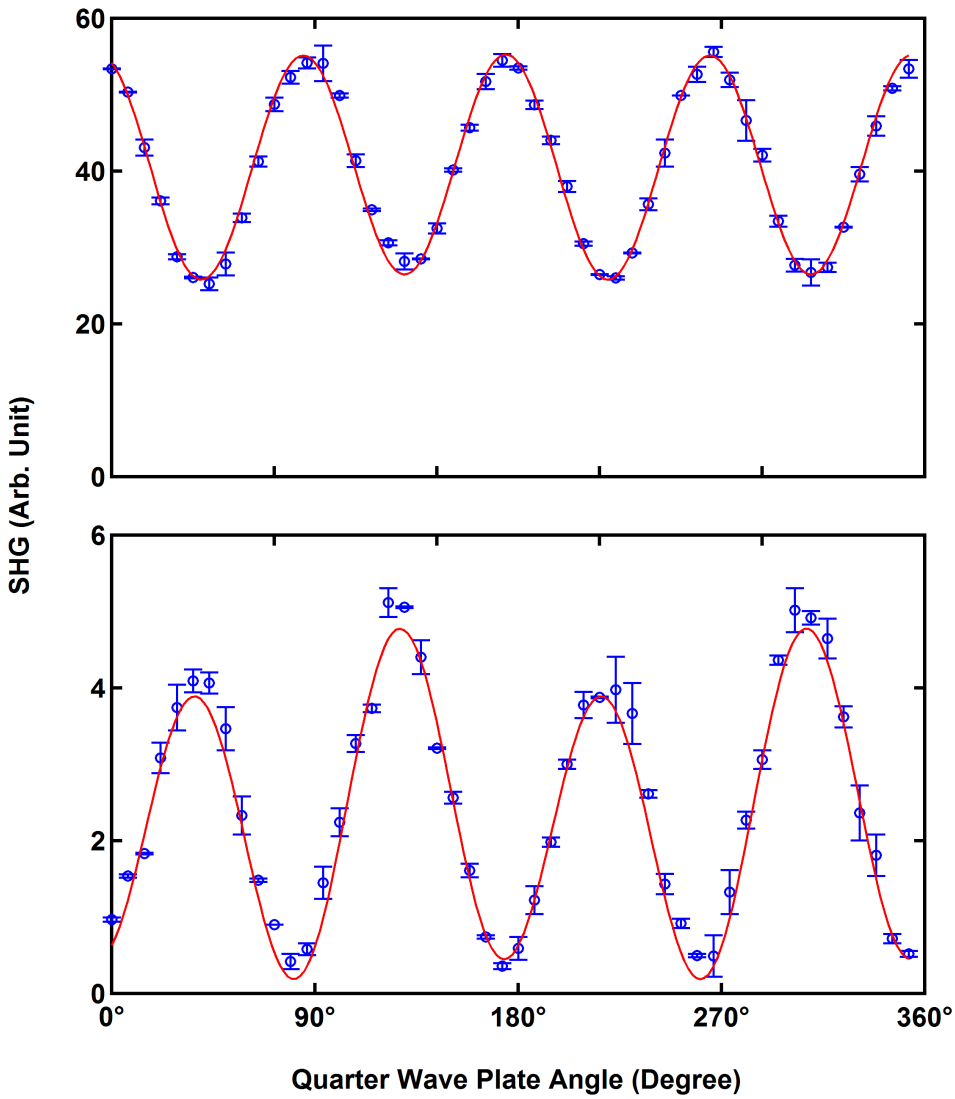

ϕ is the polarization angle of input linear polarized light respective to the p state. For our samples, we always have $R_p < R_s$; therefore, the accurate p polarized light can be found by minimizing the total reflection coefficient when rotating the HWP. The silicon photo diode is used to measure the intensity of the reflected laser. The beam chopper and the lock-in amplifier are used to eliminate the background light noise(see Figure 2.6). The beam chopper is arranged in the beam path to modulate the reflected laser at 500Hz. The signal from silicon photo diode is fed to the Channel A of the lock-in amplifier, while the reference frequency signal is fed to the Channel B of the lock-in amplifier. The processed reflected laser intensity is measured by the National Instrument DAQ card, while the Labview code on the desktop controls the rotation of the HWP. The produced the intensity of reflected laser frequency vs HWP rotation step allows one to find the intensity minimum, i.e. the accurate p polarized input laser.

After all the procedure described above, we are ready to proceed to input polarization scan. I have used the old Aluminum sample fabricated by Chaz Teplin to reproduce the Input Polarization Scan described in his work [59, 76, 77]. Figure 2.7 indicates the the s-intensity, p-intensity, and relative phase of the p and p polarized electric fields is shown as a function of input polarization. In this figure, the maximum intensity of p state SHG is observed at p state input polarization, and this geometry is dominated by the contribution from $\chi^{(2)}_{\perp}$. The minimum intensity of p state SHG is observed near s state input polarization. The maximum intensity of s state SHG is observed at mixed polarized ($\phi = 45°$) input polarization, which is corresponding to the tensor of $\chi^{(2)}_{yzy}$. In summary, this input polarization scan has repeated the work in the Chaz's thesis. The symmetric behavior in the four quadrants of input polarization angle proves the uniformity of the optics system.

2.2.3 Eta Kappa fitting

I use the model developed by Teplin to analyse the second harmonic intensity data as a function of the input laser polarization angle. In this model, we fit the ratio of the s-to-p intensities to avoid concerns that the incident beam was not equally intense at all input polarizations arising

Figure 2.6: The setup for calibration of the p-polarized input laser.

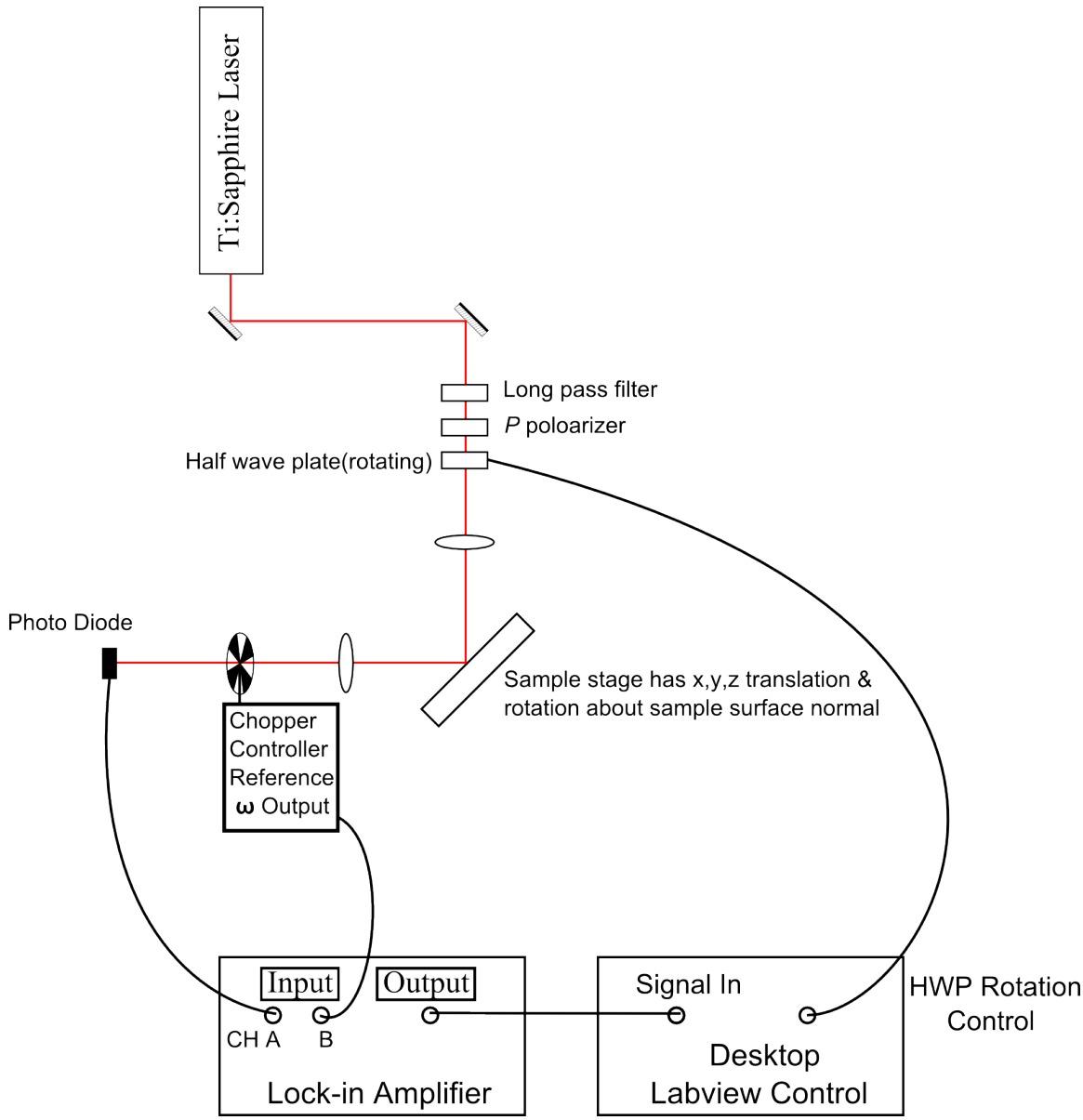

Figure 2.7: The input polarization scan from the Aluminum film fabricated by *Chaz Teplin*. The horizontal axis represents the full-cycle rotation of HWP, and it corresponds to 720° rotation of the input laser polarization. The symmetric behavior in the four quadrants of input polarization angle proves the uniformity of HWP and other optics components.

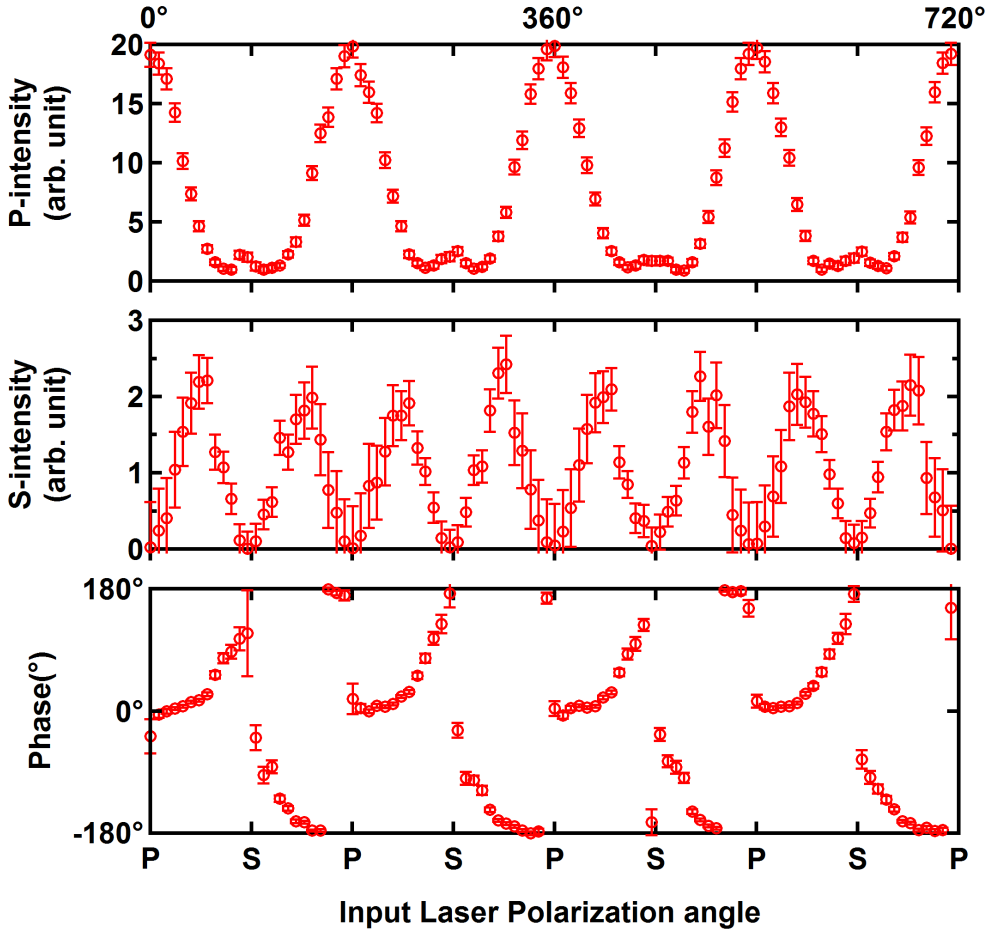

from imperfections in the input polarization optics. By introducing the complex fitting parameters η and κ, the fitting functions can be written as

$$\tan \Psi^{(2)} = \frac{|E_S^{(2)}|^2}{|E_P^{(2)}|^2} = \frac{\sin^2\phi\cos^2\phi}{(\eta\cos^2\phi + \kappa\sin^2\phi)^2} \tag{2.31}$$

and

$$\delta = \mathrm{Arg}(\eta\cos^2\phi + \kappa\sin^2\phi) - \mathrm{Arg}(\sin\phi\cos\phi) \tag{2.32}$$

where η and κ is expressed by the tensor elements and the linear optical constants

$$\eta = \frac{k_{1z}+k_{2z}}{\epsilon_2 k_{1z}+\epsilon_1 k_{2z}}\frac{\epsilon_1}{k_1}\frac{t_p}{t_s}\frac{1}{2\sin\theta_T\chi_{\parallel}^{(2)}} \times [2k_{2z}\cos\theta_T\sin\theta_T\chi_{\parallel}^{(2)} + k_x(\sin^2\theta_T(\chi_{\perp}^{(2)}+\chi_{bulk}^{(2)}) + \cos^2\theta_T\chi_{bulk}^{(2)})] \tag{2.33}$$

$$\kappa = \frac{k_{1z}+k_{2z}}{\epsilon_2 k_{1z}+\epsilon_1 k_{2z}}\frac{\epsilon_1}{k_1}\frac{t_S}{t_P}\frac{k_x\chi_{bulk}^{(2)}}{2\sin\theta_T\chi_{\parallel}^{(2)}} \tag{2.34}$$

In this model, η can be viewed as the ratio of p-polarized second harmonic from p-polarized input light to s-polarized second harmonic from *mixed* polarization input light. κ can be viewed as the ratio of p-polarized second harmonic from s-polarized input light to s-polarized second harmonic from mixed polarization input light. Figure 2.7 shows the ratio of SHG s-to-p intensity ratio and relative phase as a function of the input laser polarization angle. The data is fitted into the Equations (2.31) and (2.32). The fitting results are $|\eta| = 1.674 \pm 0.036, \phi_\eta = 0.46^\circ \pm 0.43^\circ, |\kappa| = 0.479 \pm 0.013, \phi_\kappa = 116.1^\circ \pm 1.7^\circ$ with $\chi^2 = 1.3$. These results are slightly differed from the values reported by Chaz Teplin, and it could because of the surface oxidization after air exposure after many years.

Figure 2.8: Second harmonic light from Aluminum film fitted to Equations (2.31) and (2.32). The fitting results are $|\eta| = 1.674 \pm 0.036, \phi_\eta = 0.46^\circ \pm 0.43^\circ, |\kappa| = 0.479 \pm 0.013, \phi_\kappa = 116.1^\circ \pm 1.7^\circ$ with $\chi^2 = 1.3$. These results are slightly differed from the value reported by Chaz Teplin [59], and it could because of the surface oxidization after air exposure after many years.

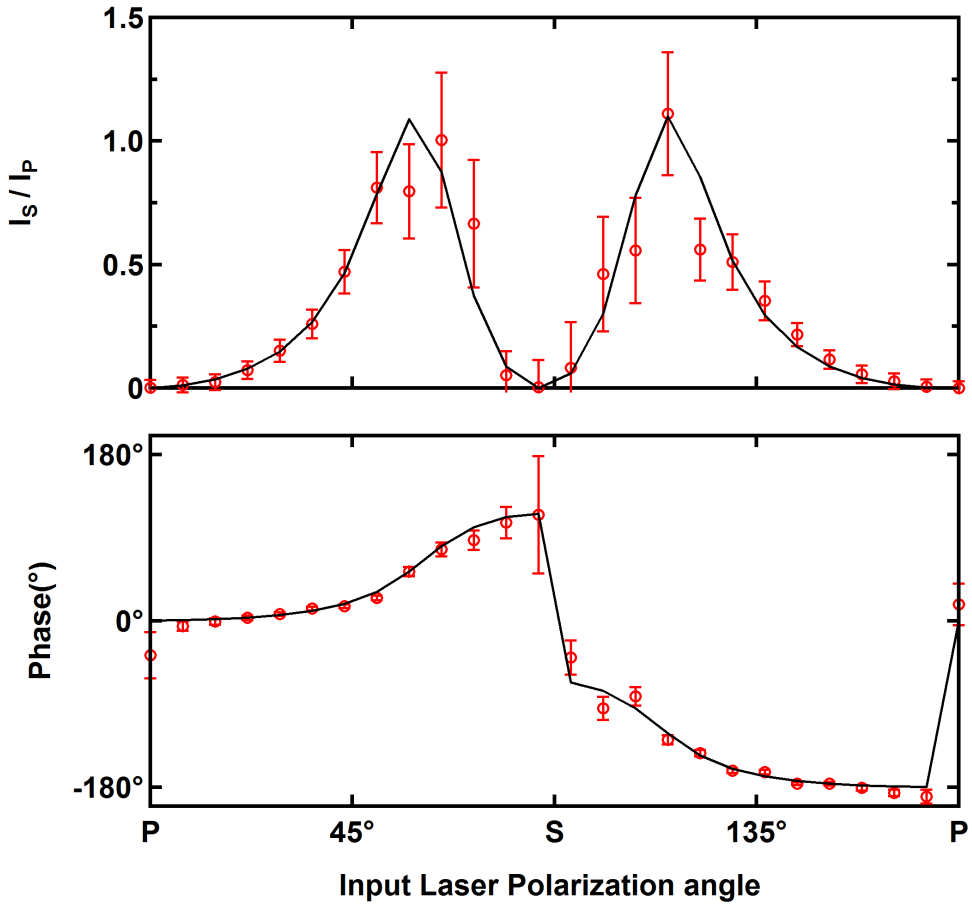

2.2.4 Summary

In this Chapter, I have prepared the mathematical background for SSHG and EFISH which is necessary for analysing and interpreting the SHG data in the following Chapters. The experimental set up is described, and typical data taking methodology is explained. Finally, the input polarization scan SHG data from Aluminum film is obtained and the fitting algorithm is presented and exercised. The SHG results are compared with previous work to validate the experimental set up.

Typically, in the Chapters below, I will report the basic SHG output quantities of I_p, I_s and the phase shift between them, versus changes in experimental conditions including applied device bias voltage and sample rotations about the surface normal. These plots allow us to see how the underlying SHG tensor elements of $\chi^{(2)}$ change with experimental conditions, and thereby allow us to use the measured SHG to explore changes in the optically accessible interfaces.

Chapter 3

SHG from Heterojunction solar cells

In our first effort to see whether SHG and EFISH measurements can be useful for studying interfaces in photovoltaic systems, we studied $\sim$ 15% efficient SiHJ devices based on both p and n-type wafers. The devices were grown and patterned by the NREL silicon group. These solar cell devices were prepared as part of a project to understand the Sanyo HIT devices. The growth and fabrication are describe in Ref [78, 79]. Briefly, the intrinsic and doped a-Si:H was grown with Hot-Wire Chemical Vapor Deposition (HWCVD). Transparent conducting layers and metal grids provided the front contact. A backside heterojunction and aluminum layer formed the back contact [80]. Figures 3.1 and 3.2 show the layer structure and picture for n-type and p-type SiHJ solar cell. The standard JV measurement is performed by attaching the electrode contacts to the front gold grid and back side metal layer.

3.1 Bias Dependent SHG on Silicon Heterojunction device

For the SHG measurements, Ti:Sapphire laser light tuned to 820 nm (1.51 eV) was focused on the sample. The 1.51 eV laser is strongly absorptive in crystalline silicon(c-Si) wafer. The laser excites electron and hole pairs which are separated by build-in electric field at the heterojunction of c-Si/a-Si:H. As a result, the electric voltage potential is built between the opposite side of the device yielding photocurrent in the closed circuit. The current-voltage measurements of the solar cell are obtained under this laser illumination and dark condition as shown in Figure 3.3. It is indicated that the Open Circuit voltage of the solar cell is -0.65V. At the each bias, we perform

the SHG measurement with the fixed input laser polarization angles at p, s and *mixed* polarization state.

Because 10 nm a-Si:H layer is super thin and ITO is almost non-absorptive for 1.51 and 3.02 eV photons, the 1.51 eV laser penetrates through the top ITO and a-Si:H layer, and is finally absorbed by c-Si wafer. The SHG 3.02 eV photons are allowed to escape from c-Si/a-Si:H area. Around this area, multiple interfaces are capable of producing SHG photons, including air/ITO, ITO/a-Si:H and a-Si:H/c-Si interfaces. In addition, the strong electric field present in the heterojunction can also contribute to SHG signal. Though c-Si is strongly absorptive at both wavelength, the SHG contribution form the top bulk c-Si and c-Si/a-Si:H border can still contribute. The total SHG signal sensed by Photon Multiplier Tube (PMT) is the interference combination of the SHG contributions from multiple interfaces and strong electric field in the a-Si:H and c-Si bulk as illustrated in Figure 3.1.

Below, we delineate various polarization geometries using an $inOUT$ notation wherethe first, lowercase letter or letters denotes the laser polarization as either p-polarized (p), s-polarized (s) or linearly-polarized with equal p and s intensities (mix) and the second, capitalized letter denotes the SHG polarization as either P or S polarization. To facilitate measurements at different sample rotation angles and device bias conditions, the devices were mounted on a rotation stage in the SHG measurement apparatus and contacted in-situ to standard current-voltage measurement equipment.

In Figure 3.3, "SHG vs Bias" is shown at four different geometries: *pP, sP, mixP* and *mixS*. In all geometries, we observe a change in the SHG signal with sample bias. A number of factors could contribute to the bias sensitivity in the SHG signal observed in Figure 3.3. These include: changes in charge distribution at the various material interfaces, changes in the electric field throughout the optically accessible regions of the device and changes in the bulk c-Si contributions. Changes in the charge distributions and associated electric fields within the device are important for device characterization. Different choices of input polarization, sample orientation, incident energy, etc. can help to separate these different device regions.

Due to the uniform layer structure of the SiHJ solar cell, the internal electric field in the device

Figure 3.1: Layer structure of the SiHJ solar cell used for the experiments. The red arrow indicates 820 nm laser pass through the sample; the blue arrows illustrate various SHG contribution from multiple interface and bulk part.

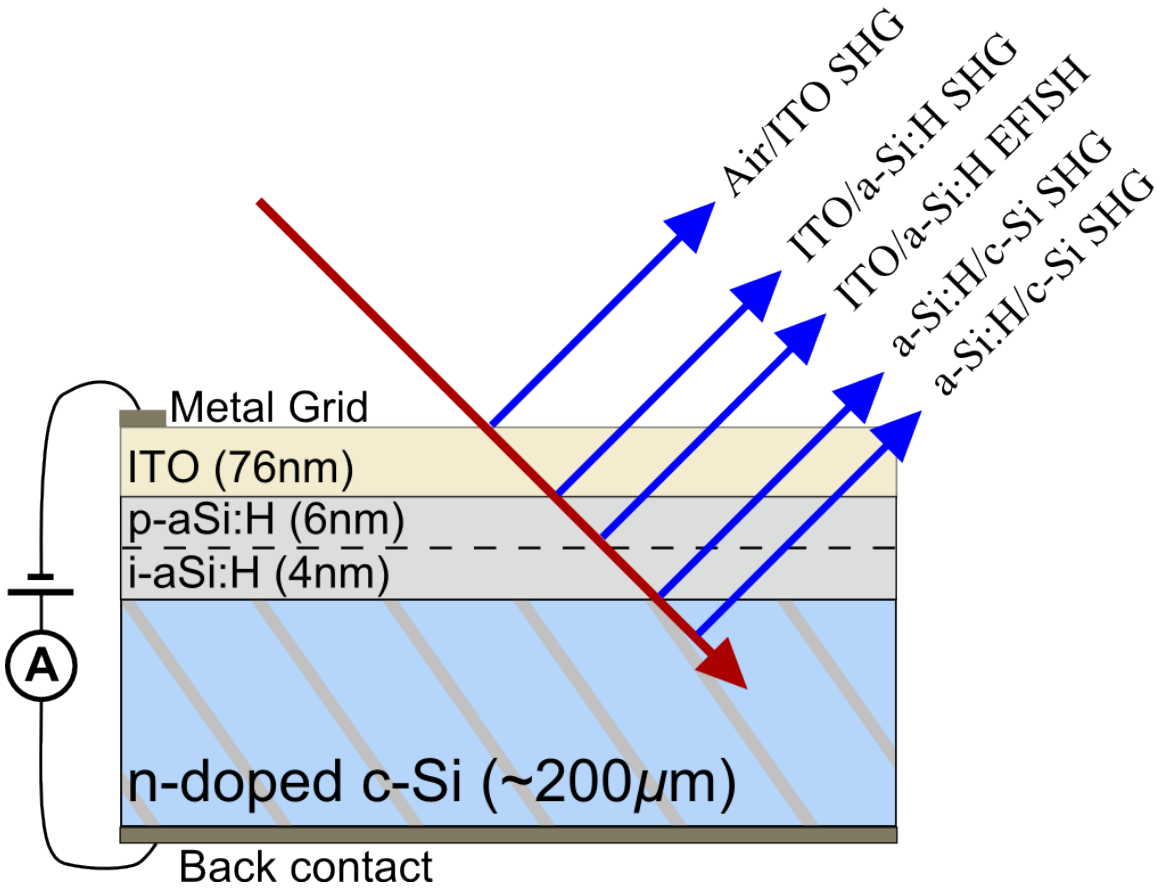

Figure 3.2: The picture of the SiHJ solar cell used for the experiments. The whole device is fabricated on n-type wafer silicon. The silver area is super thin amorphous silicon layer. The 1cm X 1cm blue square is the SiHJ solar cell device with the structure indicated in Figure 3.1

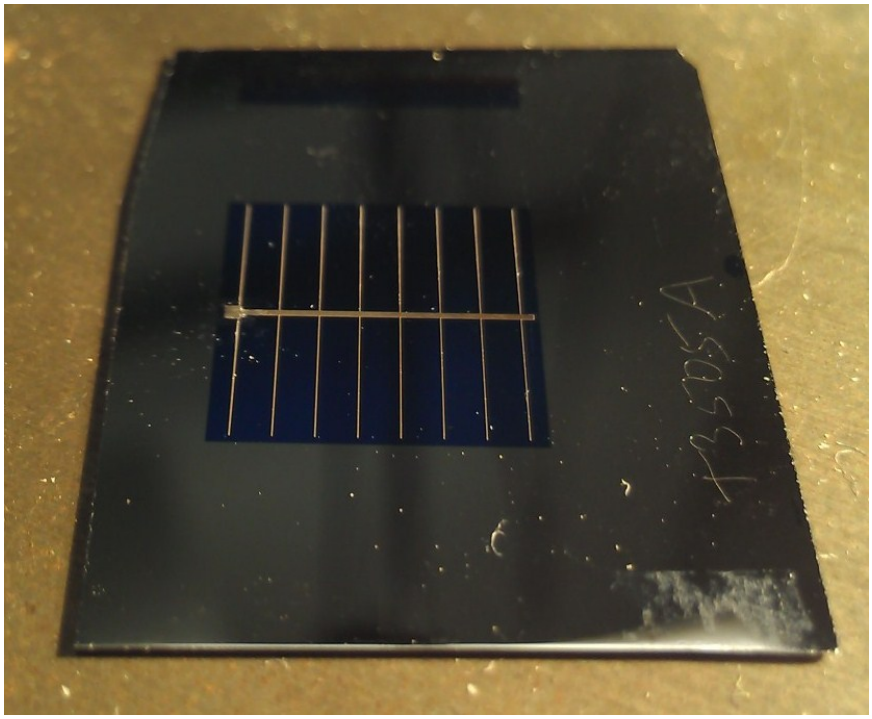

Figure 3.3: The JV curve of the corresponding SiHJ solar cell in dark condition(Blue square) and 1 Watt laser(Red circle). The JV curve under illumination indicates the Open Circuit voltage is 0.65V and Short Circuit current is 38mA. The SHG signals in all geometries display changes at different bias condition.

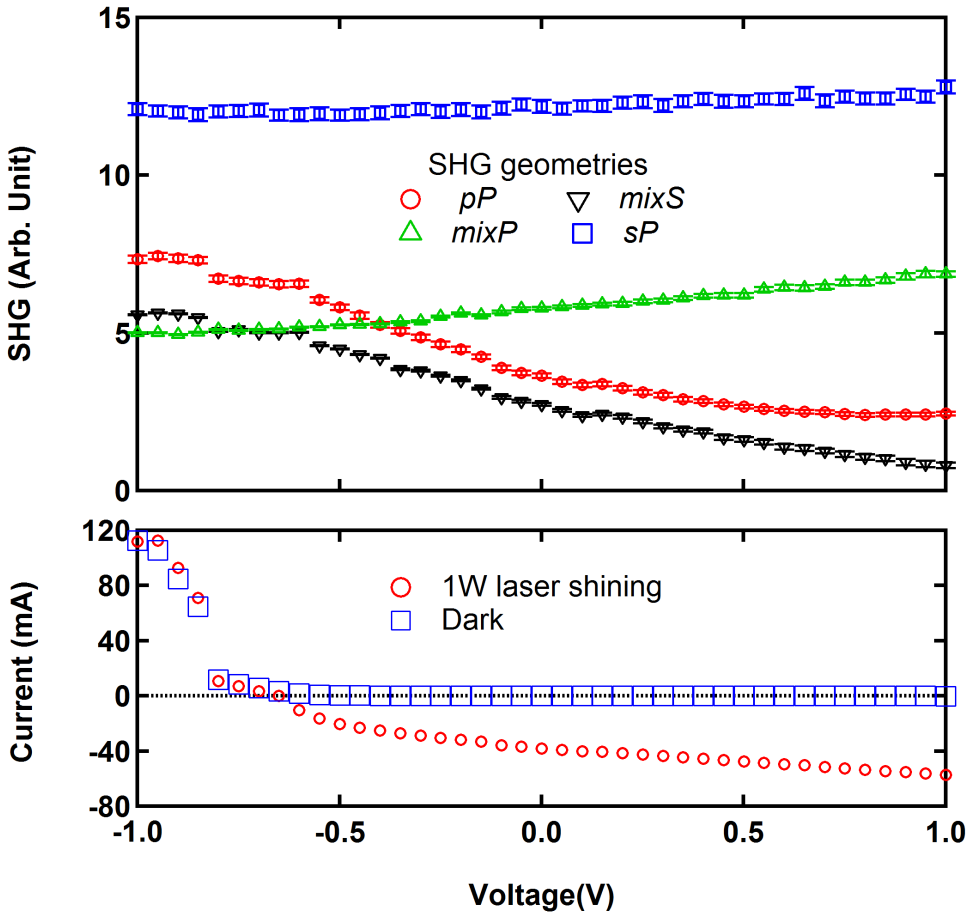

are along the surface normal. The resulting EFISH should produce isotropic SHG photons. Ana Kanevce in NREL simulated the electric field profile in the SiHJ solar cell based on the fabrication doping information and semiconductor theory [81]. The simulated electric field profile in the layer structures under illumination at various bias conditions is presented in Figure 3.4. The internal electric fields reach up to $10^6 V/cm$ in the a-Si:H layer due to the band bending at the junction area. As we shall see in Chapter 4, this strong electric field can produce considerable EFISH in the static SHG signal. It is noticeable that significant electric field change happens in the intrinsic amorphous layer and near interface area in c-Si bulk at different bias conditions. The electric field can change up by $\sim 30\%$ between 0V and 0.6V in this region. Therefore, the EFISH corresponding to this strong electric field change can be an important part of the bias-dependent SHG signal in Figure 3.3.

We also measured the "SHG vs bias sweep" on the reversed doping type SiHJ solar cell based on the p type c-Si wafer. With the similar structure as n type SiHJ solar cell as shown in Figure 3.1, the top p doped a-Si:H is replaced with n doped a-Si:H deposited on the p type c-Si wafer. Under laser illumination, the p type SiHJ solar cell produce the external voltage and current of opposite polarity as for the n type SiHJ device (see the JV curves in Figure 3.5). At the same time, the SHG signal also reversed the polarity under the bias sweep in Figure 3.5. This phenomenon corresponds to the electric fields of the opposite directions present in the "twin" reverse doped SiHJ solar cells.

3.2 SSHG vs Input Polarization Angle

An input polarization scan is to obtain the SHG signal at different input laser polarization angles. It involves of rotation of the linear input polarization step-wise and acquisition of a polarimetry trace at each point. In this measurement, the s- and p-polarized intensities, their ratio, and relative phase δ as a function of the input polarization angle are plotted. This type of scan is useful for characterization of isotropic or anisotropic surfaces by extraction of the surface susceptibility tensor $\chi^{(2)}$. Therefore, we use this technique to characterize the bias-dependent SHG signal from SiHJ solar cell.

Figure 3.4: The device simulation for electric field profile in the SiHJ junction under one sun illumination at different bias conditions. It is noticeable that significant electric field change happens in the intrinsic amorphous layer and near interface area in c-Si bulk at different bias conditions [81].

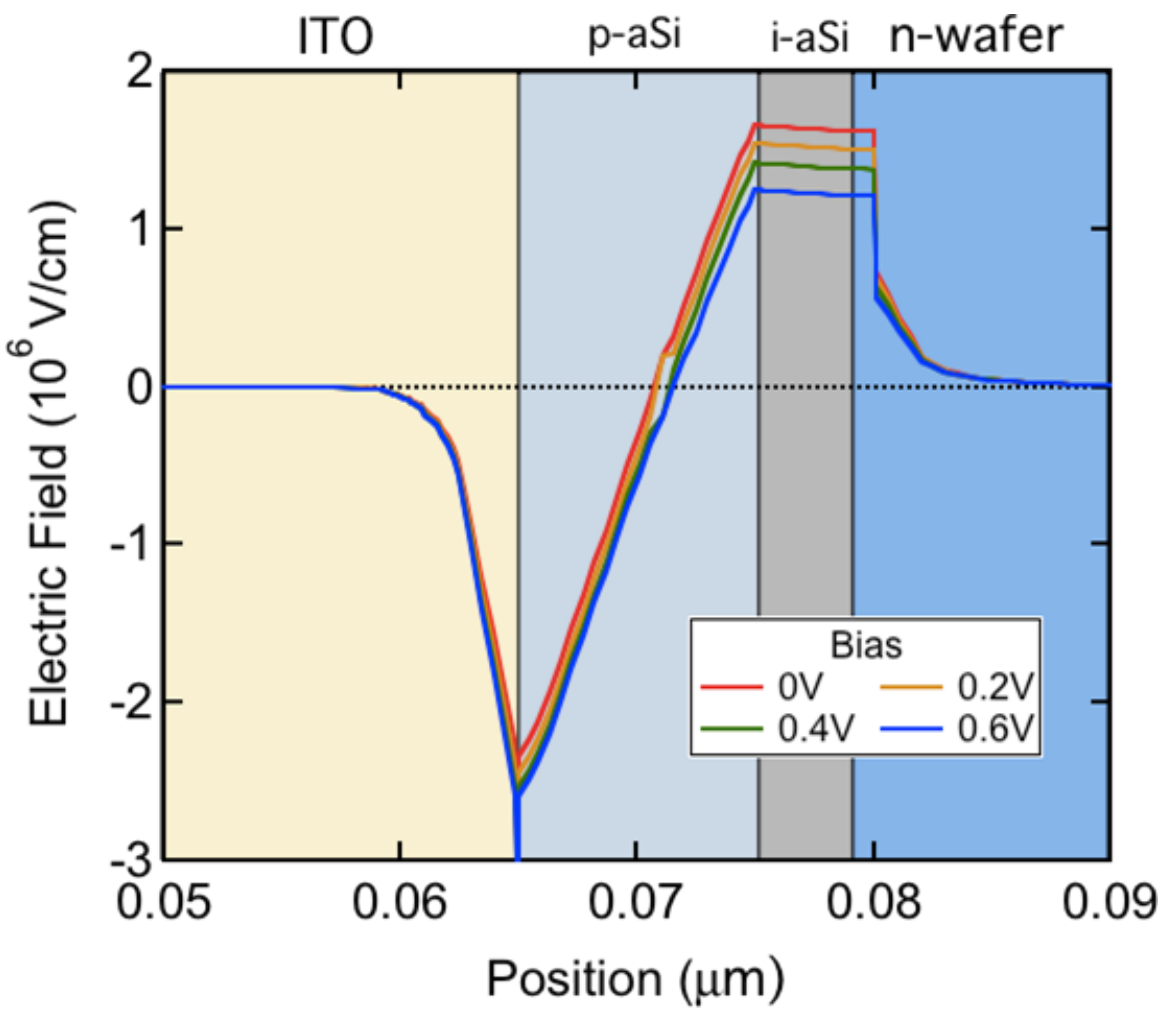

Figure 3.5: Lower Panel: The JV curves of the "twin" p and n type SiHJ solar cell under 1 Watt laser. The two devices have opposite Open Circuit voltages: -0.65 V for n type device and 0.65 V for p type device. Upper Panel: the *p*-state SHG signals under *p*-state input laser display symmetric opposite changes at different bias condition for the "twin" devices.

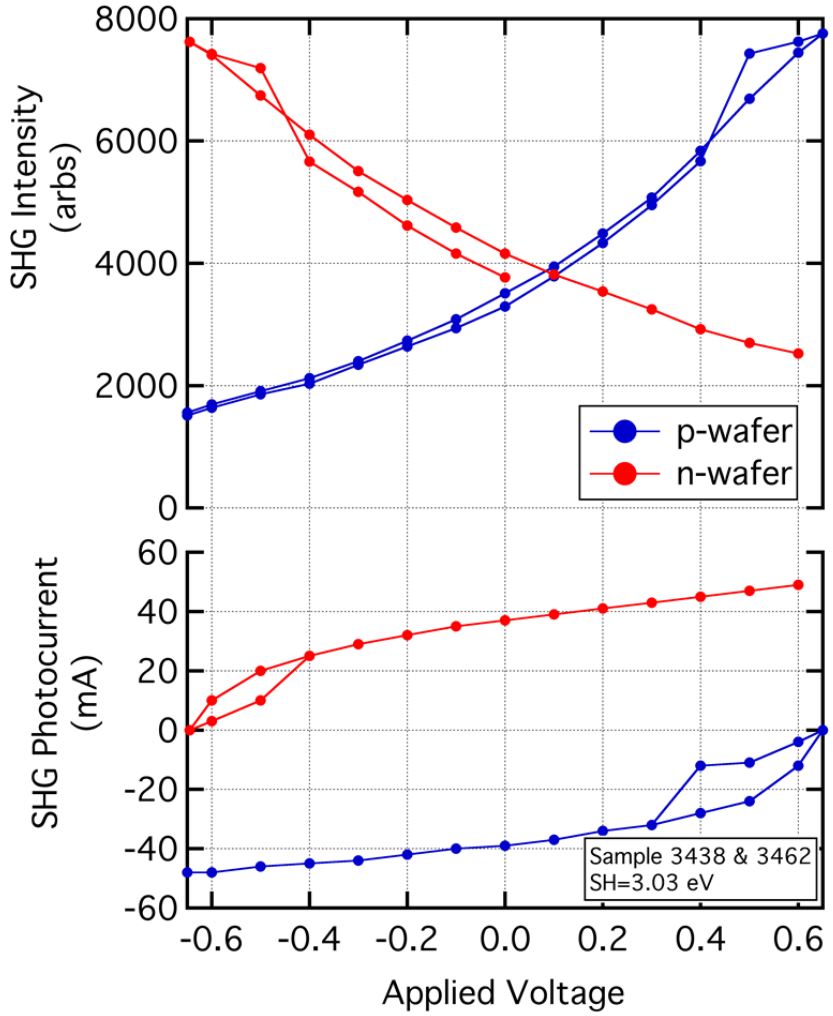

For this measurement, we choose to measure the SHG signal at two bias condition: Short Circuit (0V) and Open Circuit (-0.65V) condition on the JV curve. At each input laser polarization angle position, the SHG polarimetry curves are retrieved at SC and OC convectively to avoid any potential device change. Then we precede to the next polarization angle position for the same operation. In Figure 3.6, I present the SHG measurement from measuring the intensity and polarization state of the second harmonic light as a function of input polarization state. The maximum bias-dependent SHG change is obtained at p-input polarization (pP) and mixed input polarization at 45° ($mixP$). The pP geometry has been assumed to be dominated by the contribution from $\chi_{\perp}^{(2)}$. The $mixP$ geometry is governed by $\chi_{xyz}^{(2)}$, the only tensor element that produces s-polarized second harmonic. This phase shift occurs because the s-polarized electric field goes through zero and changes sign near p-input polarization.

We also obtained the input polarization scan from 70 nm ITO/Silica wafer to evaluate the background SHG signal from the ITO layer. Because the amorphous silica is a weak SHG source [74], the SHG signal from this sample is dominated by the front surface and back interface of 70nm ITO layer. Figure 3.7 shows the input polarization scan from the 70 nm ITO layer. The 70 nm ITO is a bright source for pP SHG geometry, while it is very dark for sP geometry. Comparing the data from 70 nm ITO layer with the input polarization scan from SiHJ solar cell in Figure 3.6 shows that the strong sP SHG photons are coming from the interfaces below ITO. In other words, the EFISH in a-Si:H and bulk Si, a-Si:H/c-Si interface and c-Si bulk are all the candidates for the sP SHG photons shown in Figure 3.6. In Chapter 4, we will see that the EFISH in a-Si:H is a dim source of bias dependent sP SHG. After taking this part in consideration, the bias-independent sP SHG signal in Figure 3.6 is believed to be generated in the c-Si bulk and a-Si:H/c-Si interface. So, we could conclude that the SHG signal from a-Si:H/c-Si interface and c-Si bulk is insensitive to the applied bias. This argument further supports our hypothesis that the bias-dependent SHG signal mainly contributed by the EFISH in a-Si:H layer of the HIT solar cell.

The data for the s-to-p intensity ratio and δ were fitted to Equations (2.31) and (2.32) simultaneously for Short Circuit and Open Circuit condition in Figure 3.8. Though the total

Figure 3.6: Second harmonic light p-polarization intensity, s-polarization intensity, and relative phase generated as a function of input polarization angle for SiHJ solar cell at Short Circuit (red circle) and Open Circuit (blue triangle) condition. Note that there is a 180° jump in phase at S state. This occurs because the s-polarized electric field goes through zero and changes sign. It is obvious that the s-polarization at 45° and p-polarization at 0° displays bias-dependent behavior at Open Circuit and Short Circuit condition.

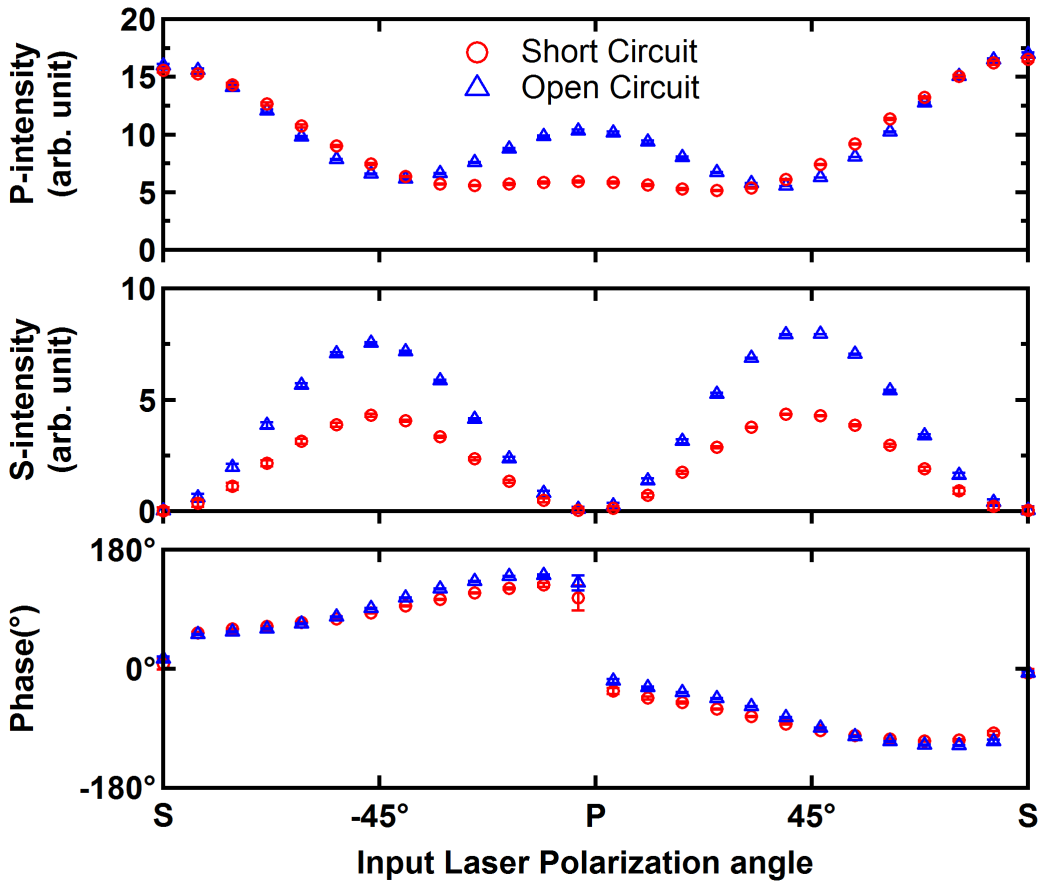

Figure 3.7: Second harmonic light p-polarization intensity, s-polarization intensity, and relative phase generated as a function of input polarization angle for 70 nm ITO film on silica wafer.

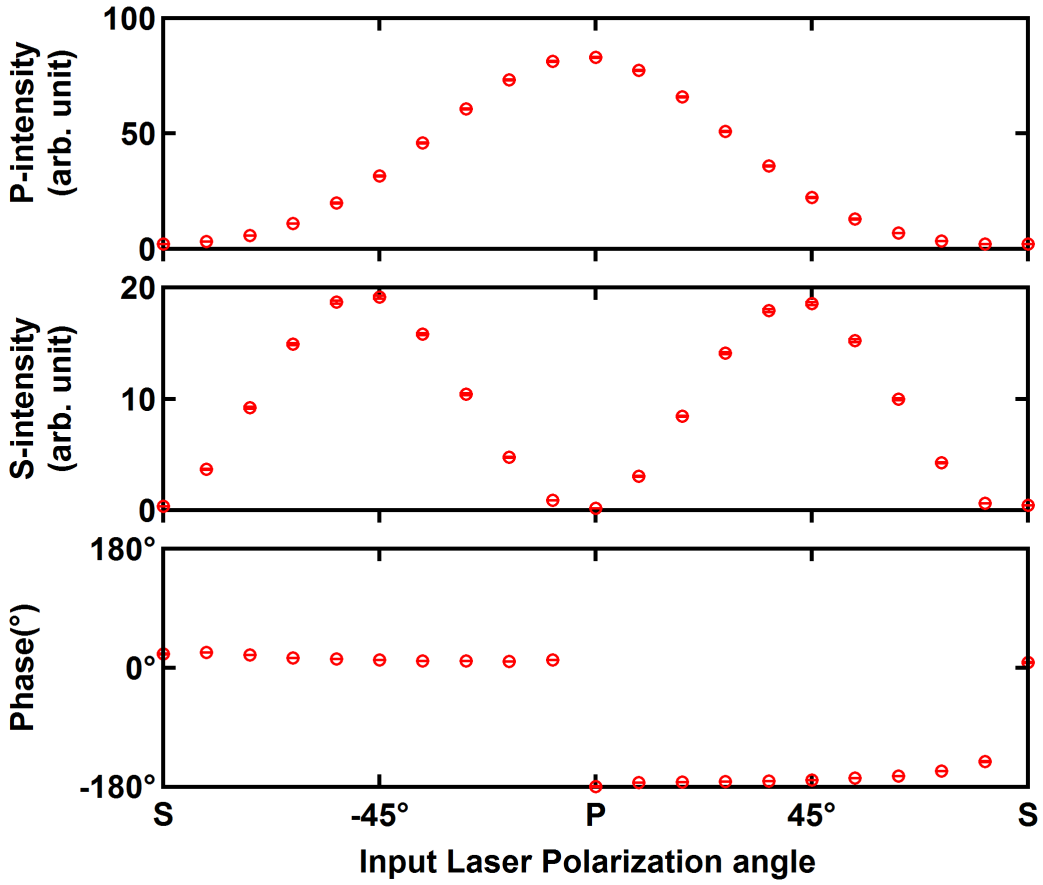

Figure 3.8: Second harmonic light generated from SiHJ device fitted to Equations (2.31) and (2.32). The input polarization was varied through a full rotation of the input half wave-plate, resulting in four full rotations of the input polarization vector. The fitting results for Short Circuit are $|\eta| = 0.522 \pm 0.040, \phi_\eta = -52.3° \pm 3.5°, |\kappa| = 0.813 \pm 0.06, \phi_\kappa = -118.943° \pm 3.0°$ with $\chi^2 = 3.5$. The fitting results for Open Circuit are $|\eta| = 0.596 \pm 0.023, \phi_\eta = -30.2° \pm 2.1°, |\kappa| = 0.738 \pm 0.028, \phi_\kappa = -129.4° \pm 2.0°$ with $\chi^2 = 4.4$.

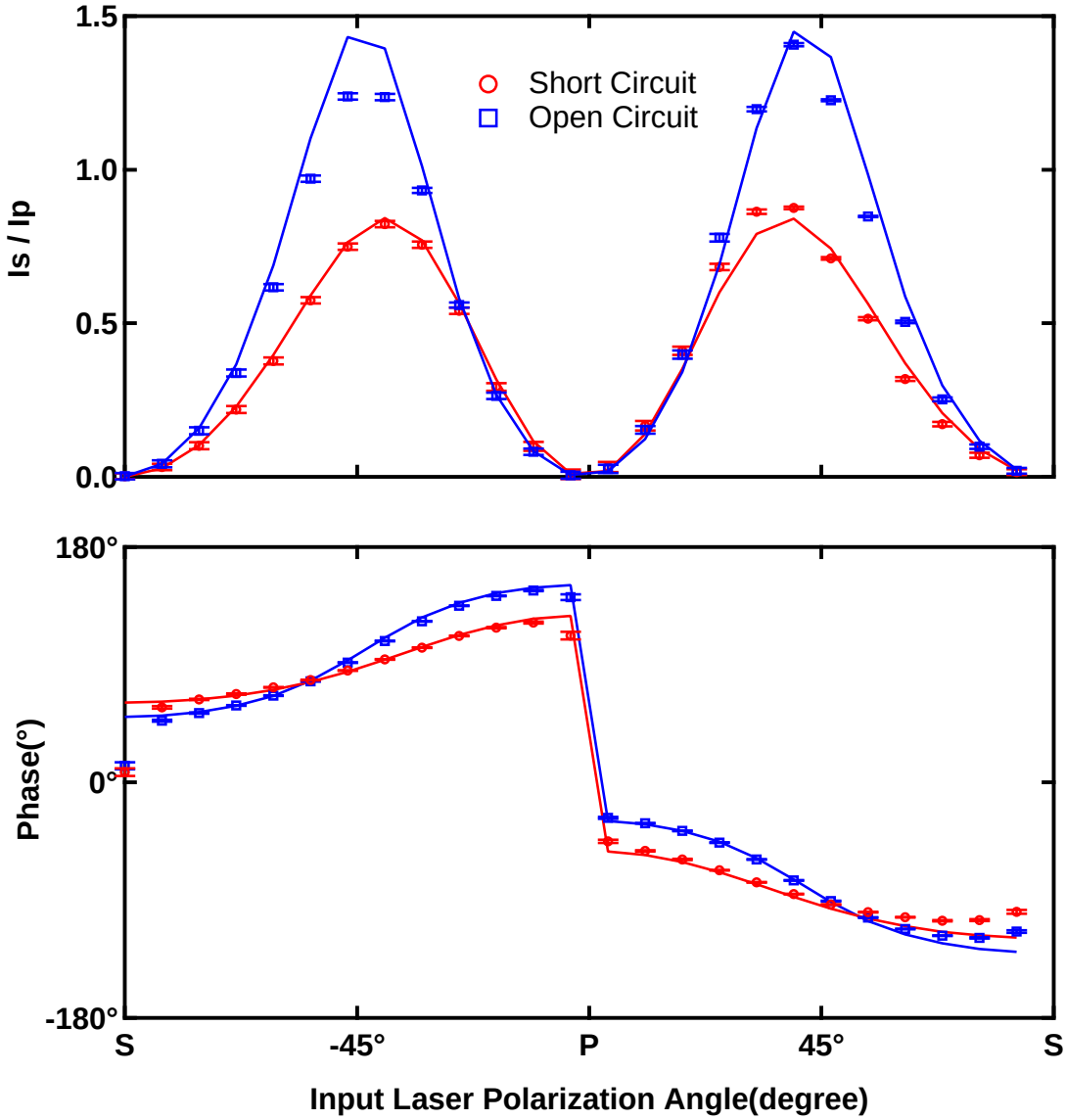

second harmonic light is the combination of multiple SHG interference from the buried interfaces and strong electric fields in the sample layer structure, the fitting indicates this complex SHG combination can be understood with a set of bias voltage dependent effective tensor elements.

3.3 SSHG vs Azimuthal Angle

SHG measurements as a function of sample rotation about the surface normal directly determine the underlying symmetry of the material and interfaces. In order to help quantify the portion of the signal arising from bulk, quadrupolar SHG in the c-Si, we measured the SHG signal as the sample was rotated about its surface normal (i.e, azimuthal scans) at different biases. Because the c-Si bulk is not isotropic, we expect any SHG signal from the c-Si bulk to change with azimuthal angle [61, 67, 82]. In Figure 3.9, we show data from azimuthal scans in the pP geometry under Short Circuit (SC) and Open Circuit (OC) conditions. There is a clear 1-fold and 4-fold dependence in the pP SHG data. There is also a strong signal that is independent of the azimuthal angle. We note that while the 4-fold variation is expected from the (weak) bulk c-Si contribution, the 1-fold contribution is not expected for an ideal (100) silicon surface [67]. The 1-fold variation can arise from surface steps at the c-Si surface, which result from the inevitable slight miscut of the (100) Si wafer. In order to examine the relationship between the SHG 1-fold variation and the wafer miscut, we intentionally fabricated a 6° mis-cutted (100) Si wafer. Due to the misalignment between the crystal axis and wafer surface normal, the angle between input laser and crystal angle will cycle between 39° and 51° with the wafer azimuthal rotation; therefore, it creates a significant 1-fold SHG variation in the azimuthal scan as seen in Figure 3.10.

A sinusoidal function is used to illustrate the 1-fold and 4-fold azimuthal SHG variation. To quantify these contributions, we fit the data in Figure 3.10 to the function:

$$SHG(\varphi) = |A_0 + A_1 e^{i\theta_1} \cos(\varphi - \varphi_1) + A_4 e^{i\theta_4} \cos[4(\varphi - \varphi_4)]|^2 \tag{3.1}$$

Although the sinusoidal function is not precise for depicting the details for the 1-fold variation

Figure 3.9: SHG intensity of pP geometry measured as the sample is rotated about its surface normal at Open and Short Circuit conditions. The solid lines are fits to Equation (3.1), and the fitted parameters are listed in Table 3.1.

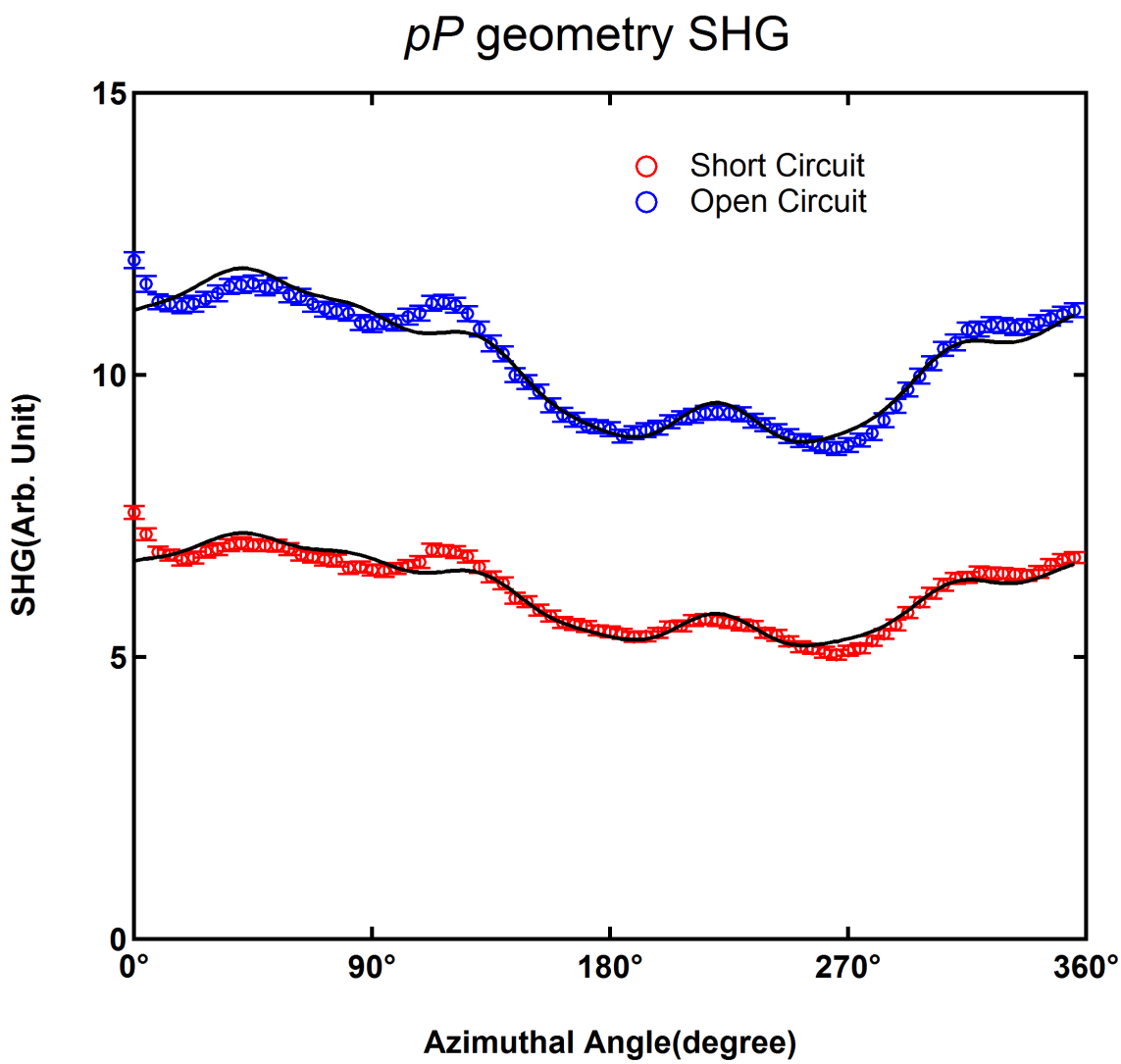

Figure 3.10: SHG intensity of pP geometry measured as the sample of 6° mis-cutted (100) Si wafer is rotated about its surface normal. The solid line is a fit to Equation (3.1), and the fitted parameters are listed in Table 3.1. This figure shows the stronger 1-fold modulation with increased surface miscut comparing to the azimuthal scan in Figure 3.9.

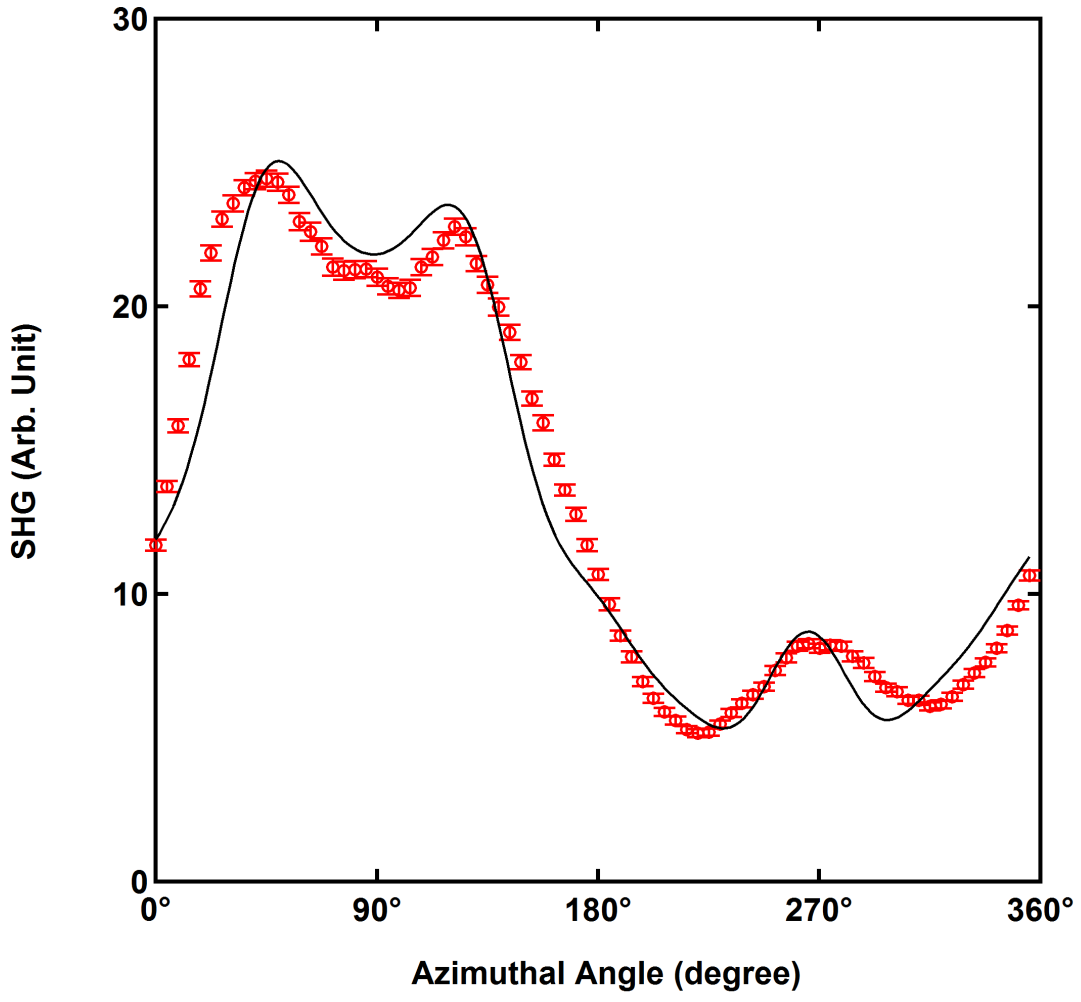

in Figure 3.10, the fitting line in the figure mostly catch the azimuthal SHG variation for the miscut Si wafer(the fitted parameters are listed in Table 3.1). The fitting successfully confirms that the anisotropic SHG contribution from c-Si wafer can be understood via Equation (3.1).

Qualitatively, this intensity can show an overall isotropic behavior, with 1-fold and 4-fold intensity arising from the cross term with the isotropic contribution, and additional 2-fold, 3-fold, 5-fold, and 8-fold intensity contributions due to various cross terms. In fact, the isotropic term is dominant, leading to the observed largely isotropic, 1-fold, and 4-fold contributions. The parameters A_0,A_1, and A_4 are the 0-fold isotropic, 1-fold and 4-fold contributions and the remaining parameters correspond to the relative phases between the electric fields and offsets in azimuthal angle ϕ. When we fitted the OC and SC data to Equation (3.1), the resulting fit parameters(see Table 3.1) in the second two terms of Equation (3.1) were identical (within error bar), indicating that the 1-fold and 4-fold contributions are independent of bias. The fits are shown as the solid lines in Figure 3.9. The fits result in typical 'goodness of fit' parameter χ^2 values of 3, dominated by the fact that the 1-fold contribution is not observed to be strictly sinusoidal with azimuthal angle as seen in Figure 3.10. The success of these fits confirm that there is little or no bias-dependence in the 1-fold and 4-fold second harmonic electric fields. The small size and bias-independence of A_4, in particular, indicates that the anisotropic bulk contributions to the SHG cannot explain the strong bias-dependence (in the pP geometry) in Figure 3.6.

The above analysis of the data in Figure 3.9 reveals that bulk, quadrupolar contributions are not responsible for the large bias dependence observed in Figures 3.3 and 3.6. Instead, the observed bias sensitivity of the SHG signal is an isotropic signal. It must arise from a combination of charge populations at the various material interfaces and electric fields that change with the application of bias in the SiHJ solar cell. In other words, the possible sources for the bias-dependent SHG are likely to be in the a-Si:H and its interfaces.

Table 3.1: Resulting fit parameters from least squares fitting of the SHG data to Figures 3.9 and 3.10. By comparing the Short Circuit and Open Circuit conditions for SiHJ solar cell, it is easy to notice that the major difference comes from the A_0 term, while other parameters, especially A_4, are within the uncertainty bar. This fitting results strongly suggests that the bulk silicon EFISH is not important in the overall bias-dependent SHG signal. The fitted A_1 for miscut Si wafer is much bigger than SiHJ solar cell. It confirms that the 1-fold SHG variation in Figure 3.9 arises from the small angle between the sample surface normal and silicon (100) direction.

Parameter	6° Miscut (100) Si Wafer	n wafer HIT cell (SC)	n wafer HIT cell (OC)
A_0(a.u.)	3.3101 ± 0.0046	2.4817 ± 0.0022	3.1842 ± 0.0034
A_1(a.u.)	2.114 ± 0.015	0.26 ± 0.024	0.305 ± 0.027
φ_1 (rad)	1.4230 ± 0.0035	0.815 ± 0.018	0.767 ± 0.015
θ_1 (rad)	-0.838 ± 0.005	0.84 ± 0.08	0.80 ± 0.09
A_4(a.u.)	0.790 ± 0.017	0.379 ± 0.039	0.417 ± 0.047
φ_4 (rad)	-0.347 ± 0.017	-0.33 ± 0.06	-0.32 ± 0.05
θ_4 (rad)	1.716 ± 0.006	1.681 ± 0.014	1.682 ± 0.014

3.4 ITO/a-Si:H interface isolation

We redesigned the layer structures of SiHJ solar cell by increasing the thickness of the p type amorphous silicon layer between ITO and c-Si wafer from 10 nm to 240 nm, and maintain the same configuration for the other layers in the device. Though the device performance changes from the classic SiHJ solar cell device which is optimize for best photon conversion efficiency, this redesigned device helps us separate the SHG contribution from multiple buried interfaces. Figure 3.11 shows the layer structures of the modified SiHJ solar cell and SHG contributions. The thicker a-Si:H layer is strongly absorptive for the SHG photons from a-Si:H/c-Si interface and c-Si bulk($\sim$30 nm penetration depth in a-Si:H for 3.02 eV photons [72]). As a result, the visible SHG signal arises only from the contribution of air/ITO, ITO/a-Si:H interfacial SHG and a-Si:H bulk EFISH.

In Figure 3.12, we present the SHG intensity of fixed input laser polarization at different voltage bias. It is interesting to notice the asymmetric pattern in Figure 3.12. The second harmonic intensity maintains constant in the forward bias region, while bias-dependent SHG signal of *pP,sP* and *mixS* geometries is greatly amplified in the reverse bias region. Thanks to the thick opaque thicker a-Si:H layer, the SHG photons from a-Si:H/c-Si interface and c-Si bulk are forbidden to escape; hence, those SHG contributions can be exclude from the bias-dependent SHG signal. What is more, the air/ITO interface is stable at different biases. Therefore, the possible sources for this bias-dependent signal are ITO/a-Si:H interface and strong electric field in a-Si:H bulk. This finding supports a hypothesis that the EFISH from a-Si:H bulk could be an important contribution to the bias-dependent SHG from SiHJ junction. In Chapter 4, we will develop a SHG interference theory to quantitatively understand these data. At the end of Chapter 4, the data in Figure 3.12 will be revisited.

3.5 Summary

In this chapter, we have presented various optical second harmonic generation measurements for SiHJ solar cell devices. Optical second harmonic generation is a promising characterization

Figure 3.11: The layer structures of the redesigned SiHJ device with thicker p-a-Si:H layer. The SHG in all geometries display asymmetric change in positive and negative bias region. We will revisit these data at the end of Chapter 4.

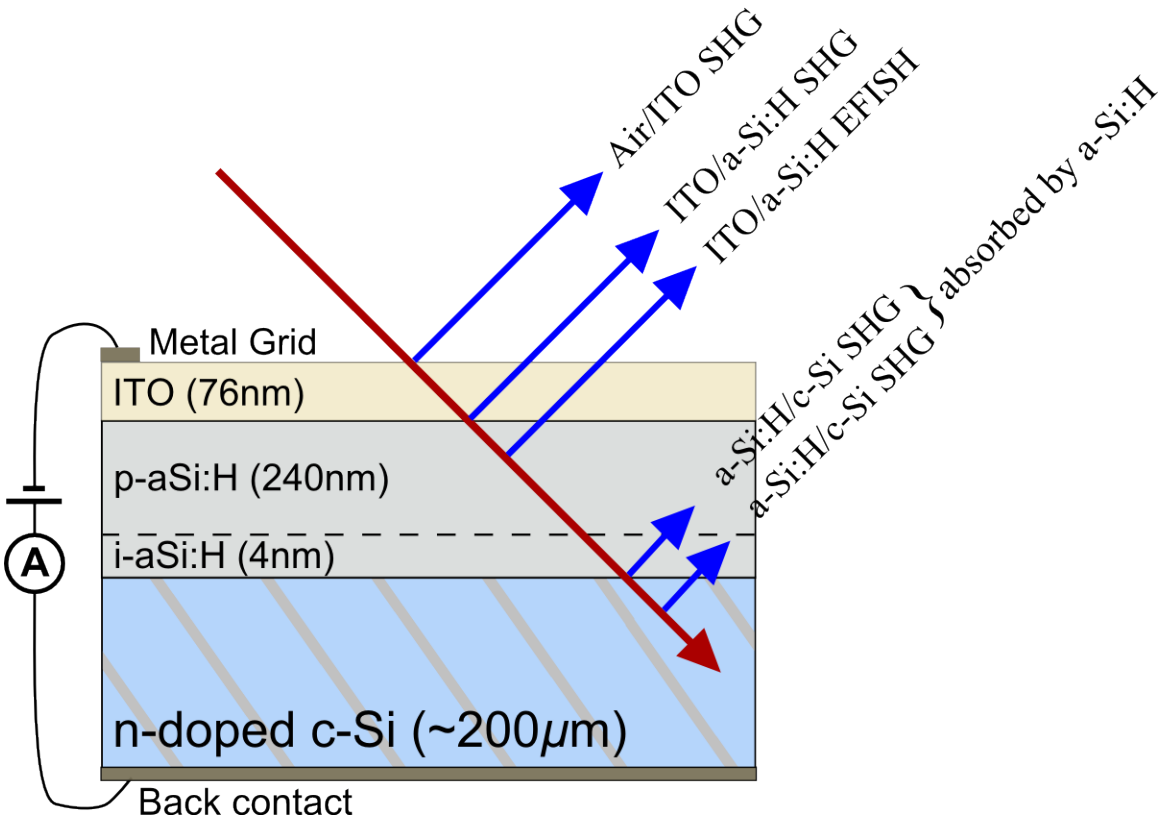

Figure 3.12: The measured SHG intensity at different bias for redesigned SiHJ device. The SHG in all geometries display asymmetric increase only in the negative bias region. This graph will be revisited at the end of Chapter 4.

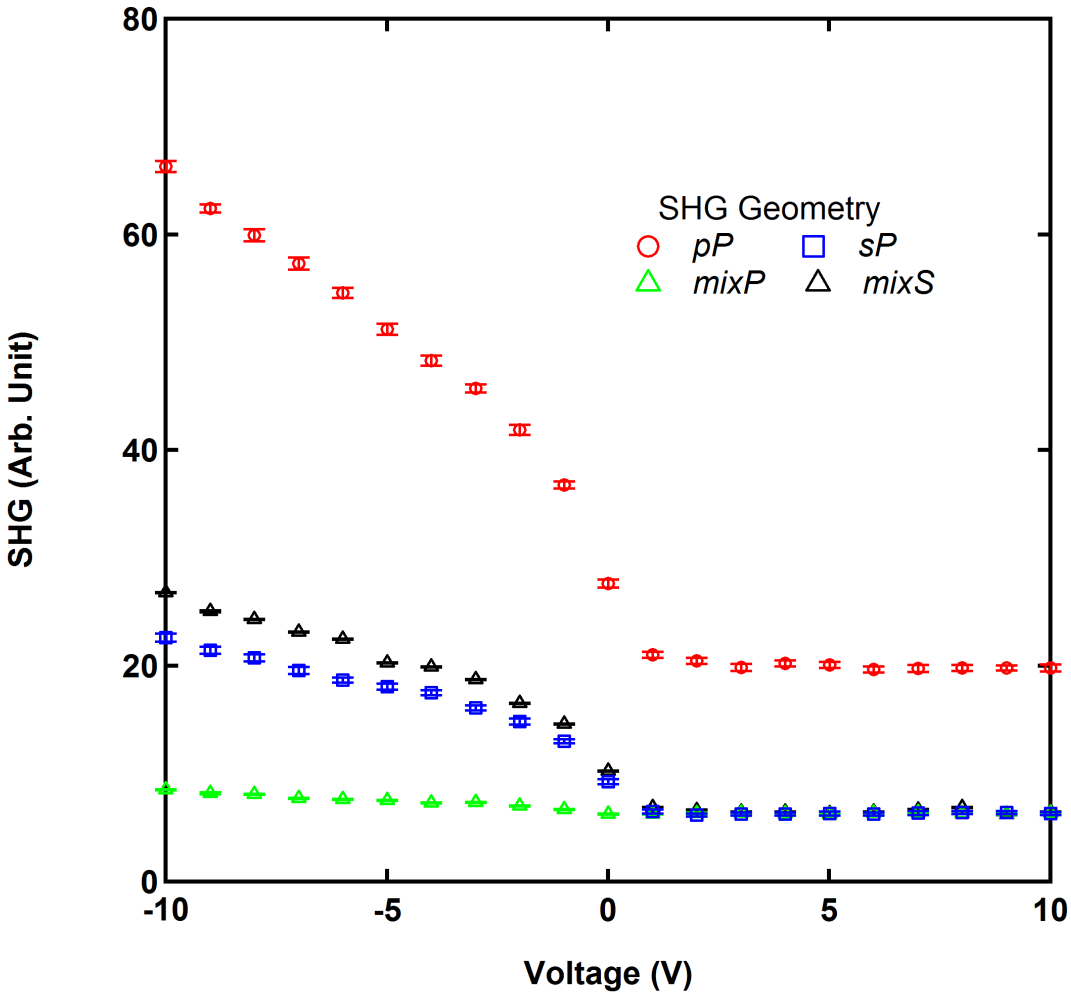

technique for photovoltaic devices because it is only sensitive to regions with broken inversion symmetry. This includes interfaces and areas with strong electric fields (both critical to device performance), but not the bulk of of amorphous and cubic materials. In initial measurements, we find that SHG from silicon heterojunction solar cells is very sensitive to changes in bias as the device is swept through a standard current-voltage curve. The azimuthal measurements show that c-Si bulk properties are not responsible for the bias dependence. The SHG measurement on the redesigned SiHJ device with thicker a-Si:H layer supports a picture where the bias-dependence signal comes from the Electric Field Induced Second Harmonic in a-Si:H bulk.

Chapter 4

SSHG on ITO/a-Si:H/ITO tri-layer sample

The results in Chapter 3 suggest strongly that the bias dependent SHG seen for HIT solar cells arise from EFISH in the a-Si layers. No previous report of EFISH existed in the literature, so we decided to measure it.

In order to study the EFISH contribution from the a-Si:H bulk, we fabricated various samples of ITO/a-Si:H/ITO "sandwich" structures. The ITO layers are thermally evaporated from metal sources in an oxygen atmosphere. The polycrystalline ITO has grains $\sim 1\mu m$ with no preferred crystallographic orientation and so is inversion symmetric over the probe laser size. The a-Si:H is deposited by hot-wire chemical vapor deposition (HWCVD) from pure SiH4 at $\sim$ 250°C using a $\sim$2000 °C W filament 5 cm from the substrate. The a-Si:H are "device quality" with a light:dark conductivity ratio of 2.8×10^5, as measured on a witness a-Si:H film on glass. Subsequent to deposition of the final ITO layer, 2.5 mm diameter device mesas are created by 1) patterning photoresist to protect the top ITO and a-Si:H layers, 2) etching the top ITO and a-Si:H and 3) removing the resist. With the front and back ITO contacts exposed, we bias the devices and measure current-voltage curves and SHG signals simultaneously. Two different layer structures have been studied. These structures differ principally in the thickness of the top-most ITO layer. The Sample type A structure (see Figure 4.1) is a thin-film stack (listed from substrate to top-most layer) of silica substrate / ITO(70nm) / a-Si:H($\sim$700nm) / ITO(5nm) structure. The Sample type B structure is Si Wafer / SiO2(native $\sim$2 nm) / ITO(70nm) / a-Si:H($\sim$700nm) / ITO(70nm). As we describe further below, the a-Si is thick enough to absorb any SHG from the back interfaces,

while the variation in distance between the ITO/air and a-Si/ITO interfaces allows us to more clearly study the a-Si EFISH.

Figure 4.1: shows the device structure of Sample A, bias geometry, and optical experimental configuration.

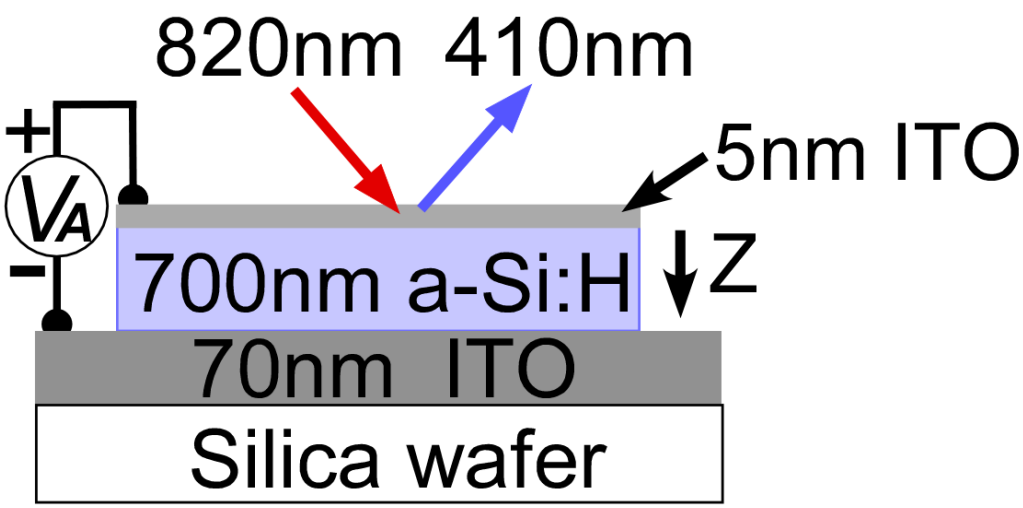

4.1 Bias Dependent SSHG

The ITO/a-Si:H/ITO devices respond electronically as "leaky" back-to-back diodes, and the dark I-V current (Figure 4.3) is limited by whichever interface is the reverse-biased junction. When the top a-Si:H/ITO junction is reverse biased ($V_A < 0$), there is an EFISH contribution to the SHG signal that arises from the strong electric field in the a-Si:H near the top ITO interface. However, when this junction is forward biased ($V_A > 0$), forward diode conduction prevents the weak electric fields at the front interface from varying significantly with V_A, while the strongest electric fields at the back interface are not observed in the measured SHG (due to finite SHG optical penetration at 410 nm).

Therefore, the measured SHG in Figure 4.4 arises from a superposition of EFISH and interface SHG from the air/ITO and top ITO/a-Si:H interface. Because the ITO is highly conductive, the static electric field in the ITO is small and largely V_A-independent; therefore, we assume EFISH

Figure 4.2: The picture of an actual "sandwich" device fabricated on silica wafer. The whole wafer has a size of 2.5cm X 2cm, with 4 X 4 circular mesas on the top. Each circular "sandwich" device features a diameter of 2.5 mm diameter.

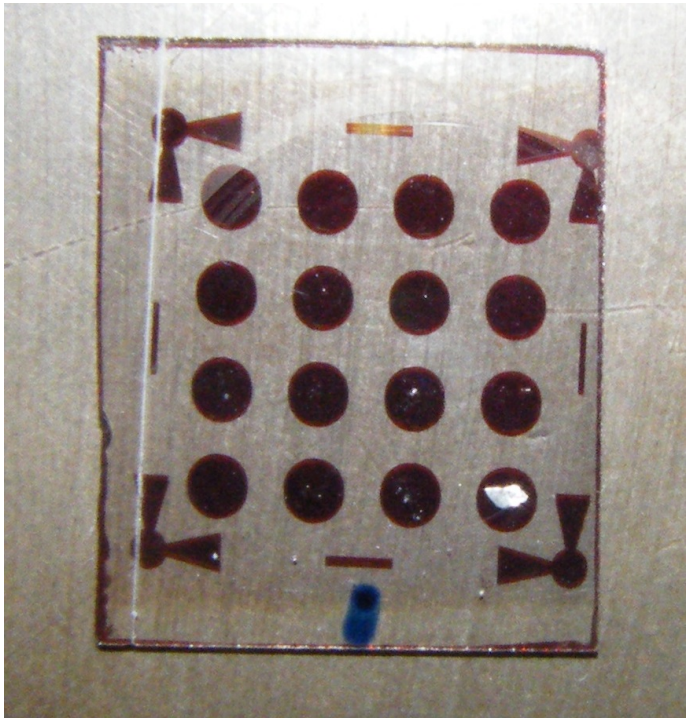

signals from the ITO are small. The superposition of the two ITO interface SHG signals then create a V_A-independent second harmonic "idler" field, $E_I^{(2\omega)}$. The total measured SHG intensity signal then arises from the superposition of $E_{EFISH}^{(2\omega)}$ and $E_I^{(2\omega)}$:

$$SHG \sim |E_I^{(2\omega)} + E_{EFISH}^{(2\omega)}(V_A)|^2 = |E_I^{(2\omega)}|^2 + |E_{EFISH}^{(2\omega)}(V_A)|^2 + 2E_I^{(2\omega)}E_{EFISH}^{(2\omega)}(V_A)cos(\delta) \quad (4.1)$$

Here, δ is the relative phase between the complex fields $E_{EFISH}^{(2\omega)}$ and $E_I^{(2\omega)}$.

For both samples, a-Si:H and air act as non-absorbing dielectrics at the pump laser wavelength. In Sample A, the top ITO layer is thin (5nm) and inversion symmetry is nearly restored, resulting in the observed very small idler contribution as seen in other dielectric/dielectric interfaces. In this case, $E_{EFISH}^{(2\omega)} >> E_I^{(2\omega)}$ and the total SHG is dominated by the second term in Equation (4.1). Qualitatively, the Sample A SHG has a linear V_A-dependence in reverse bias (see Figure 4.5). In Sample B, the thicker top ITO physically separates the ITO/air and a-Si/ITO interfaces. SHG generated at these interfaces can constructively interfere and there is significant idler contribution $E_{EFISH}^{(2\omega)}$. Thus, the SHG from Sample B arises predominantly from the first and third terms in Equation (4.1). Qualitatively, the Sample B SHG has a sub-linear V_A-dependence with the top junction in reverse bias (see Figure 4.7).

4.2 SHG and EFISH interference theory for a-Si:H/ITO interface

To obtain a quantitative understanding of the data, we generalize traditional interfacial SHG treatments [60] and assign three complex vectors to both the idler SHG and EFISH signals: ($p\vec{P}_{idler}$, $s\vec{P}_{idler}$, $m\vec{ix}S_{idler}$) for $E_I^{(2\omega)}$ and ($p\vec{P}_{EFISH}$, $s\vec{P}_{EFISH}$, $m\vec{ix}S_{EFISH}$) for $E_{EFISH}^{(2\omega)}$. For both Sample A and B, we then simultaneously fitted the SHG variation with both input polarization and V_A to:

$$\begin{aligned} I_p(\phi, V_A) &= |\vec{E_p}|^2 \\ &= |cos^2\phi(\overrightarrow{pP}_{idler} + \overrightarrow{pP}_{EFISH}\sqrt{V_{BI} - V_A}) + sin^2\phi(\overrightarrow{sP}_{idler} + \overrightarrow{sP}_{EFISH}\sqrt{V_{BI} - V_A})|^2 \quad (4.2) \end{aligned}$$

Figure 4.3: shows measured JV curve on Sample A. This JV curve obeys a weakly non-linear back-to-back diode behavior.

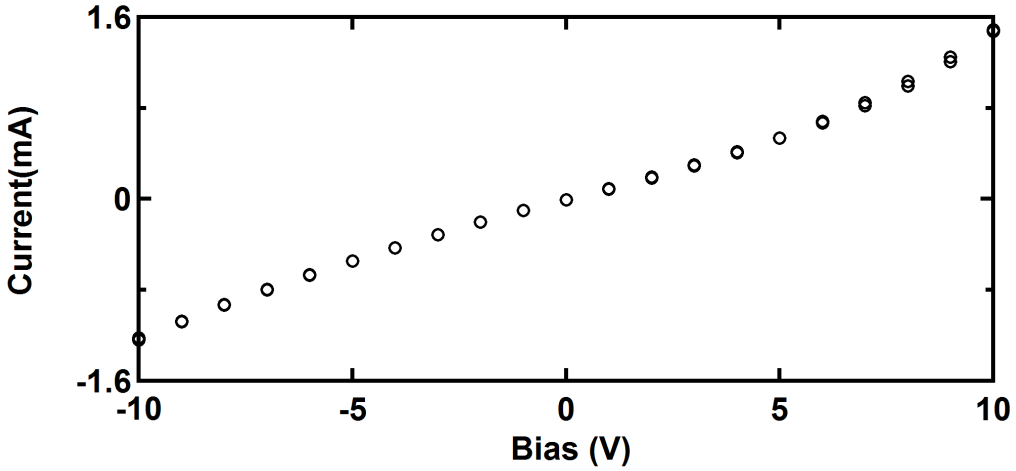

Figure 4.4: Measured second harmonic intensity and relative phase for Sample A as a function of input laser polarization at three different device voltage biases (V_A). In upper panel, we plot the p-polarized SHG intensity. In mid panel, we plot the s-polarized SHG intensity. In bottom panel, we plot relative phase of the p and s polarized SHG. The 0V and +10V data in (a) and (b) are scaled by 5X to improve visibility. Solid lines are the fitting result, as described in the text. The inset shows the device structure of Sample A, bias geometry, and optical experimental configuration.

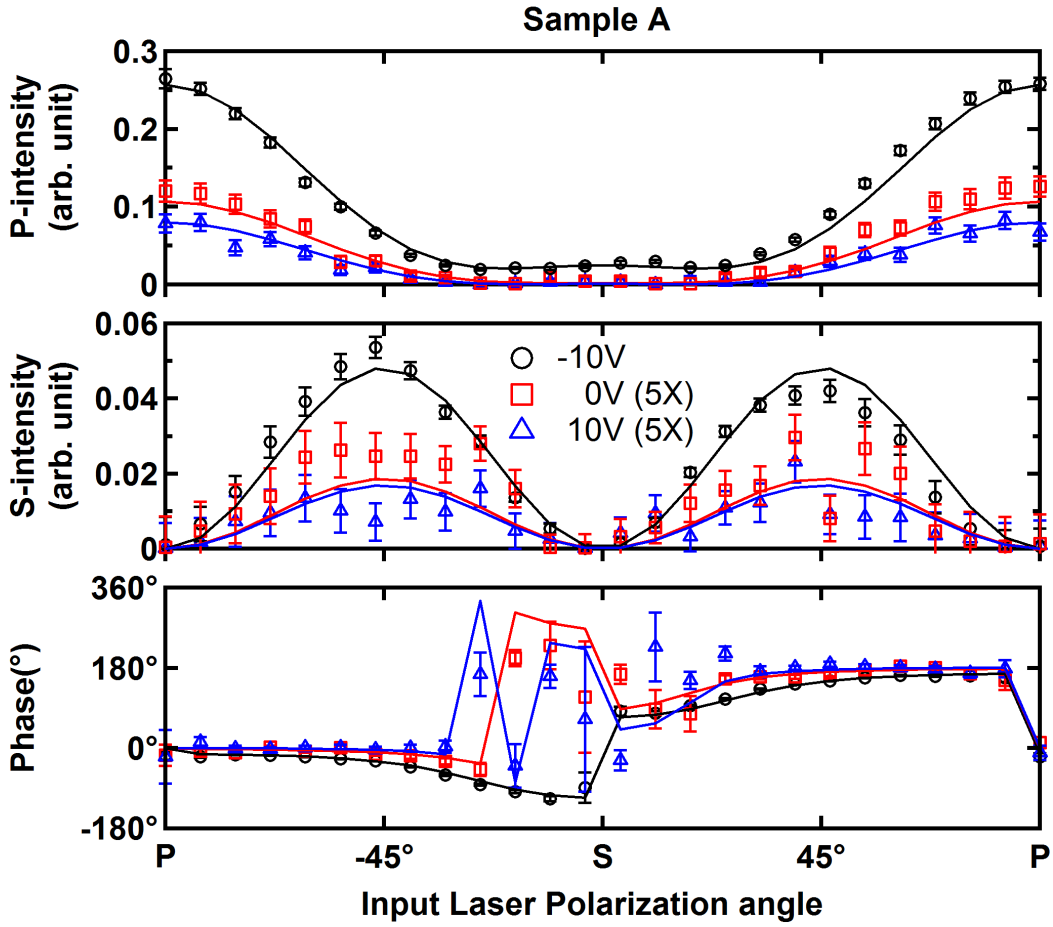

Figure 4.5: Second harmonic intensity and relative phase as a function of applied bias voltage. In upper panel, the SHG intensity is shown for different input laser polarizations: red circles: pP, blue squares: sP, green point-up triangles: $mixP$, black point-down triangles: $mixS$. Mid panel show the phase difference between the $mixP$ and $mixS$ SHG signal. Bottom panel show the IV curves. Solid lines are fits to Equations (4.2) to (4.4), as described in the text. The resulting fit parameters are listed in Table 4.1. The increasing Sample B SHG signal for $V_A > 5$V cannot be explained by the physics underlying the fit equations and so is not fitted.

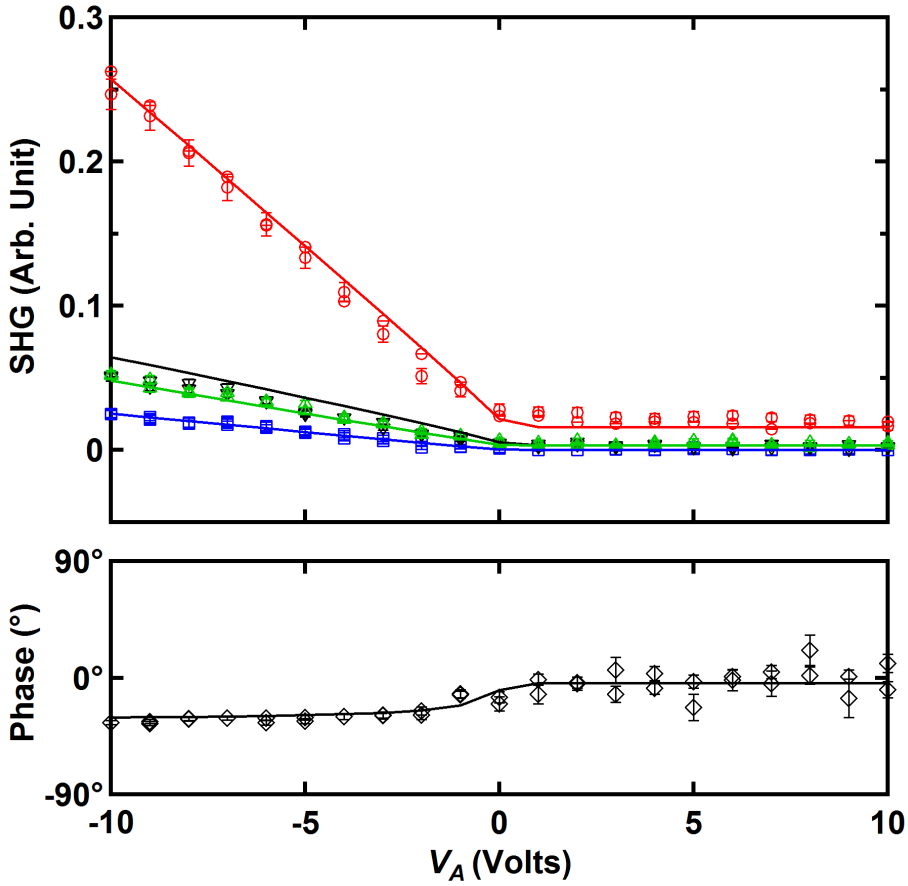

$$I_s(\phi, V_A) = |\overrightarrow{E_s}|^2 = |2cos\phi sin\phi(\overrightarrow{mixS}_{idler} + \overrightarrow{mixS}_{EFISH}\sqrt{V_{BI} - V_A})|^2 \tag{4.3}$$

$$\Delta = arg(E_p/E_s) \tag{4.4}$$

The solid lines in Figures 4.4 to 4.7 are the fit result. We did not fit Sample B at $V_A > 5$V (see below). In Equations (4.2) to (4.4), we have assumed $E^{(2\omega)}_{EFISH} \sim \sqrt{V_{BI} - V_A}$. Here, I_p, I_s, $\vec{E_p}$ and $\vec{E_s}$ are p and s polarized SHG light intensity and field vectors, Δ is the phase difference between $\vec{E_p}$ and $\vec{E_s}$, and ϕ is the input light polarization angle, measured from p-polarization. The $\overrightarrow{pP}_{idler}$ phase is fixed to zero, as our measurement is not sensitive to the overall phase. To account for the small electric field variation near the top ITO/a-Si:H interface in forward bias, we set $\sqrt{V_{BI} - V_A} = 0$ for $V_A > V_{BI}$. This fitting, therefore, assumes there are only V_A-independent idler contributions in forward bias.

To provide a rough scale of second harmonic yield, we compare the SHG from Sample A at V_A = -10V in the pP geometry (EFISH dominated) to the SHG from a reference Al film described in Chaz's thesis under identical measurement conditions: the Sample A SHG signal is ~3 times larger than that found from the aluminum film, indicating that EFISH from a-Si can be a bright source of second harmonic photons, comparable to metal layers in device structures. The physics underlying the fitting cannot account for the increasing SHG in Sample B for $V_A > 5$V; therefore, we did not fit this data. The increasing SHG signal could arise from fields associated with the leakage through the reverse-biased diode. Also fitted and shown in Table 4.1 are values for the a-Si/ITO built-in voltage V_{BI}. These successful fits reveal that the electric field is proportional to $\sqrt{V_{BI} - V_A}$ in the near-interface region of both samples and that the different SHG V_A-dependences (Figures 4.5 and 4.7) arise from differences in the idler contribution (Table 4.1) interfering with the EFISH contribution.

We have measured and fit the SHG response of a variety of a-Si:H trilayer samples similar to Samples A and B, including samples where the top ITO layer is replaced with ~ 5 nm Cr contact, a material that is often used in EFISH studies of c-Si. In all the measured samples, the SHG V_A-dependence is well fitted by Equations (4.2) to (4.4), in which we have assumed

Figure 4.6: Measured second harmonic intensity and relative phase for Sample B as a function of input laser polarization at three different device voltage biases (V_A). In upper panel, we plot the p-polarized SHG intensity. In mid panel, we plot the s-polarized SHG intensity. In bottom panel, we plot relative phase of the p and s polarized SHG. The +10V data is not fitted due to device voltage leakage. Solid lines are the fitting result, as described in the text.

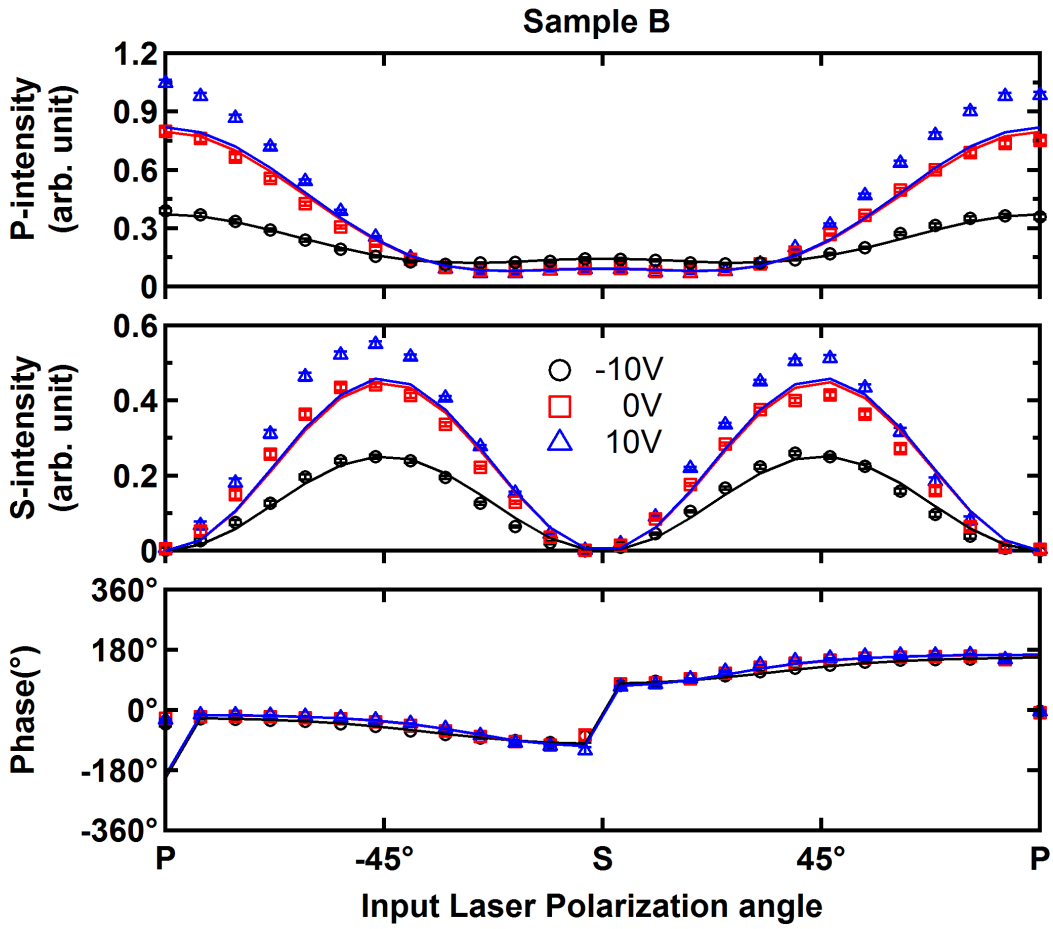

Figure 4.7: Second harmonic intensity in upper panel, relative phase in mid panel, and current in bottom panel as a function of applied bias voltage. In upper panel, the SHG intensity is shown for different input laser polarizations: red circles: pP, blue squares: sP, green point-up triangles: $mixP$, black point-down triangles: $mixS$. Mid panel shows the phase difference between the mixP and mixS SHG signal. Bottom panel shows the I-V curves. Solid lines are fits to Equations (4.2) to (4.4), as described in the text. The resulting fit parameters are listed in Table 4.1. The increasing Sample B SHG signal for $V_A > 5$V cannot be explained by the physics underlying the fit equations and so is not fitted.

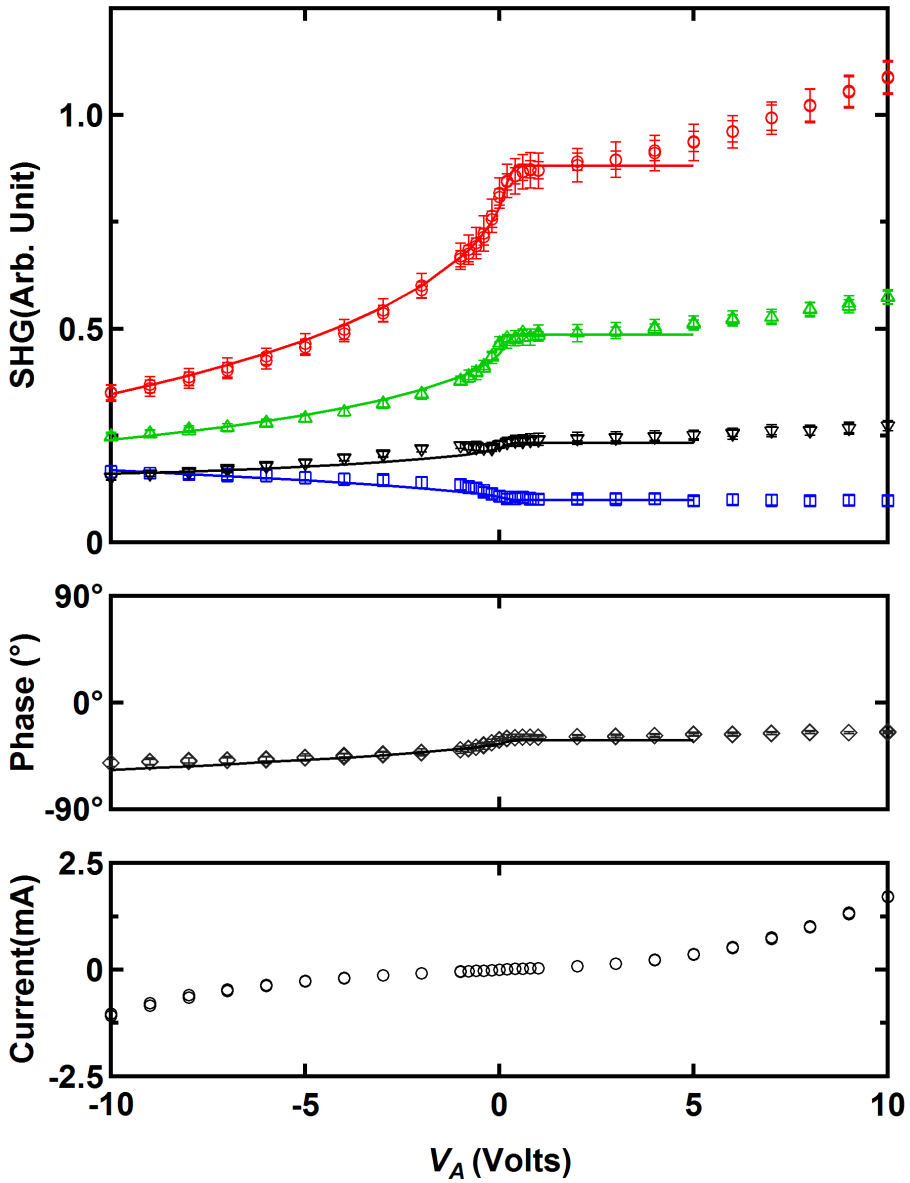

Table 4.1: Resulting fit parameters from least squares fitting of the SHG data to Equations (4.2) to (4.4). The solid lines in Figures 4.4 to 4.7 show the fit results.

Parameter	Sample A	Sample B
Magnitude(arb. unit) / Phase(Degree)		
$\overrightarrow{pP}_{idler}$	0.1264 ±0.0013 / 0 °	0.9389 ±0.0008 / 0 °
$\boldsymbol{\overrightarrow{pP}_{EFISH}}$	**0.1494 ±0.0020 / 83.0 °±3.0 °**	**0.1102 ±0.0006 / -174.4 ° ±1.5 °**
$\overrightarrow{SP}_{idler}$	0.0148 ±0.0010 / -139.2 °±4.2 °	0.3144 ±0.0007 / -94.40 ° ±0.15 °
$\boldsymbol{\overrightarrow{SP}_{EFISH}}$	**0.0516 ±0.0005 / -25.2 °±2.8 °**	**0.0436 ±0.0013 / -40.0 ° ±2.0 °**
$\overrightarrow{mixS}_{idler}$	0.0581 ±0.0010 / -0.7 °±0.7 °	0.6974 ±0.0004 / 12.81 ° ±0.05 °
$\boldsymbol{\overrightarrow{mixS}_{EFISH}}$	**0.0687 ±0.0009 / 96.5 °±2.9 °**	**0.0736 ±0.0013 / 169.7 ° ±1.5 °**
V_{BI} (V)	0.160 ±0.025	0.239 ±0.005

$E_{EFISH}^{(2\omega)} \sim \sqrt{V_{BI} - V_A}$. The similar behavior of Cr capped samples strongly suggests that V_A-dependent SHG from the top ITO surface does not contribute significantly to the fitted response.

In high reverse bias, where V_A is greater than any built-in fields, the electric field in the bulk of the semiconductor (as for any ohmic material) is linear in V_A. In interfacial regions, the high a-Si:H bandtail trap densities can screen E_z^{DC}. Könenkamp et al. [83, 84] have probed electric fields in the ∼500 nm near i-p a-Si:H interfaces at V_A <2 V with time-of-flight measurements that had a resolution of ∼80 nm. They find that the space charge density at this interface is well modeled by an exponential spatial dependence $\sim \exp(-x/L_0)$ with a characteristic length L_0, of roughly 210 nm. The associated electric field and potential spatial dependences are then both exponential, leading to an electric field that is again proportional to the voltage. The SHG measurements probe only the top 30 nm of the a-Si:H layer, closest to the ITO interface. Thus, EFISH measurements provide improved depth resolution. The observed $E_Z^{DC} \sim \sqrt{V_{BI} - V_A}$ dependence at the a-Si:H / ITO interface could arise naturally from full depletion of the band-edge states as described in Chapter 2: The observed $V_{BI} \sim 200$ mV is large compared to the energy width of the band tail states, ∼20mV [68]. Therefore, we expect that all the defect states and donor states near the interface are ionized, leading to a spatially uniform space-charge density. As for simple Schottky interfaces, uniform space-charge implies a linear spatial variation of E_Z^{DC}, a quadratic spatial variation in potential, and therefore a square-root dependence of E_Z^{DC} with potential.

4.3 SiHJ PV Devices Revisited

In the sections above, we have successfully developed a interfacial SHG and bulk EFISH interference theory to explain the bias-dependent SHG signal from a-Si:H trilayer structure. This theory is very helpful for understanding the bias-dependent SHG from HIT devices. In this section, I apply the SHG and EFISH interference theory to understand the SHG data from SiHJ PV devices with a thick a-Si:H layer mentioned in Chapter 3.

As we promised in Chapter 3, we discuss the SHG data from a redesigned HIT solar cell device shown in Figure 3.12 again. The layer structures of this redesigned device the same configuration

for the other HIT devices (Figure 3.1), but we increased the thickness of the p type amorphous silicon layer between ITO and c-Si wafer from 10 nm to 240 nm (Figure 3.11). Though the device performance changes from the classic SiHJ solar cell device which is optimize for best photon conversion efficiency, this redesigned device helps us separate the SHG contribution from multiple buried interfaces. Due to the same SHG mechanism for trilayer devices of Sample Type B, the visible SHG photon only comes from air/ITO, ITO/a-Si:H and a-Si:H bulk. This is the same configuration for the trilayer devices we have discussed in the above sections. Therefore, we apply the same interference theory and fitting functions to understand the bias-dependent SHG data from input polarization scan and SHG vs bias sweep.

The fitting shown in Figures 4.8 and 4.9 clearly catch the asymmetric behavior in the reverse bias region. It indicate that the E-field behavior at ITO/a-Si:H interface can be explained by Schottky physics similar as we described in the last section. Further more, this result also support our hypothesis in Chapter 3 that the bias-dependent SHG signal comes from the EFISH in a-Si:H layer.

4.4 Summary

We have shown that SHG can probe the interfacial region of ITO/a-Si:H. The EFISH signal is proportional to the reverse bias on the ITO/a-Si:H junction. The linear relationship between EFISH in a-Si:H and bias is also confirmed to exist on Cr/a-Si:H junction. The whole EFISH signal can be explained by that the behavior of the space charge region of a Schottky junction, indicating all the defect states and donor states in the a-Si:H are ionized, leading to a spatially uniform space-charge density in the region near the interface ITO/a-Si:H junction. The interference theory of the idler interfacial SHG and EFISH quantitatively explained the asymmetric bias-dependent SHG behavior in the redesigned HIT device with a thick a-Si:H layer. In summary, the EFISH we find in the sample trilayer a-Si devices then does an excellent job in explaining the variations in SHG observed in the SiHJ photovoltaic devices.

Figure 4.8: The SHG vs bias sweep data and the fitting results for the thick a-Si HIT device. Second harmonic intensity in upper panel, relative phase in mid panel, and current in bottom panel as a function of applied bias voltage. In upper panel, the SHG intensity is shown for different input laser polarizations: red circles: pP, blue squares: sP, green point-up triangles: $mixP$, black point-down triangles: $mixS$. Mid panel shows the phase difference between the mixP and mixS SHG signal. Bottom panel shows the I-V curves. Solid lines are fits to Equations (4.2) to (4.4), as described in the text. The resulting fit parameters are listed in Table 4.2.

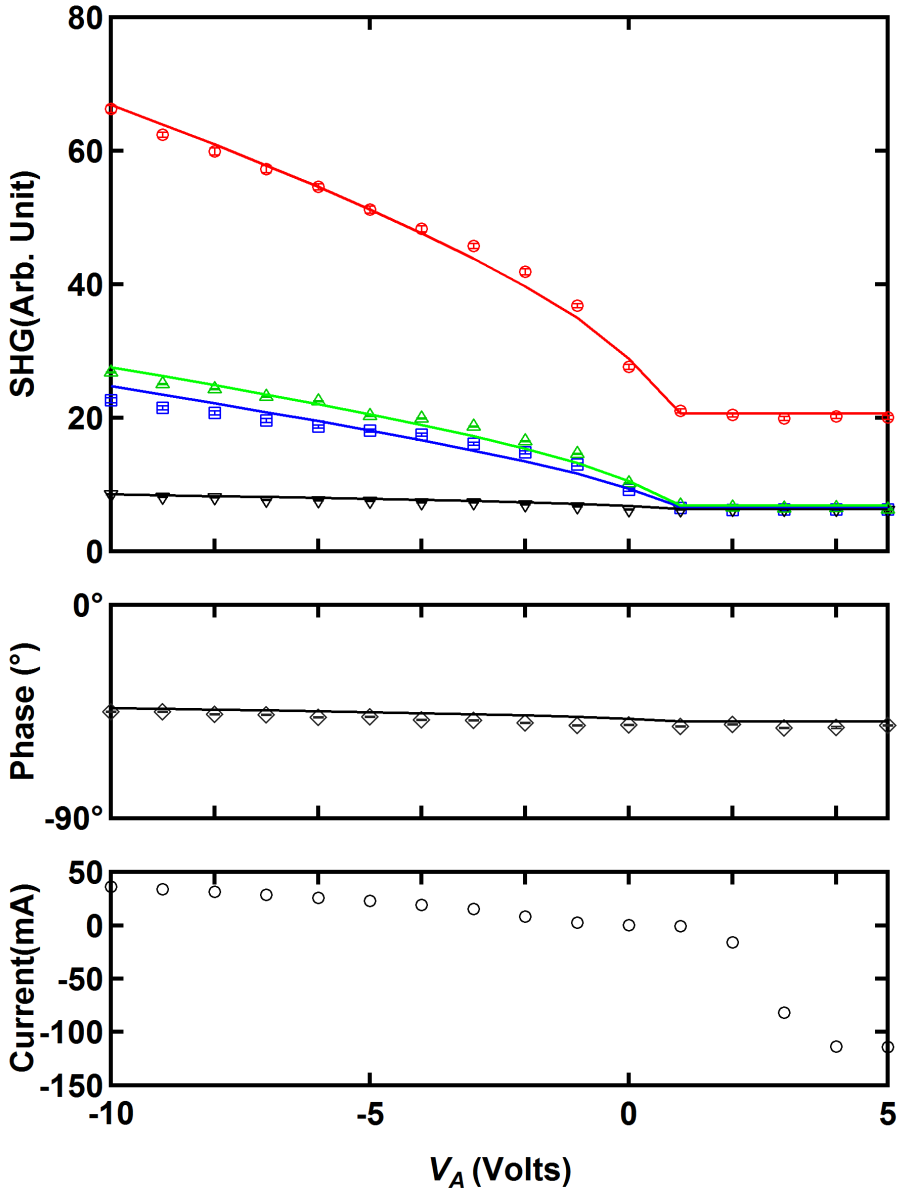

Figure 4.9: Measured second harmonic intensity and relative phase for thick a-Si HIT device as a function of input laser polarization at Short Circuit (0V) and Open Circuit (0.5V). In upper panel, we plot the p-polarized SHG intensity. In mid panel, we plot the s-polarized SHG intensity. In bottom panel, we plot relative phase of the p and s polarized SHG. Solid lines are the fitting result, as described in the text.

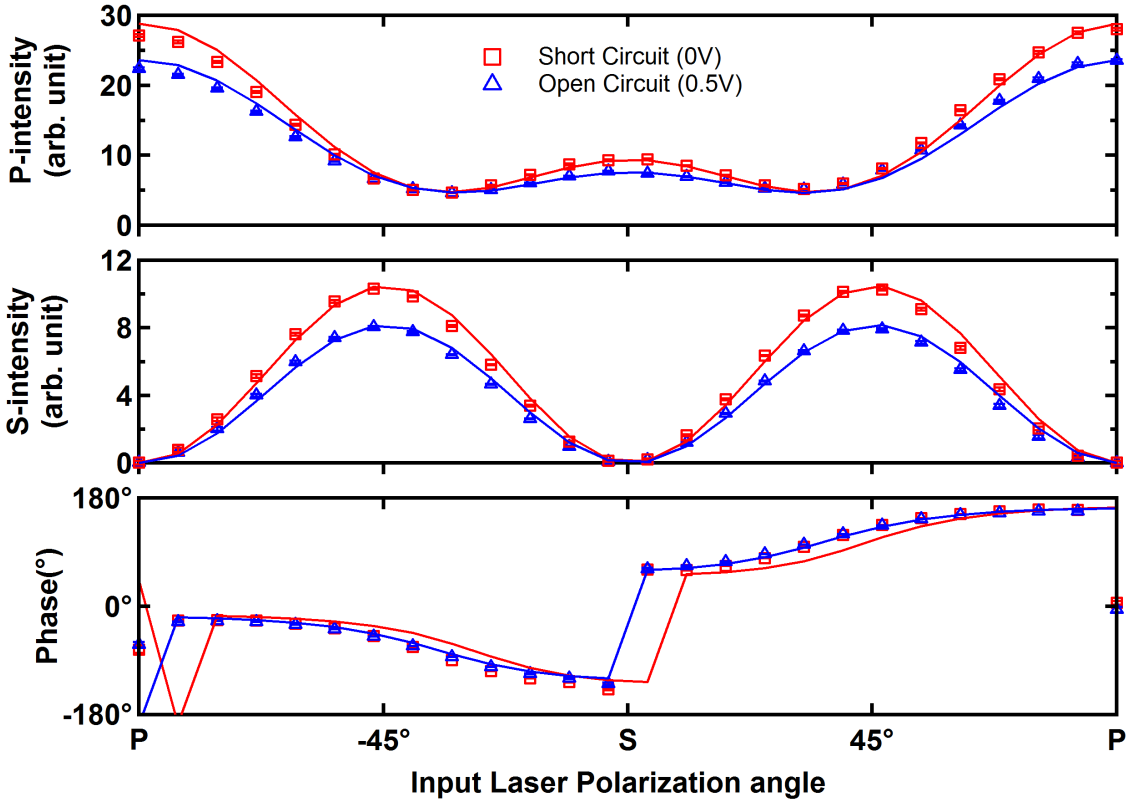

Table 4.2: Resulting fit parameters from least squares fitting of the SHG data to Equations (4.2) to (4.4). The solid lines in Figures 4.8 and 4.9 show the fit results.

Parameter		HIT solar cell with thick a-Si:H layer
Magnitude(arb. unit) / Phase(Degree)	$\overrightarrow{pP}_{idler}$	4.55195 ± 0.005/ 0 °
	$\boldsymbol{\overrightarrow{pP}_{EFISH}}$	**1.202 ± 0.007 / 29.7 °±0.9 °**
	$\overrightarrow{SP}_{idler}$	2.5828 ± 0.0035 / -95.9 °±0.10 °
	$\boldsymbol{\overrightarrow{SP}_{EFISH}}$	**0.900 ± 0.007 / -146.8 °±0.7 °**
	$\overrightarrow{mixS}_{idler}$	0.8119 ± 0.0014 / 19.22 °±0.06 °
	$\boldsymbol{\overrightarrow{mixS}_{EFISH}}$	**0.445 ± 0.016 / 25.5 °±0.9 °**
V_{BI} (V)		0.5855 ± 0.0018

Chapter 5

SHG Dynamics on ITO/a-Si:H/ITO tri-layer sample

In Chapter 4, we showed that a-Si EFISH is a significant source of SHG and that it can explain much of the variation in SHG we have observed in HIT PV devices. In this Chapter, we show how to use the EFISH to help us understand the time dependence of the internal E-field in a-Si semiconductor devices.

Among the most useful methods used to characterize semiconductors are capacitance-voltage(C-V) profiling measurements [85, 86, 87, 88]. In amorphous silicon, however, or indeed any semiconductor with a large concentration of deep gap states, such techniques are difficult to interpret. The depletion region, bulk states, free carriers and rear interface in a semiconductor device all contribute to the C-V response and an accurate C-V interpretation requires carefully separating these contributions. For example, A. Rolland and J.P. Kleider [89, 90] proposed a multiple capacitor circuit model to understand the C-V measurements of a-Si:H of metal insulator semiconductor(MIS) structure in the quasi-static regime. However, they were unable to determine the actual physical location of each capacitor in the complex device. Which interfaces contribute to various capacitors is an open question we wish to study.

In last chapter, we have proved that the EFISH intensity is proportional to the static voltage magnitude in the reverse bias region. This linear relationship comes from the electric field induced by the space charge region. By probing the time-resolved electric field with time-resolved SHG, we can directly probe carrier dynamics in the depletion region of a ITO/a-Si:H junction. Here, we overcome the challenges of stand-alone current-voltage measurements by combining C-V and

SHG measurements. While, C-V measures the dynamic response of the entire structure, SHG probes only the front ITO/a-Si:H depletion region. Together, current-voltage and dynamic SHG measurements allow us to directly study charge motion at the ITO/a-Si:H interface.

5.1 Experimental Setup

It is an interesting question about how to take dynamical data in an experiment where the signal comes as discrete photon counts. For static situations as in Chapters 3 and 4, we simply set the conditions such as bias voltage or polarization angle, and then acquire photon counts until we have enough counts to provide the desired signal-to-noise ratio. In the case of dynamical conditions, it is necessary to correlate the arrival of a photon with the conditions that are in place at that particular moment. That means acquiring photon counts and recording not only how many have arrived, but also when they have arrived relative to some trigger or stimulus. One standard approach to do this job is to use a Time-to-Amplitude Converter (TAC) and a multi-channel analyzer...

In the static situation, we count SHG photons with SRS300 photon counter. For dynamics SHG measurement, it is natural to use a combination of Time-to-Amplitude Converter(TAC) and Multi-Channel Analyser(MCA) to obtain time-resolved SHG signal on the time range from 100ns to 1ms. However, the TAC-MCA system is throttled by double counting blinding effect. This drawback comes from that TAC is only designed as a low order count device. For example, when TAC offers a range of T and two pulses are feeded into the TAC within window T, the second pulse will be ignored by the TAC. Therefore, TAC can only count the signal with a rate $<1/T$. In order to minimize this double pulse coincidence within the same window T, the signal fed to TAC should be slower than 1/10T, which means low SHG intensity. As a result, TAC-MCA system needs a long average time to achieve the desired signal-to-noise ratio. To overcome this limitation, I have developed new system with a reliable data acquisition of much faster rate.

We use an AlazarTech ATS9440 digitizer to measure the SHG photon pulses directly. The ATS9440 digitizer provides a 14-bit analog-to-digital converter, 125 Mega-Sample/sec(MS/s) which allows maximum temporal resolution of 8ns. More importantly, it offers Dual-port Memory mode

that increases the data acquisition rate with remarkable duty cycle (>95%). In other words, it allows >95% SHG photon capture during the SHG data acquisition time window, comparing <10% photon capture by Single-port Memory mode. This is very important to achieve desired signal-to-noise ratio within a relatively short time. Whoever is interested in the details of this technique is encouraged to read more in the ATS9440 manual. The paragraphs below will go through more technical details of how to use this instrument for SHG photon averaging.

When sending the sequence of voltage wave(sinusoidal, triangle or square wave) to the tri-layer sample, the voltage wave also provides the trigger to the ATS9440 to maintain identical piece of wave cycle for each temporal SHG measurement. Each trigger on ATS9440 produces a piece of array containing the SHG measurement wave. After billions of arrays averaged, the SHG photon intensity as a function of time will be profiled by a series samples with time interval specified by the sampling rate of ATS9440. Eventually, at each time sampling point, the SHG intensity is obtained by averaging billions of measurement of SHG pulses.

Since each sample from ATS9440 occupies a 2 byte memory, 125MS/sec sampling rate is equivalent to 250MByte/sec(MB/s) data production rate. In a dark SHG intensity scenario, more than 30 minutes of continuous data acquisition is necessary to reach desired the signal-to-noise ratio. The total data size for this time window is estimated by "$250 MByte/sec \times 60 secs/mins \times 30 mins$ = 450GByte". During this data acquisition process, the ATS9440 continues filling the 2GB onboard memory with traces at the rate of 250MB/s, while the desktop retrieves the data from ATS9440 to motherboard memory and processes it. For each iteration, the computer needs to process the retrieved trace for calculating the eventual average value. It is necessary for the computer to retrieve the value trace from ATS9440's onboard memory and process it faster than 250MByte/sec to avoid the memory overflow on ATS9440. To achieve this fast processing speed, it is important that the computer system (CPU, memory transportation) is overclocked and Labview process is set to be "high priority" in the Windows operation system. What is more, the trace size needs to be careful selected for maximum transferring speed between ATS9440 and desktop motherboard.

The system best temporal resolution is mainly constrained by the sampling rate of ATS9440.

The maximum 125MS/s defines the upper bound of the resolution as 8ns. At the same time, the SHG photon pulse width needs deliberation to cooperate with the sampling rate. On one hand, the pulse width need to be greater than 8ns for not being missed in the sampling gap. On the other hand, the pulse width needs to be small to avoid the multiple sampling which deteriorates the temporal resolution. In order to achieve the best resolution and 100% SHG photon capture, the ideal width of pulse fed to ATS9440 should be in the range of 8∼16ns.

For the current tri-layer sample and laser conditions, we usually deal with the SHG photon counts <10000/sec. Each photon indicates a voltage pulse of height around 1V with 12ns temporal width. Each pulse is profiled by one or two samples of ATS9440 with sampling gap of 8ns, at 125MHz sampling rate. As a result, within 1 second time window, we obtained about 10000 meaningful data points out of 125M samples. After billions of times of averaging, the SHG photons signals will be diluted by $10000/125,000,000 \approx 10^{-4}$ after averaging due to the low counts of SHG photons. For the most part ($> 99.99\%$) of data acquisition time, each time sampling point can not see any SHG photon pulse, and only measures the background noise. Therefore, minimizing the background noise is crucial for increasing the signal-to-noise ratio. Unfortunately, some unclear intrinsic design flaw on ATS9440 result the unpredictable systematic error for background measurement under DMA mode. This systematic error is on par with the diluted SHG pulse signal, and greatly distorts the averaged SHG intensity profile. In order to circumvent this problem, I added in the DC signal to shift the background from zero to the outside of the ATS9440 measurement range. For example, if digitizer is set of the range in -0.4∼0.4V, the DC signal is selected to be 0.405V in order to persistently saturate the digitizer by 5mV. In this way, the digitizer will produce a perfect 0.4V constant background signal. When a negative SHG photon pulse of height 0.7V appears, it briefly kicks off the digitizer from the saturation status, and produce a sharp negative pulse. The catch for this configuration is that the response time of saturated digitizer will be theoretically prolonged. But, fortunately, I did not notice any delay influencing the measurement in time domain.

Another benefit of this saturation technique is truncating the undesired jitter following the SHG signal. The pulses saw by ATS9440 are not ideal due to the capacitance of the transportation

Figure 5.1: (a) Normal condition: the digitizer range covers the full range of the SHG photon pulses. Left is the actual SHG photon pulses being profiled at 8ns interval sampling without saturating the digitizer. Right is the sample array obtained by digitizer. The red markers are the actual sampling values by digitizer at 125MS/s sampling rate. The jitter tail is also profiled and hence introduces noise. (b) Saturation condition: the SHG photon pulses is shifted by a DC signal which saturates the dizzier range. Left is the actual SHG photon pulses profiled by the digitizer. Right is the sample array obtained by digitizer. The jitter tail is truncated by the saturation level.

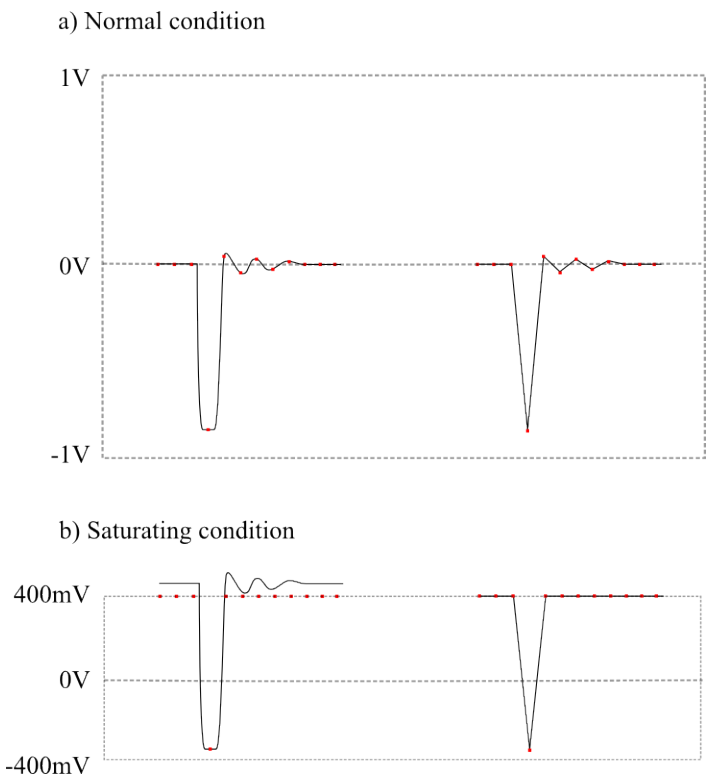

Figure 5.2: The flow chart for SHG photon processing. The lower part of the graph is the circuit diagram for shifting the current pulse.

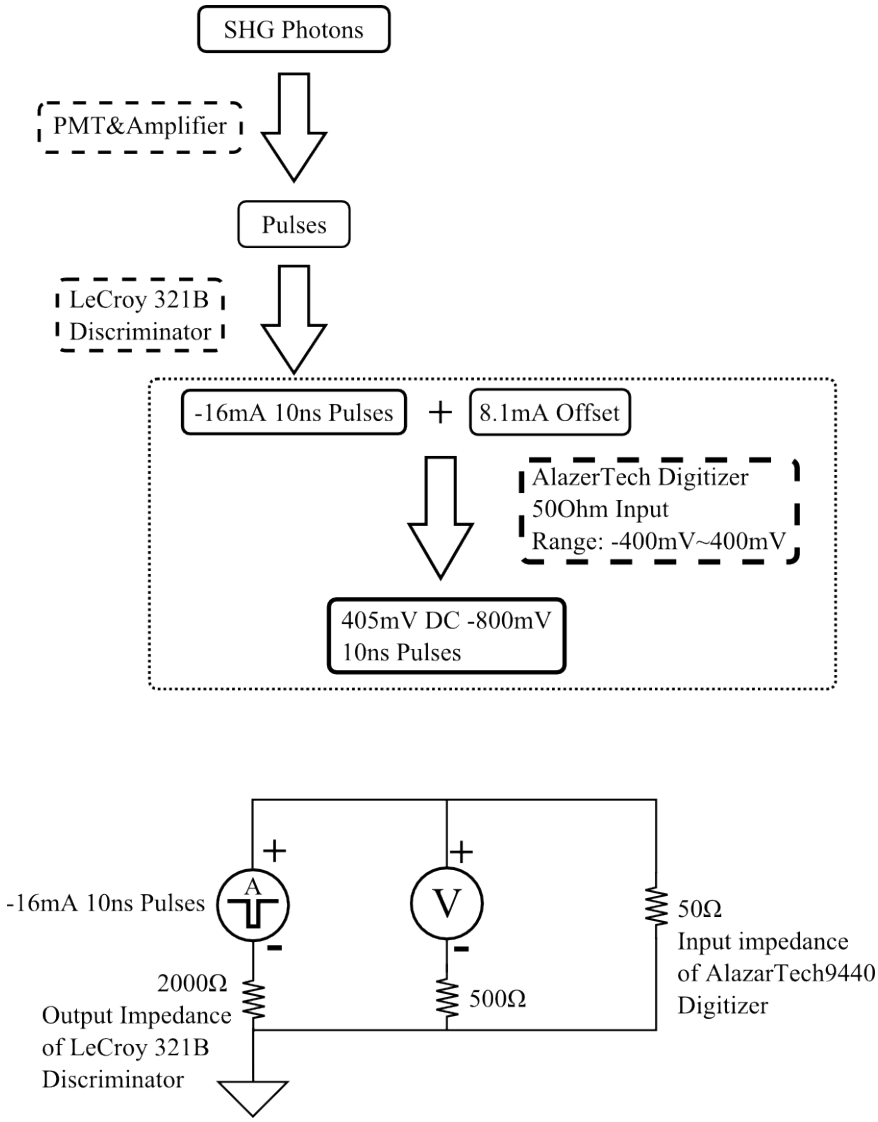

cable and connectors. The jitter following the pulse introduce extra noise for the averaged SHG signal and jeopardize the temporal resolution. By tuning the saturation level of the digitizer, DC offset and pulse height, the jitter can be truncated by the saturation.(Figure 5.1)

Figure 5.2 shows the SHG photon pulse processing flow chart. It is necessary to produce the pulses of required standard for best temporal resolution and signal-to-noise ratio. The LeCroy 321B discriminator is capable of producing the negative current of 16mA with a tunable temporal width set to 10ns. I also developed the circuit shown in Figure 5.2 to shift the current pulse. The LeCory 321B discriminator output is negative current source with >2000Ω output impedance. It parallels with a voltage source of 500Ω output impedance and the 50Ω. The voltage source provide a consistent current flow through the digitizer. When 16mA current pulse is triggered by SHG photon, it would flow through the digitizer providing about 800mV voltage pulse on ATS9440 with 10% current leakage through the voltage source. This configuration is superior to the typical amplifier DC offset circuit by avoiding pulse shape distortion.

5.2 SSHG dynamics under sinusoidal voltage wave on tri-layer sample

Following the standard C-V measurement procedure, a strong negative DC bias is applied to accumulate the majority carriers in the a-Si:H near the top interface. The current response and SHG photons counts are monitored in the time domain. The sinusoidal current wave is observed as a result of the voltage function. For each particular frequency of the AC voltage, one can obtain the magnitude and phase of the complex device impedance, and eventually produce the Bode plot over a large frequency range as shown in Figure 5.5. The impedance Bode plot indicates that, in the low frequency range ($< 10^3$Hz), the device display high impedance which is dominated by the a-Si:H bulk resistance. As the driving frequency increases, the impedance of device geometrical capacitance decreases and allows more AC current flowing through the device. When the frequency reach 1MHz, the total impedance of the whole device is limited by the ITO series resistance.

A circuit model is established to quantitatively analyze the complex impedance Bode plot. In this model, different electronic elements correspond to different parts of the sample (Figure 5.4).

Figure 5.3: The panel (a) shows the measured SHG intensity versus the applied bias on the sample. The red circles are the SHG data, the blue line is the fitted curve based on the interference of the idler SHG and the EFISH contribution. This fitting result yields a 84 deg phase difference, allowing the SHG in the reverse bias region can be approximated by $SHG = V_A * F_V^{SHG} + SHG_{Offset}$. In lower panel, we show the -3 V DC biased 0.5Vpp voltage sinusoidal wave in (b), the resulting current sinusoidal wave in (c), the real time SHG data and sinusoidal fitting curve in (d).

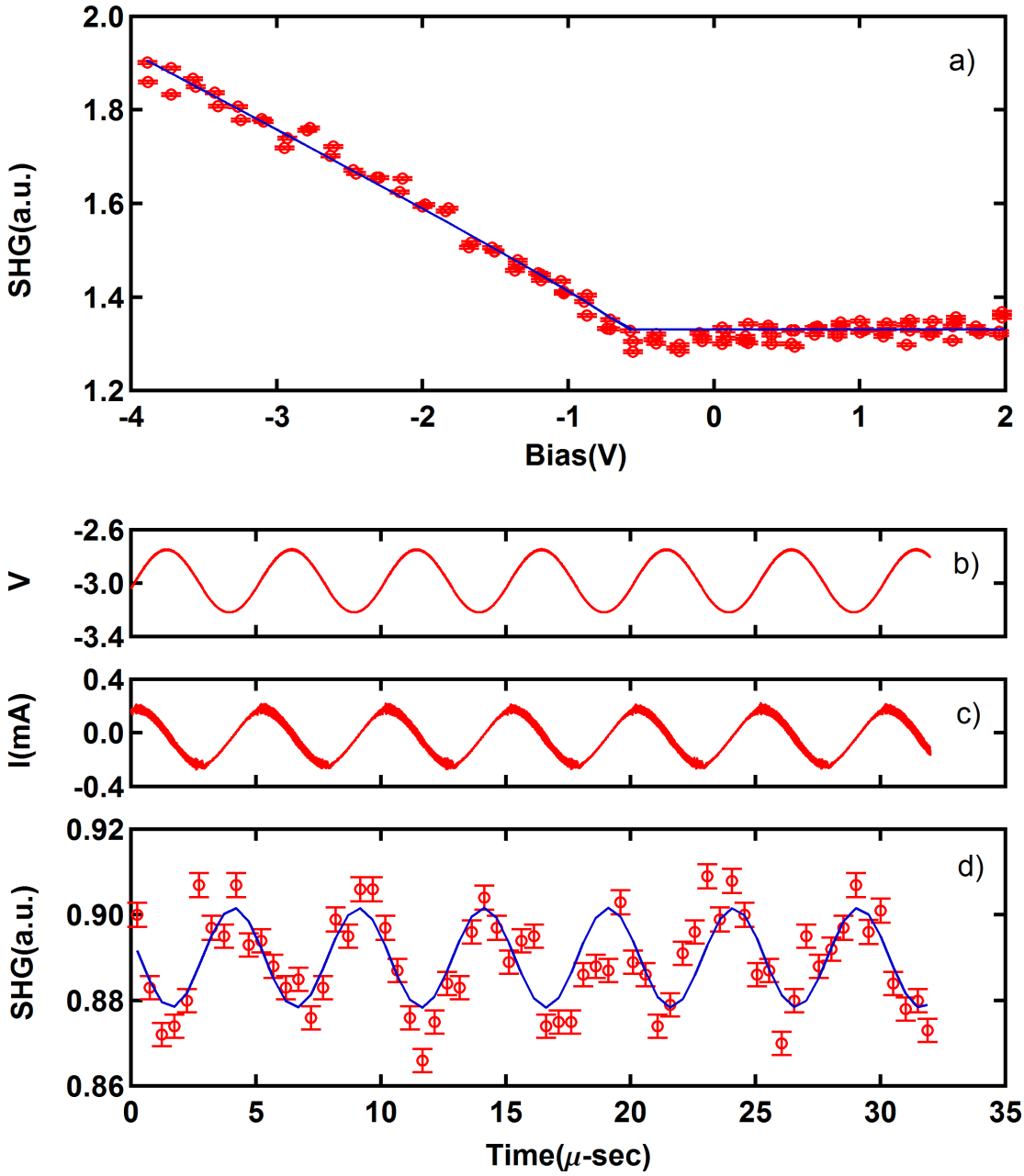

R_0 is the ITO and the electrode/ITO contact resistance. R_1 is the resistance of bulk amorphous silicon. C_1 is the geometrical capacitance due to the device architecture. Here we assume that, C_2 is the capacitance of the depletion region while R_2 is the resistor hindering the carrier movement in the depletion region, and this R_C pair together models the carrier dynamics in the depletion region of ITO/a-Si:H interface. Based on this circuit model, the device impedance can be fully described and fitted by Eq(1), yielding the component values of R_0, R_1, R_2, C_1 and C_2. The fitting result indicates that the device impedance characteristic is primarily governed by the R_0, R_1 and C_1, while R_2 and C_2 pair contributes a small amount charge flow of the total current signal. However, successful fitting to the impedance Bode plot does not necessarily prove our assumption for the origination and physical location of R_2 and C_2. However, time-resolved SHG provided further evidence to validate this hypothesis.

Figure 5.4: Shows the device structure of the sample, bias geometry, and optical experimental configuration. The circuit elements in the dash line rectangle make up the circuit model resembling the actual device.

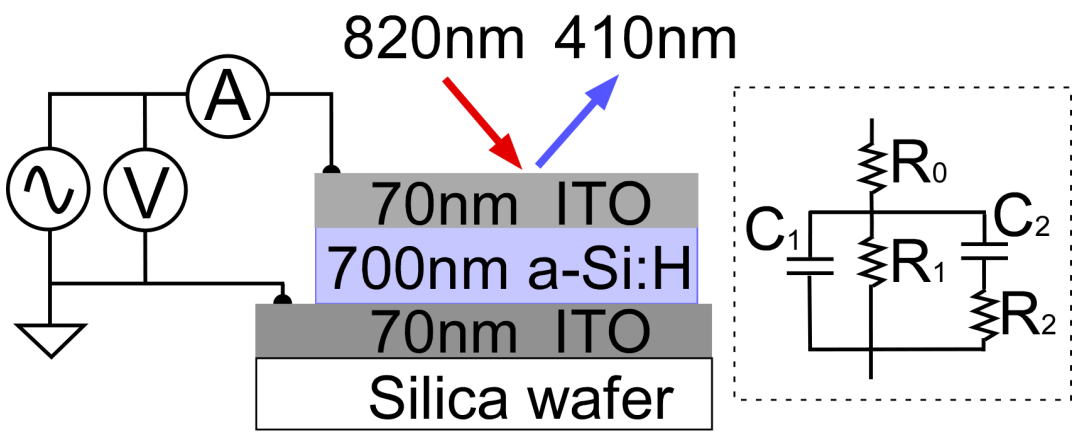

$$\tilde{Z}(\omega) = \frac{\tilde{V}_A(\omega)}{\tilde{I}(\omega)} = Z_{R0} + Z_{aSi} \quad with \quad Z_{aSi} = \frac{1}{1/Z_{R1} + 1/Z_{C1}(\omega) + 1/(Z_{C2}(\omega) + Z_{R2})} \tag{5.1}$$

$$\frac{\tilde{V}_{C2}(\omega)}{\tilde{V}_A(\omega)} = \frac{Z_{aSi}}{Z_{aSi} + Z_{R0}} * \frac{Z_{C2}(\omega)}{Z_{C2}(\omega) + Z_{R2}} \tag{5.2}$$

$$SHG(t) = V_{C2}(t) * F_V^{SHG} + SHG_{Offset} \qquad \Rightarrow \qquad \frac{S\tilde{H}G(\omega)}{\tilde{V}_A(\omega)} = \frac{\tilde{V}_{C2}(\omega)}{\tilde{V}_A(\omega)} * F_V^{SHG} \tag{5.3}$$

The SHG intensity can reveal the voltage drop across the top ITO/a-Si:H junction, hence, the time-resolved SHG data can be converted into the real-time voltage on C_2, aka V_{C2}, via the linear relationship described in Equation (5.3). In Figure 5.3(b) panel, 50 kHz 0.5 Vpp sinusoidal voltage function and -3V DC offset are imposed on the sample. We observed a sinusoidal SHG signal in the time domain (Figure 5.3(d) panel) indicating V_{C2} behaves as sinusoidal wave. The SHG wave is fitted with sinusoidal function, allowing one to obtain the magnitude ratio and relative phase between SHG oscillation and applied voltage function. By comparing the SHG oscillation magnitude and relative phase to the input voltage function over wide frequency range, we plot the SHG Bode plot as showed in Figure 5.5(b) panel. In this figure, starting from 200 kHz, the SHG oscillation magnitude attenuates rapidly, and the relative phase deviates from 0. These SHG behaviors corresponding to the carriers in the depletion region being unable to respond fast enough to the changes in the applied bias.

From the equivalent circuit model, we draw the fitting functions 5.1 and 5.2. Z_X represents the impedance of component "X". The impedance of capacitor, $Z_C(\omega)$ is frequency dependent. Accent of "$\sim$" represents the complex vector of the sinusoidal oscillation signal. We draw 5.3 from the linear relationship between the SHG and the voltage drop on C_2 capacitor. F_V^{SHG} is the conversion factor between SHG intensity and the static voltage drop on the depletion region. The additional information of V_{C2} provided by SHG Bode plot, in conjunction with the impedance Bode plot, are adequate to determine each circuit element in the model, especially, the accurate value of C_2 capacitor, i.e. capacitance of the depletion region.

The solid lines in Figure 5.5 are the fit results to the Equations (5.1) to (5.3). We assume that measurement error is dominated by shot-noise, as indicated by the error bars. Fit quality is excellent with $\chi^2 < 3$, and fitted curves clearly capture current and SHG data in the fitted frequency range. The extracted circuit element values are summarized in Table 5.1. The successful

Figure 5.5: Panel (a) shows the bode plot of the device impedance. Panel (b) shows the ratio of fitted SHG AC amplitude over driving voltage AC amplitude versus frequency, and the relative phase between fitted SHG signal and voltage AC signal at different frequency. The solid lines in the graphs are the fitting curve from the model described in Equations (5.1) to (5.3).

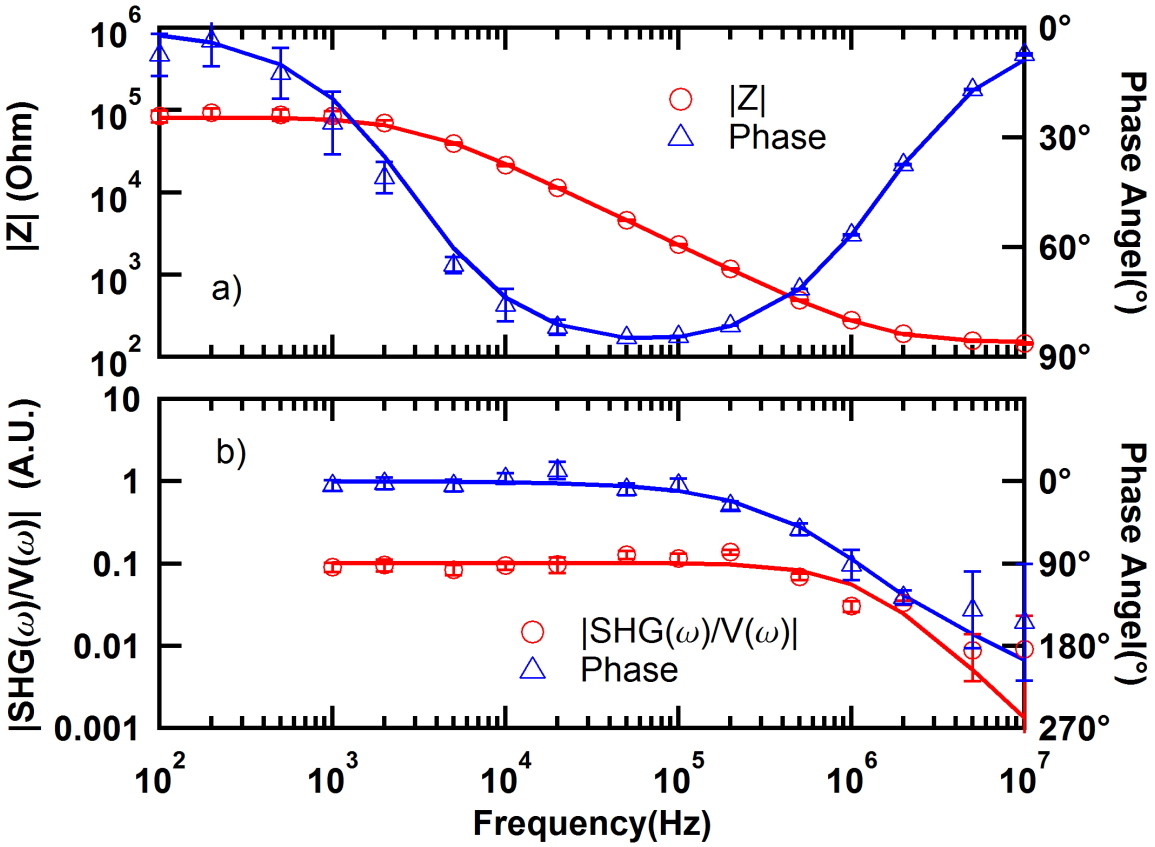

fit to the SHG data shows that the dynamics of the trapped carrier can be modeled as RC circuit over a large frequency range, where the resistor mimics the carrier trapping effect in the depletion region.

5.3 SSHG dynamics under square voltage wave on tri-layer sample

In order to study the transient behavior of the electric field in a-Si:H/ITO junction, we apply the 2 Vpp 50 kHz square wave and -2 V DC offset on the same device, and monitor the current and SHG simultaneously by the same experimental setup. The results are shown in Figure 5.6. Because the square wave function provided by the voltage source are non-ideal(Figure 5.3), the theoretical electrical response of the circuit model for step function is not sufficient. Therefore, we developed the algorithm of solving coupled differential equations convolving with the voltage data, to yield the numerical solutions of current through the device and voltage drop on capacitor C_2 which can be translated into SHG data. The coupled differential equations derived from the circuit model are shown below as Equations (5.5) and (5.6). In the equations below, "i_X" and "V_X" represents the current and voltage drop across the component "X", and "F_V^{SHG}" and "SHG_{Offset}" are the parameters for linear relationship between SHG and V_{C2}. By simultaneously approaching the numerical solutions ($i_0(t)$ and $SHG(t)$ in 5.6) of differential equations to the measured waves of current and SHG (Figure 5.3(b) and (c)), the algorithm is capable of finding the best fit of circuit component values.

$$\frac{di_{R1}(t)}{dt} = \frac{1}{C_1 R_0 R_1}(V_A(t) - i_1(R_0 + R_1) - C_2 R_0 \frac{dV_{C2}}{dt}) \tag{5.4}$$

$$\frac{dV_{C2}(t)}{dt} = \frac{i_{R1}(t) R_1}{C_2 R_2} - \frac{V_{C2}(t)}{C_2 R_2} \tag{5.5}$$

$$i_0(t) = \frac{V_A(t) - i_{R1}(t) R_1}{R_0} \qquad and \qquad SHG(t) = V_{C2}(t) * F_V^{SHG} + SHG_{Offset} \tag{5.6}$$

In Figure 5.6(b) the dash line marked region, the current curve shows sharp spikes within

1 us after the voltage transitions in both polarities, and they are symmetrically identical in both polarity. Those current spikes are zoomed in as showed in Figure 5.6(f) and (e). The fitting curves catch all the minute details in the current wave, especially the transition region in the zoomed region. In Figure 5.6(c), SHG transient signals are also fully caught by the fitting curve. The successful fit to the current data confirmed that the device electric response is can be explained by the circuit model consisting of linear electric components.

We compared the fitted circuit component values both from the sinusoidal function and square function response in Table 5.1. Their agreement confirms the success of the circuit model on explaining the ITO/a-Si:H interface charge transportation over a wide range of frequency. The product of R_2 and C_2 values indicates that the junction depletion region has a RC time constant around 2 microseconds. We also notice that the forward biased ITO/a-Si:H interface on the device rear side does not contribute to the electric response of the whole device. This could be due to the depletion region is squeezed by the forward bias, in which the trapped charge carrier is frozen or fully eliminated. Further, the SHG clearly indicates that the slow RC time that is visible in the device current response is happening at the ITO/a-Si interface.

5.4 Summary

We have developed a new technique to combine current-voltage and SHG measurement allowing us to directly study charge motion at the ITO/a-Si:H interface. The innovative experimental method for SHG dynamics using high speed digitizer is detailed. The current and SHG measurement for trilayer structure under sinusoidal and square voltage wave is discussed. A circuit model is introduced to explain these data. In order to extract the component parameters based on this circuit model, multivariate fitting functions are developed for understanding complex impedance and SHG over a large range of frequency, and time-evolving fitting functions are developed to integrate the transient current and SHG signal. The plausible agreement between these two different analytical methods shows the success of the circuit model on explaining the ITO/a-Si:H interface charge transportation over a wide range of frequency. It further indicates that the slow RC time

Figure 5.6: (a) The voltage square wave function applied on the device; (b) The measured current through the device(Red) and its fitting curve(Blue); (c) the measured SHG intensity data (Red) and its fitting curve (Blue); (d) the corresponding fitting residual for SHG data. The zoom in current curves (f) and (e) as the dash line marked region in (b).

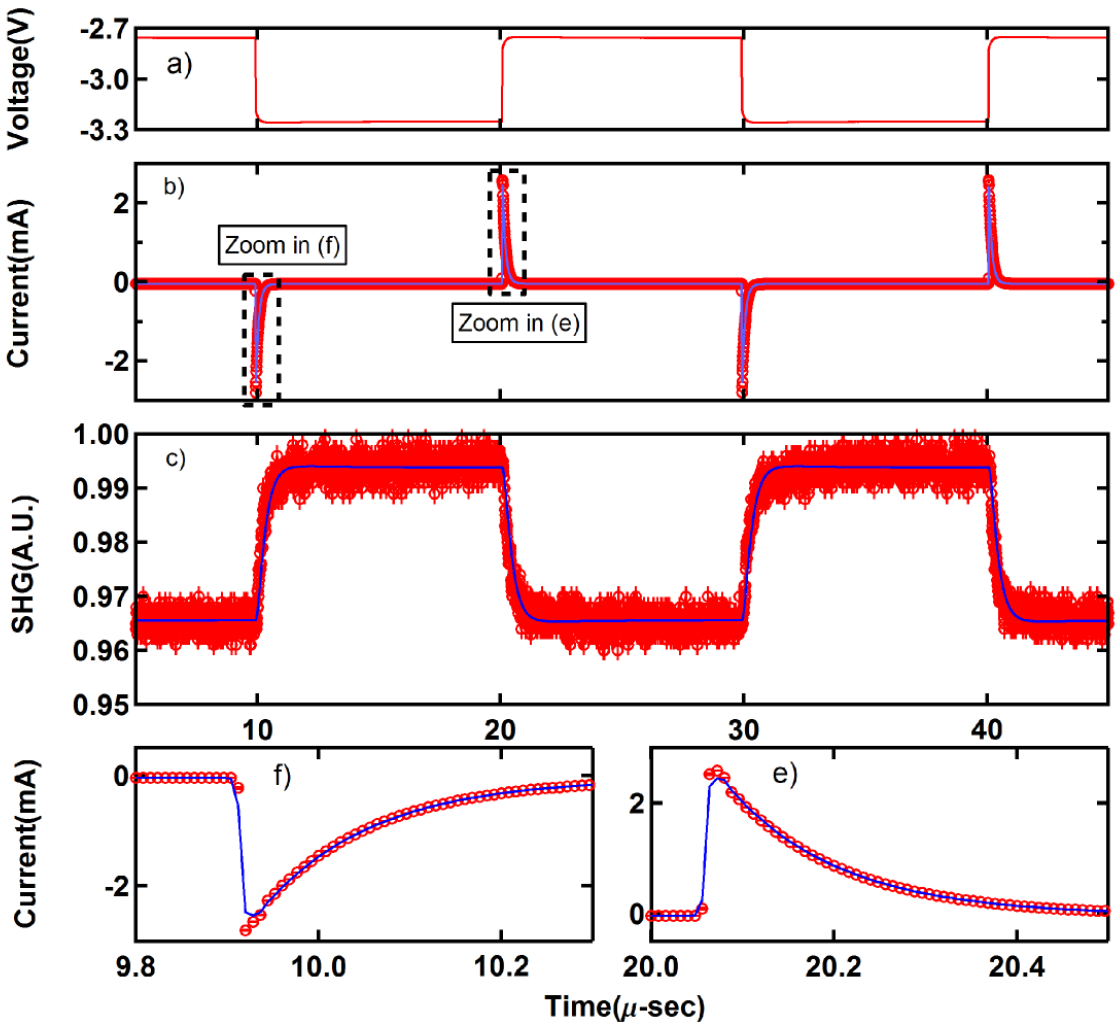

Table 5.1: Resulting fit parameters from least squares fitting of the current and SHG data, respectively, using Equations (5.1) to (5.3) for sinusoidal wave response in Figure 5.3, and using Equations (5.4) to (5.6) for square wave response in Figure 5.6. The plausible agreement between the two sets of fitted parameter shows the success of the circuit model on explaining the ITO/a-Si:H interface charge transportation over a wide range of frequency.

Parameter	Sinusoidal Wave Response	Square Wave Response
R_0(Ohm)	149.90 $\pm$1.07	155.581 $\pm$0.018
R_1(Ohm)	80583.8 $\pm$2376.16	87839.5 $\pm$74.4
R_2(Ohm)	23653.0 $\pm$6642.8	37457.9 $\pm$334.4
C_1(pF)	688.8 $\pm$4.9	661.47 $\pm$0.04
C_2(pF)	7.70 $\pm$2.09	7.987 $\pm$0.034
F_V^{SHG}*(a.u.)* SHG to V_{C2} Factor	0.0565 $\pm$2.3e-03	0.0570 $\pm$1e-04

that is visible in the device current response is happening at the ITO/a-Si interface.

Chapter 6

Summary and Proposed Next Experiments

6.1 Summary for SHG from SHJ solar cell

Now we can summarize the information presented in Chapter 3 and 4, and look back at the data on SiHJ solar cell again. In Chapter 3, the input polarization on SHJ solar cell at Open Circuit and Short Circuit condition (Figure 3.6) indicates the major bias-dependent SHG signal happens at pP geometry. The possible candidates for this SHG change are SSHG from ITO/a-Si:H and a-Si:H/c-Si interface, SHG from c-Si bulk and EFISH from a-Si:H film. Further careful study on the azimuthal scan for pP SHG at Open Circuit and Short Circuit conditions (Figure 3.9) excludes the responsibility of c-Si bulk for producing bias-dependent signal, by isolating the bias-independent four fold SHG contribution. Next, the device simulation for electric field profile in the SiHJ junction shows significant electric field strength change in the a-Si:H layer. It leads our attention to suspect the EFISH contribution from a-Si:H. What is more, the opposite SHG behaviors in the "twin" reverse doped SiHJ further suggest that the strong bias-dependent SHG signals is originated from the reversed electric fields of the a-Si layer in these devices. In Chapter 4, we have demonstrated the strong EFISH signal from a-Si:H bulk, and develop the interference theory to qualitatively explain the bias-sweep SHG signal and input polarization scan data. Our fitting results indicate a strong bias-sensitive pP SHG signal from EFISH effect in a-Si:H. The similar fitting results were further proven to be valid for the redesigned HIT device with a thick a-Si:H layer. This result further support our hypothesis that the bias-dependent SHG in SiHJ solar cell arises from EFISH effect in super thin a-Si:H layer.

6.2 Suggestion for future experiments for SHJ solar cell

In Chapter 4, the quantitative model has been established for EFISH effect in a-Si:H, and the future experiment can be focused on probing the electric field in a-Si:H layer for SiHJ solar cell. The low-hanging fruit is theoretically reconstructing "EFISH vs Bias" signal originated from thin a-Si:H layer in SiHJ solar cell. One can simulate the electric field in this layer for SiHJ solar cell device under different bias condition. Based on the quantitative model developed in Chapter 4, the EFISH signals from a-Si:H layer can be predicted for the electric field simulation results of different bias. Next, the similar interference theory as presented in Chapter 4 can be implemented to "SHG vs Bias" signal, in order to separate the bias-dependent EFISH and bias-independent SHG contributions. The bias-independent SHG contribution consists of the isotropic SSHG originated from air/ITO and ITO/a-Si:H interface, anisotropic SHG from a-Si:H/c-Si interface and c-Si bulk. The anisotropic SHG contribution can be further distinguished by azimuthal scan. Finally, if the suggested experiments succeed, we shall develop a comprehensive fitting function to explain the SHG signal from SiHJ solar cell as a function of different biases and azimuthal angles. As a result, the EFISH from a-Si:H thin layer, isotropic SSHG from air/ITO and ITO/a-Si:H interface, anisotropic SHG from a-Si:H/c-Si and c-Si bulk will be quantitatively separated.

Separating EFISH from the total SHG signal will allow directly probing the electric field profile presenting in the a-Si:H layer. EFISH will be useful to the electric field dynamics of SiHJ device under various condition, including the temperature sweep, different doping levels. It is capable of providing critical information of charge transportation in the working SiHJ device under illumination. Also, one may want to tune the probing laser wavelength from 820 nm to deep infrared region to avoid exciting the large amount of electron-hole pairs which may drastically alter the device physics.

6.3 SHG dynamics on ITO/a-Si:H junction

In Chapter 5, we directly probe carrier dynamics in the depletion region of a ITO/a-Si:H junction with time-resolved optical second-harmonic generation. This SHG technique in conjunction with traditional C-V measurement successfully confirms that the capacitance of trapped charge locates in the ITO/a-Si:H depletion region around the top surface under the reverse bias region. It successfully characterized the electrical response of ITO/a-Si:H junction over a wide frequency range from 100Hz to 10MHz. SHG is demonstrated as powerful tool to study the electric field dynamics for ITO/a-Si:H interface.

Because the data in traditional C-V measurement is overwhelmed with the DC current flowing through the device, accurate interpretation of the current signals requires careful separation of the capacitance contributions of the depletion region, bulk states, free carriers and rear interface in the semiconductor device. EFISH is capable of providing critical real-time electric-field information for understanding traditional capacitance measurement in complicated device structure. By fitting the current-frequency and EFISH-frequency data simultaneously to the device circuit model, we successfully separate the capacitance of a-Si:H/ITO junction from the device bulk capacitance. In the future, the attention can be paid to the study of capacitance variation when changing bias, temperature, illumination conditions etc. For example, the experiment of "capacitance vs bias" would allow the further ability to investigate the state diversity profile. Also, this approach could be applied to study the complex multilayer a-Si:H devices, such as Si heterojunction solar cells.

6.4 SHG on Organic Photovoltaic (OPV)

Organic Photovoltaic (OPV) are third generation PV cells which use an organic polymer layer instead of inorganic semiconductor material for light absorption and charge transport to produce electricity from sunlight by the photovoltaic effect. People are interested in OPV mainly because its potential for low cost manufacturing and the tunability of the band gaps. We are lucky enough to obtain several OPV devices from NREL David Ginley's group, and measured them using our

SHG experimental setup. Interesting SHG signal is observed in input polarization scan at different bias. I would like to present those initial results here, and hopefully they may inspire the following SHG research on OPV in the future. Due to my shallow knowledge on OPV itself, I will merely present the device structure and SHG results, without going into depth for OPV physics. In the following part, I will brief the observed preliminary SHG result.

The most common strategy for OPV is so-called bulk heterojunction, in which electron donors such as poly(3-hexylthiophene) (P3HT) and acceptors such as (6,6)-phenyl C61 butyric acid methyl ester (PCBM) are blended to form one mixed layer. The OPV devices we obtained from NREL is built based on P3HT:PCBM blended polymer film. The device structure and SHG experimental configuration is indicated in Figure 6.1. Due to the instable nature of the organic molecule, the polymer layer would experience "bleaching" effect, with the color is washed out under the exposure of light and air. I start the SHG measurement from a lower input laser intensity 140 mW on a fresh device. The OPV polymer layer displays significant decaying SHG signal during the standard input polarization scan. In Figure 6.2, by comparing the SHG intensity at p states, i.e. 0°, 180°, 360°, 540° and 720°, the pP SHG field strength experience obvious decay over the time (about 2 hours). This can be caused by the instable property of the polymer layer under pulse laser.

When the device is entirely bleached out, we re-take the input polarization scan at different bias condition. The data is presented in Figure 6.3 for -0.5, 0 and 0.5 V. We notice that the SHG signals in all geometries are all amplified in the positive bias condition. The further measurement of SHG vs bias further reveals the SHG behavior under the bias sweeping. In Figure 6.4, SHG signals in pP, sP, $mixP$ and $mixS$ shows similar asymmetric growth as in a-Si:H tri-layer device. In the negative bias region, the SHG intensity is slightly decreased and the phase between $mixS$ and $mixP$ drifts across zero. The current curve displays a diode behavior, rectifying the positive bias region. More interesting part is that the SHG signal is greatly amplified in the positive bias region, with relative phase between $mixS$ and $mixP$ very stable. These bias-dependent signals may be dominated the EFSIH and can be used to imply the electric field profile in this complicated OPV device.

Figure 6.1: shows the device structure of OPV, bias geometry, and optical experimental configuration.

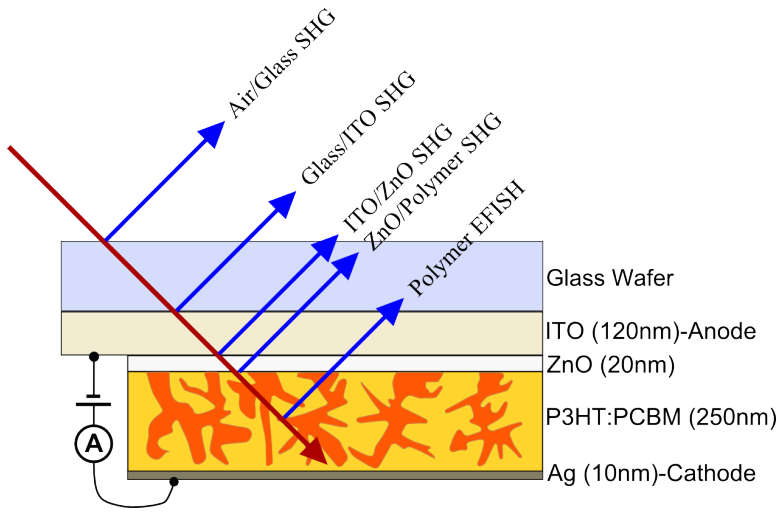

Figure 6.2: Input polarization scan under 140mW input laser on OPV device. The input laser polarization is rotated in an uniform speed from 0°(p state) to 720°. Therefore, the bottom axis also represents the elapsed time. By comparing the SHG intensity at p states, i.e. 0°, 180°, 360°, 540° and 720°, the pP SHG field strength experience decay over the time. This can be caused by the instable property of the polymer layer under pulse laser.

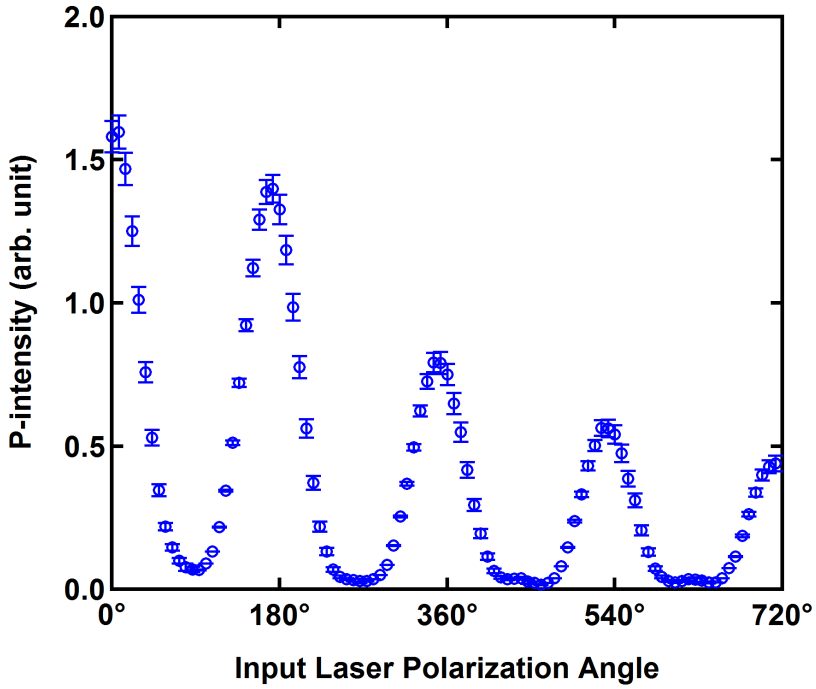

For the future experiment, I suggest we try to exercise the interference theory developed in Chapter 4 to separate the EFISH and interface SHG contribution. The EFISH signals are useful for implication of electric field profile within the device. Then after, the SHG dynamics measurement can be used to study the interfacial exciton dynamics.

Figure 6.3: Measured second harmonic intensity and relative phase for OPV as a function of input laser polarization at three different device voltage biases -0.5,0 and 0.5 V. In upper panel, we plot the p-polarized SHG intensity. In mid panel, we plot the s-polarized SHG intensity. In bottom panel, we plot relative phase of the p and s polarized SHG.

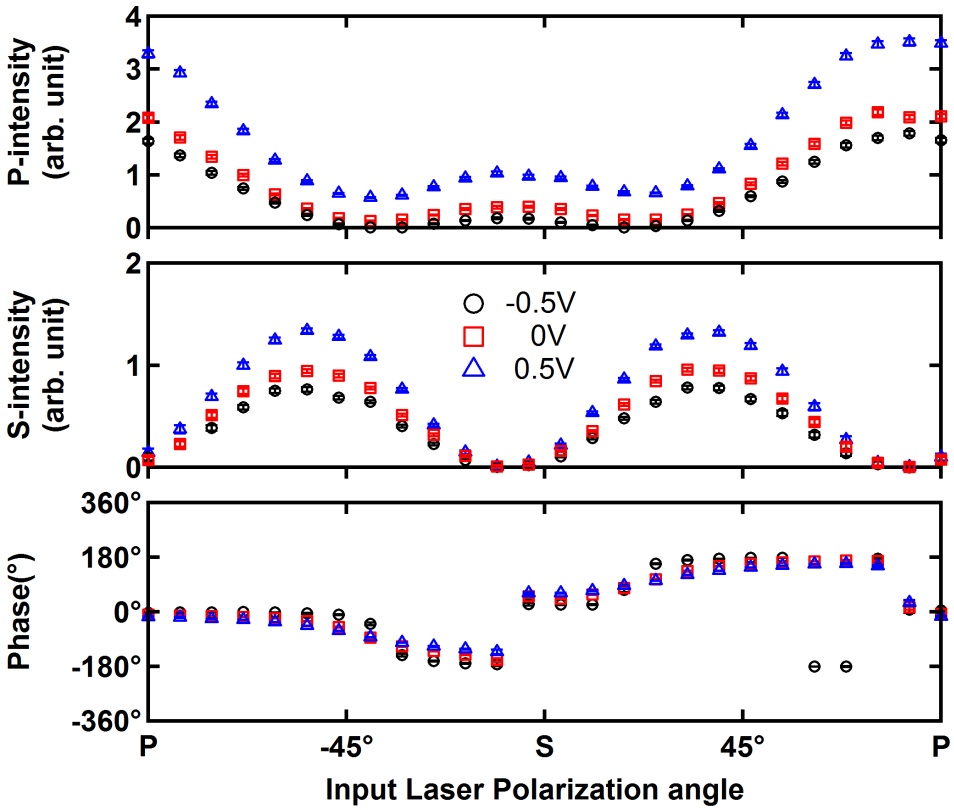

Figure 6.4: Second harmonic intensity in upper panel, relative phase in mid panel, and current in bottom panel as a function of applied bias voltage for OPV device. In upper panel, the SHG intensity is shown for different input laser polarizations: red circles: pP, blue squares: sP, green point-up triangles: $mixP$, black point-down triangles: $mixS$. Mid panel shows the phase difference between the mixP and mixS SHG signal. Bottom panel shows the I-V curves.

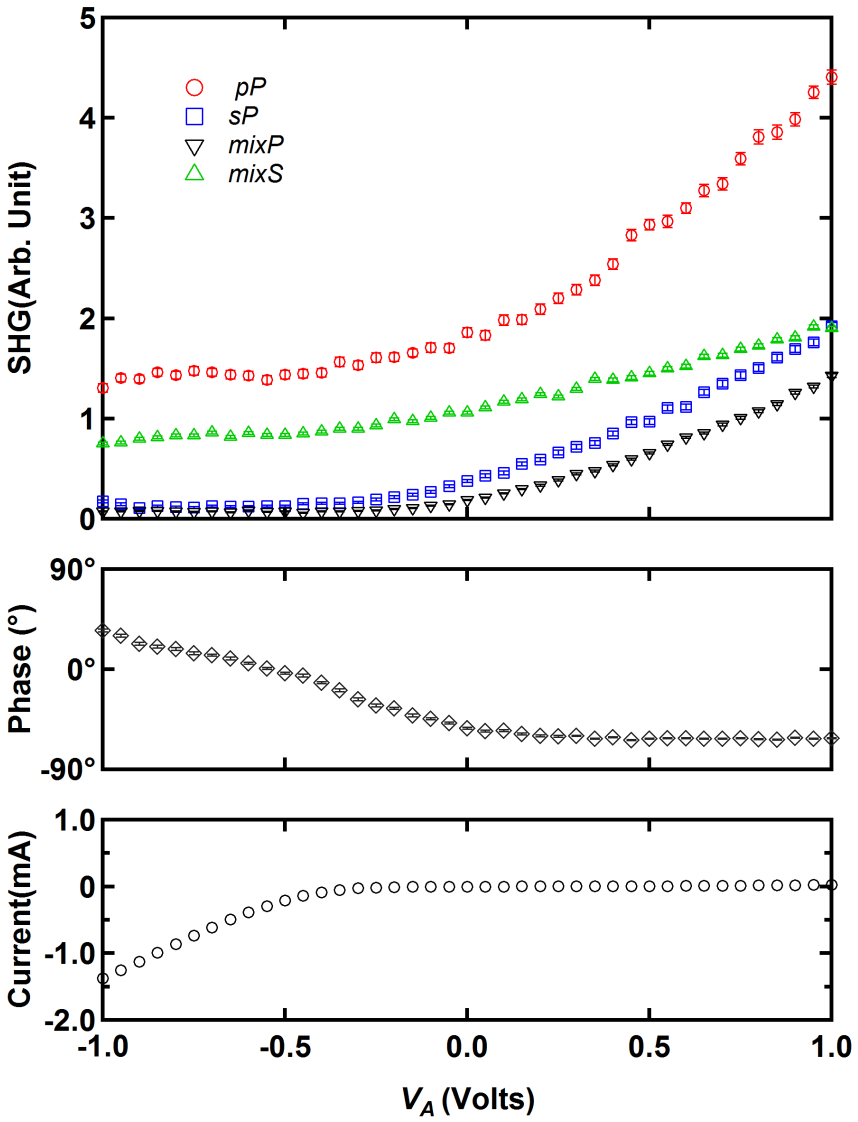

Bibliography

[1] R. Williams, "Becquerel Photovoltaic Effect in Binary Compounds," The Journal of Chemical Physics, vol. 32, no. 5, p. 1505, 1960.

[2] A. E. Becquerel, "Mémoire sur les effets électriques produits sous linfluence des rayons solaires.," Comptes Rendus, no. 9, pp. 561–567, 1839.

[3] Author:unknown, "Solar Cell," Wikipedia: http://en.wikipedia.org/wiki/Solar_cell.

[4] TheNoise, "PN junction," Wikipedia: http://en.wikipedia.org/wiki/Pn_junction.

[5] W. D. Eades and R. M. Swanson, "Calculation of surface generation and recombination velocities at the Si-SiO2 interface," Journal of Applied Physics, vol. 58, no. 11, p. 4267, 1985.

[6] S. De Wolf, A. Descoeudres, Z. C. Holman, and C. Ballif, "High-efficiency Silicon Heterojunction Solar Cells: A Review," Green, vol. 2, pp. 7–24, Jan. 2012.

[7] S. M. Iftiquar, Y. Lee, V. A. Dao, S. Kim, and J. Yi, "High efficiency heterojunction with intrinsic thin layer solar cell : A short review," in Materials and processes for energy: communicating current research and technological developments (A. Mendez-Vilas, ed.), pp. 59–67, Formatex Research Center, 2013.

[8] W. Fuhs, K. Niemann, and J. Stuke, "Heterojunctions of Amorphous Silicon and Silicon Single Crystals," in TETRAHEDRALLY BONDED AMORPHOUS SEMICONDUCTORS: International Conference, pp. 345–350, ASCE, 1974.

[9] K. Wakisaka, M. Taguchi, T. Sawada, M. Tanaka, T. Matsuyama, T. Matsuoka, S. Tsuda, S. Nakano, Y. Kishi, and Y. Kuwano, "More than 16% solar cells with a new 'HIT' (doped a-Si/nondoped a-Si/crystalline Si) structure," in The Conference Record of the Twenty-Second IEEE Photovoltaic Specialists Conference - 1991, pp. 887–892, IEEE, 1991.

[10] M. Tanaka, M. Taguchi, T. Matsuyama, T. Sawada, S. Tsuda, S. Nakano, H. Hanafusa, and Y. Kuwano, "Development of New a-Si/c-Si Heterojunction Solar Cells: ACJ-HIT (Artificially Constructed Junction-Heterojunction with Intrinsic Thin-Layer)," Japanese Journal of Applied Physics, vol. 31, pp. 3518–3522, Nov. 1992.

[11] T. F. Schulze, L. Korte, F. Ruske, and B. Rech, "Band lineup in amorphous/crystalline silicon heterojunctions and the impact of hydrogen microstructure and topological disorder," Physical Review B, vol. 83, p. 165314, Apr. 2011.

[12] S. De Wolf and M. Kondo, "Abruptness of a-Si:Hc-Si interface revealed by carrier lifetime measurements," Applied Physics Letters, vol. 90, no. 4, p. 042111, 2007.

[13] T. Koida, H. Fujiwara, and M. Kondo, "Reduction of Optical Loss in Hydrogenated Amorphous Silicon/Crystalline Silicon Heterojunction Solar Cells by High-Mobility Hydrogen-Doped In 2 O 3 Transparent Conductive Oxide," Applied Physics Express, vol. 1, p. 041501, Mar. 2008.

[14] W. Ho, Y.-Y. Chen, T.-H. Cheng, J.-Y. Chen, J.-A. Lu, P.-L. Huang, and C. W. Liu, "Thermal oxide, Al¡inf¿2¡/inf¿O¡inf¿3¡/inf¿ and amorphous-Si passivation layers on silicon," in 2010 35th IEEE Photovoltaic Specialists Conference, pp. 003163–003166, IEEE, June 2010.

[15] J.-W. A. Schuttauf, K. H. M. van der Werf, I. M. Kielen, W. G. J. H. M. van Sark, J. K. Rath, and R. E. I. Schropp, "High quality crystalline silicon surface passivation by combined intrinsic and n-type hydrogenated amorphous silicon," Applied Physics Letters, vol. 99, no. 20, p. 203503, 2011.

[16] P. Würfel, Physics of Solar Cells: From Principles to New Concepts. Weinheim, Germany: Wiley-VCH Verlag GmbH, 2005.

[17] M. Taguchi, A. Yano, S. Tohoda, K. Matsuyama, Y. Nakamura, T. Nishiwaki, K. Fujita, and E. Maruyama, "24.7% Record Efficiency HIT Solar Cell on Thin Silicon Wafer," IEEE Journal of Photovoltaics, vol. 4, pp. 96–99, Jan. 2014.

[18] Panasonic, "HIT VBHN235SJ17 PV module specification," tech. rep., 2012.

[19] P. Franken, A. Hill, C. Peters, and G. Weinreich, "Generation of Optical Harmonics," Physical Review Letters, vol. 7, pp. 118–119, Aug. 1961.

[20] F. Brown and R. Parks, "Magnetic-Dipole Contribution to Optical Harmonics in Silver," Physical Review Letters, vol. 16, pp. 507–509, Mar. 1966.

[21] N. Bloembergen and Y. Shen, "Optical Nonlinearities of a Plasma," Physical Review, vol. 141, pp. 298–305, Jan. 1966.

[22] T. Heinz, C. Chen, D. Ricard, and Y. Shen, "Spectroscopy of Molecular Monolayers by Resonant Second-Harmonic Generation," Physical Review Letters, vol. 48, pp. 478–481, Feb. 1982.

[23] Y. R. Shen, "Optical Second Harmonic Generation at Interfaces," Annual Review of Physical Chemistry, vol. 40, pp. 327–350, Oct. 1989.

[24] Y. R. Shen, "Surface properties probed by second-harmonic and sum-frequency generation," Nature, vol. 337, pp. 519–525, Feb. 1989.

[25] G. Richmond, J. Robinson, and V. Shannon, "Second harmonic generation studies of interfacial structure and dynamics," Progress in Surface Science, vol. 28, pp. 1–70, Jan. 1988.

[26] Y.-R. Shen, The Principles of Nonlinear Optics. New York: Wiley-Interscience, 1 ed., 1984.

[27] T. F. Heinz, "Second-Order Nonlinear Optical Effects at Surfaces," in Nonlinear surface electromagnetic phenomena (H.-E. Ponath and G. Stegeman, eds.), p. 353, North Holland, 1991.

[28] R. J. Dempsey, D. G. Davis, R. G. Buice, and R. A. Lodder, "Biological and Medical Applications of Near-Infrared Spectrometry," Applied Spectroscopy, vol. 50, pp. 18–34, Feb. 1996.

[29] O. A. Aktsipetrov, A. A. Fedyanin, E. D. Mishina, A. N. Rubtsov, C. W. V. Hasselt, and M. A. C. Devillers, "dc-electric-field-induced second-harmonic generation in Si111...-SiO 2 -Cr metal-oxide-semiconductor structures," Physical Review B, vol. 54, no. 3, pp. 1825–1832, 1996.

[30] O. A. Aktsipetrov, A. Fedyanin, A. Melnikov, E. Mishina, A. N. Rubtsov, M. H. Anderson, P. Wilson, M. ter Beek, X. Hu, J. Dadap, and M. Downer, "dc-electric-field-induced and low-frequency electromodulation second-harmonic generation spectroscopy of Si(001)-SiO2 interfaces," Physical Review B, vol. 60, pp. 8924–8938, Sept. 1999.

[31] J. Dadap, X. Hu, M. Anderson, M. Downer, J. Lowell, and O. A. Aktsipetrov, "Optical second-harmonic electroreflectance spectroscopy of a Si(001) metal-oxide-semiconductor structure," Physical Review B, vol. 53, pp. R7607–R7609, Mar. 1996.

[32] C. Lee, R. Chang, and N. Bloembergen, "Nonlinear Electroreflectance in Silicon and Silver," Physical Review Letters, vol. 18, pp. 167–170, Jan. 1967.

[33] J. G. Mihaychuk, J. Bloch, Y. Liu, and H. M. van Driel, "Time-dependent second-harmonic generation from the Si-SiO_2 interface induced by charge transfer," Optics Letters, vol. 20, p. 2063, Oct. 1995.

[34] J. Bloch, J. Mihaychuk, and H. van Driel, "Electron Photoinjection from Silicon to Ultrathin SiO2 Films via Ambient Oxygen," Physical Review Letters, vol. 77, pp. 920–923, July 1996.

[35] G. Lüpke, "Characterization of semiconductor interfaces by second-harmonic generation," Surface Science Reports, vol. 35, pp. 75–161, Nov. 1999.

[36] Z. Marka, R. Pasternak, S. Rashkeev, Y. Jiang, S. Pantelides, N. Tolk, P. Roy, and J. Kozub, "Band offsets measured by internal photoemission-induced second-harmonic generation," Physical Review B, vol. 67, p. 045302, Jan. 2003.

[37] Y. Glinka, W. Wang, S. Singh, Z. Marka, S. Rashkeev, Y. Shirokaya, R. Albridge, S. Pantelides, N. Tolk, and G. Lucovsky, "Characterization of charge-carrier dynamics in thin oxide layers on silicon by second harmonic generation," Physical Review B, vol. 65, p. 193103, Apr. 2002.

[38] V. Fomenko, E. P. Gusev, and E. Borguet, "Optical second harmonic generation studies of ultrathin high-k dielectric stacks," Journal of Applied Physics, vol. 97, no. 8, p. 083711, 2005.

[39] A. Rumpel, B. Manschwetus, G. Lilienkamp, H. Schmidt, and W. Daum, "Polarity of space charge fields in second-harmonic generation spectra of Si(100)SiO2 interfaces," Physical Review B, vol. 74, p. 081303, Aug. 2006.

[40] J. J. H. Gielis, B. Hoex, P. J. van den Oever, M. C. M. van de Sanden, and W. M. M. Kessels, "Silicon surface passivation by hot-wire CVD Si thin films studied by in situ surface spectroscopy," Thin Solid Films, vol. 517, pp. 3456–3460, Apr. 2009.

[41] J. B. Khurgin, "Current induced second harmonic generation in semiconductors," Applied Physics Letters, vol. 67, no. 8, p. 1113, 1995.

[42] T. V. Murzina, A. I. Maydykovskiy, A. V. Gavrilenko, and V. I. Gavrilenko, "Optical Second Harmonic Generation in Semiconductor Nanostructures," Physics Research International, vol. 2012, pp. 1–11, 2012.

[43] O. A. Aktsipetrov, V. O. Bessonov, A. A. Fedyanin, and V. O. Valdner, "DC-induced generation of the reflected second harmonic in silicon," JETP Letters, vol. 89, pp. 58–62, Mar. 2009.

[44] B. A. Ruzicka, L. K. Werake, G. Xu, J. B. Khurgin, E. Y. Sherman, J. Z. Wu, and H. Zhao, "Second-Harmonic Generation Induced by Electric Currents in GaAs," Physical Review Letters, vol. 108, p. 077403, Feb. 2012.

[45] L. K. Werake and H. Zhao, "Observation of second-harmonic generation induced by pure spin currents," Nature Physics, vol. 6, pp. 875–878, Aug. 2010.

[46] A. Y. Bykov, T. V. Murzina, M. G. Rybin, and E. D. Obraztsova, "Second harmonic generation in multilayer graphene induced by direct electric current," Physical Review B, vol. 85, p. 121413, Mar. 2012.

[47] Y. Q. An, F. Nelson, J. U. Lee, and A. C. Diebold, "Enhanced optical second-harmonic generation from the current-biased graphene/SiO2/Si(001) structure.," Nano letters, vol. 13, pp. 2104–9, May 2013.

[48] Y. Q. An, J. E. Rowe, D. B. Dougherty, J. U. Lee, and A. C. Diebold, "Optical second-harmonic generation induced by electric current in graphene on Si and SiC substrates," Physical Review B, vol. 89, p. 115310, Mar. 2014.

[49] M. H. . W. Akira Ueda , Richard Mu, "Semiconductor Quantum Dot Based Nanocomposite Solar Cells," in Organic Photovoltaics (N. Serdar Sariciftci and S.-S. Sun, eds.), vol. 99 of Optical Science and Engineering, ch. 14, CRC Press, Mar. 2005.

[50] M. A. Green, Solar cells: operating principles, technology, and system applications. Englewood Cliffs, NJ: Prentice-Hall, Inc., 1982.

[51] E. Yablonovitch, T. Gmitter, R. M. Swanson, and Y. H. Kwark, "A 720 mV open circuit voltage SiOx:c-Si:SiOx double heterostructure solar cell," Applied Physics Letters, vol. 47, no. 11, p. 1211, 1985.

[52] T. WANG, E. IWANICZKO, M. PAGE, D. LEVI, Y. YAN, H. BRANZ, and Q. Wang, "Effect of emitter deposition temperature on surface passivation in hot-wire chemical vapor deposited silicon heterojunction solar cells," Thin Solid Films, vol. 501, pp. 284–287, Apr. 2006.

[53] Y. Yan, M. Page, T. H. Wang, M. M. Al-Jassim, H. M. Branz, and Q. Wang, "Atomic structure and electronic properties of c-Sia-Si:H heterointerfaces," Applied Physics Letters, vol. 88, no. 12, p. 121925, 2006.

[54] S. De Wolf and M. Kondo, "Boron-doped a-Si:Hc-Si interface passivation: Degradation mechanism," Applied Physics Letters, vol. 91, no. 11, p. 112109, 2007.

[55] H. Fujiwara and M. Kondo, "Real-time monitoring and process control in amorphouscrystalline silicon heterojunction solar cells by spectroscopic ellipsometry and infrared spectroscopy," Applied Physics Letters, vol. 86, no. 3, p. 032112, 2005.

[56] L. Korte, A. Laades, and M. Schmidt, "Electronic states in a-Si:H/c-Si heterostructures," Journal of Non-Crystalline Solids, vol. 352, pp. 1217–1220, June 2006.

[57] C. W. Teplin, H. M. Branz, K. M. Jones, M. J. Romero, P. Stradins, and S. Gall, "Hot-Wire Chemical Vapor Deposition Epitaxy on Polycrystalline Silicon Seeds on Glass," MRS Proceedings, vol. 989, pp. 0989–A06–16, Feb. 2007.

[58] V. Gowrishankar, S. R. Scully, A. T. Chan, M. D. McGehee, Q. Wang, and H. M. Branz, "Exciton harvesting, charge transfer, and charge-carrier transport in amorphous-silicon nanopillar/polymer hybrid solar cells," Journal of Applied Physics, vol. 103, no. 6, p. 064511, 2008.

[59] C. W. Teplin, "Measurement of the effective surface second harmonic susceptibility tensor in sputtered air-exposed Al and Ni80Fe20 film," PhD thesis, University of Colorado at Boulder, 2002.

[60] J. E. Sipe, D. Moss, and H. van Driel, "Phenomenological theory of optical second- and third-harmonic generation from cubic centrosymmetric crystals," Physical Review B, vol. 35, pp. 1129–1141, Jan. 1987.

[61] J. E. Sipe, "New Green-function formalism for surface optics," Journal of the Optical Society of America B, vol. 4, p. 481, Apr. 1987.

[62] O. A. Aktsipetrov and A. Fedyanin, "DC electric-field-induced second-harmonic generation in Si-SiO2 multiple quantum wells," Thin solid films, vol. 294, pp. 235–237, Feb. 1997.

[63] O. A. Aktsipetrov, I. M. Baranova, K. N. Evtyukhov, T. V. Murzina, and I. V. Cherny, "Reflected second harmonic in degenerate semiconductors: nonlinear electroreflection under surface degeneracy conditions," Soviet Journal of Quantum Electronics, vol. 22, pp. 807–814, Sept. 1992.

[64] O. A. Aktsipetrov, A. A. Fedyanin, V. N. Golovkina, and T. V. Murzina, "Optical second-harmonic generation induced by a dc electric field at the SiSiO_2 interface," Optics Letters, vol. 19, p. 1450, Sept. 1994.

[65] O. A. Aktsipetrov, I. M. Baranova, L. V. Grigor'eva, K. N. Evtyukhov, E. D. Mishina, T. V. Murzina, and I. V. Cherny, "Second harmonic generation at a semiconductorelectrolyte interface and investigation of the surface of silicon by the nonlinear electroreflection method," Soviet Journal of Quantum Electronics, vol. 21, pp. 854–859, Aug. 1991.

[66] J. J. H. Gielis, B. Hoex, M. C. M. van de Sanden, and W. M. M. Kessels, "Negative charge and charging dynamics in Al[sub 2]O[sub 3] films on Si characterized by second-harmonic generation," Journal of Applied Physics, vol. 104, no. 7, p. 073701, 2008.

[67] Y. Q. An and S. T. Cundiff, "Bulk and surface contributions to resonant second-harmonic generation from Si(001) surfaces," Applied Physics Letters, vol. 81, no. 27, p. 5174, 2002.

[68] R. A. Street, Hydrogenated Amorphous Silicon. Cambridge University Press, 1991.

[69] S. M. Sze, Physics of the semiconductor. Wiley, New York, 2 ed., 1981.

[70] S. Montanari, "Fabrication and characterization of planar Gunn diodes for Monolithic Microwave Integrated Circuits," PhD thesis, RWTH Aachen University, 2004.

[71] D. A. Neamen, Semiconductor Physics and Devices. Irwin Book Team: Irwin Professional Publishing, 1992.

[72] A. S. Ferlauto, G. M. Ferreira, J. M. Pearce, C. R. Wronski, R. W. Collins, X. Deng, and G. Ganguly, "Analytical model for the optical functions of amorphous semiconductors from the near-infrared to ultraviolet: Applications in thin film photovoltaics," Journal of Applied Physics, vol. 92, no. 5, p. 2424, 2002.

[73] C. Ohlhoff, G. Lüpke, C. Meyer, and H. Kurz, "Static and high-frequency electric fields in silicon MOS and MS structures probed by optical second-harmonic generation," Physical Review B, vol. 55, pp. 4596–4606, Feb. 1997.

[74] J. D. Walker, "Artificial Surface Mounted Rotor Systems: Experimental studies using surface second harmonic generation," PhD thesis, University of Colorado at Boulder, 2007.

[75] S. Chandrasekhar, Radiative Transfer. New York: Dover Publications, 1960.

[76] C. W. Teplin and C. Rogers, "Experimental example of isotropic surface second-harmonic generation: dc-sputtered air-exposed aluminum thin films," Physical Review B, vol. 65, p. 245408, May 2002.

[77] D. Krause, C. W. Teplin, and C. T. Rogers, "Optical surface second harmonic measurements of isotropic thin-film metals: Gold, silver, copper, aluminum, and tantalum," Journal of Applied Physics, vol. 96, no. 7, p. 3626, 2004.

[78] Q. Wang, M. Page, E. Iwaniczko, Y. Xu, L. Roybal, R. Bauer, B. To, H. Yuan, A. Duda, and Y. Yan, "Crystal silicon heterojunction solar cells by hot-wire CVD," in 2008 33rd IEEE Photovolatic Specialists Conference, pp. 1–5, IEEE, May 2008.

[79] Q. Wang, M. R. Page, E. Iwaniczko, Y. Xu, L. Roybal, R. Bauer, B. To, H.-C. Yuan, A. Duda, F. Hasoon, Y. F. Yan, D. Levi, D. Meier, H. M. Branz, and T. H. Wang, "Efficient heterojunction solar cells on p-type crystal silicon wafers," Applied Physics Letters, vol. 96, no. 1, p. 013507, 2010.

[80] Q. Wang, "High-efficiency hydrogenated amorphous/crystalline Si heterojunction solar cells," Philosophical Magazine, vol. 89, pp. 2587–2598, Oct. 2009.

[81] A. Kanevce and W. K. Metzger, "The role of amorphous silicon and tunneling in heterojunction with intrinsic thin layer (HIT) solar cells," Journal of Applied Physics, vol. 105, no. 9, p. 094507, 2009.

[82] Y. Q. An and S. Cundiff, "Phase inversion in rotational anisotropy of second harmonic generation at Si(001) interfaces," Physical Review B, vol. 67, p. 193302, May 2003.

[83] R. Könenkamp, S. Muramatsu, H. Itoh, S. Matsubara, and T. Shimada, "Determination of electric field profiles in amorphous silicon solar cells," Applied Physics Letters, vol. 57, no. 5, p. 478, 1990.

[84] R. Könenkamp, S. Muramatsu, S. Matsubara, and T. Shimada, "Space-charge distribution and trapping kinetics in amorphous silicon solar cells," Applied Physics Letters, vol. 60, no. 9, p. 1120, 1992.

[85] T. Tiedje, C. Wronski, B. Abeles, and J. Cebulka, "Electron transport in hydrogenated amorphous silicon: drift mobility and junction capacitance," Solar Cells, vol. 2, pp. 301–318, Nov. 1980.

[86] J. Cohen, D. Lang, and J. Harbison, "Direct Measurement of the Bulk Density of Gap States in n-Type Hydrogenated Amorphous Silicon," Physical Review Letters, vol. 45, pp. 197–200, July 1980.

[87] R. A. Abram and P. J. Doherty, "A theory of capacitance-voltage measurements on amorphous silicon Schottky barriers," Philosophical Magazine Part B, vol. 45, pp. 167–176, Feb. 1982.

[88] C. E. Michelson, A. V. Gelatos, and J. D. Cohen, "Drive-level capacitance profiling: Its application to determining gap state densities in hydrogenated amorphous silicon films," Applied Physics Letters, vol. 47, no. 4, p. 412, 1985.

[89] A. Rolland, "Electrical Properties of Amorphous Silicon Transistors and MIS-Devices: Comparative Study of Top Nitride and Bottom Nitride Configurations," Journal of The Electrochemical Society, vol. 140, no. 12, p. 3679, 1993.

[90] J. P. Kleider and D. Mencaraglia, "Theoretical study of the quasistatic capacitance of metal-insulatorsemiconductor structures in amorphous semiconductors," Journal of Applied Physics, vol. 78, no. 6, p. 3857, 1995.

Appendix A

Cr/a-Si:H/ITO sample

In order to study the ITO influence on the total SHG signal, we fabricated a Cr/a-Si:H/ITO sample to compare with the ITO/a-Si:H/ITO trilayer sample. Cr is a material that is often used in EFISH studies of c-Si. The super thin Cr film could provide relative good transparency for pump laser (820nm) and SHG photons (410nm), allowing EFISH photons from a-Si:H bulk to escape. Cr film produce low intensity SHG at this wavelength, thus this device produce very low SHG background signal. At the same time, it provide conductivity allowing external bias been applied on a-Si:H bulk.

The thickness of Cr film on the a-Si:H is important and needs to be carefully selected. If the Cr film is too thick, it heavily absorbs 410nm photons, hence reduce the EFISH signals. On the opposite, if Cr film is too thin, it can induce large resistance in series with a-Si:H which reduce the percentage of voltage drop across a-Si:H out of the applied bias, as a result reducing the EFISH signal. Before depositing the Cr film on the a-Si:H device, we deposited various thickness of Cr films on glass wafers to study conductivity and SHG production at different thickness.

We use Chemical Vapor Deposition(CVD) to deposit Cr thin film on glass wafer. The deposition process is undertaken in the "MARK" vacuum system. This is two stage vacuum system. Before the first vacuum stage, I mount the glass wafer in the chamber and seal the chamber. After depleting the air in the mechanical pump with liquid nitrogen, I proceed to the first vacuum stage. I use the mechanical pump to decrease the chamber pressure down to 100 mTorr. Then I disconnect the champer from mechanical pump, and open the vent for diffusion pump and turn on the ion

gauge. When the chamber pressure drops to 2×10^{-6} Torr, I open the vapor shutter right below the sample, and turn on the high voltage on filament to evaporate the Cr pellet. I slowly increase the current to slowly melt and evaporate Cr pellet, and increase the Cr film grow rate until the thickness monitor indicates a steady growth rate of 2-3Å/sec. The vapor is closed when the Cr film reaches objective thickness. Then, I turn off the filament heating, and wait 10 minute for the Cr vapor completely cooling down before shutting down the vacuum pump and finishing the whole deposition process.

Three Cr/glass samples are fabricated with respective 5, 10 and 15 nm thickness of Cr film. The resistance for Cr films is measured by two point method with two electrodes 2 cm apart. The measured resistance for each sample are 7000 ohm for 5 nm Cr film, 3000 ohm for 10 nm, 1700 nm for 15 nm. The 700 nm a-Si:H film has a resistance around 10,000 ohm. After pondering on Cr film resistance and transparence, the film thickness is determined to be 8 nm. We follow the same routine above, deposited 8 nm Cr film on the semi-manufactured ITO/a-Si:H sample. The Cr/a-Si:H interface will form a metal/semiconductor junction similar to ITO/a-Si:H interface. Figure A.3 shows the JV curve for this sample, and it shows similar back-to-back diode behavior.

The "SHG vs Bias" and Input Polarization Scan are performed for this sample under similar laser intensity. The result shows that SHG counts for zero and forward bias condition is below the background count. Only the pP SHG intensity under reverse bias is above the dark background photon counts. Figure A.4 displays the SHG intensity vs bias sweep. In the forward bias region($V_A > 0$), the idler SHG intensity is in distinguishable from background noise. In the reverse bias region, the EFISH signal in linear relationship with bias magnitude. This similar linearity as in ITO/a-Si:H/ITO strongly suggests that V_A-dependent SHG from the top ITO surface does not contribute significantly to the fitted response.

Figure A.1: shows picture of fabricated Cr/Glass samples. From left to right, Cr film thickness is 5nm, 10nm, 15nm. The color of the film become darker as film thickness increases.

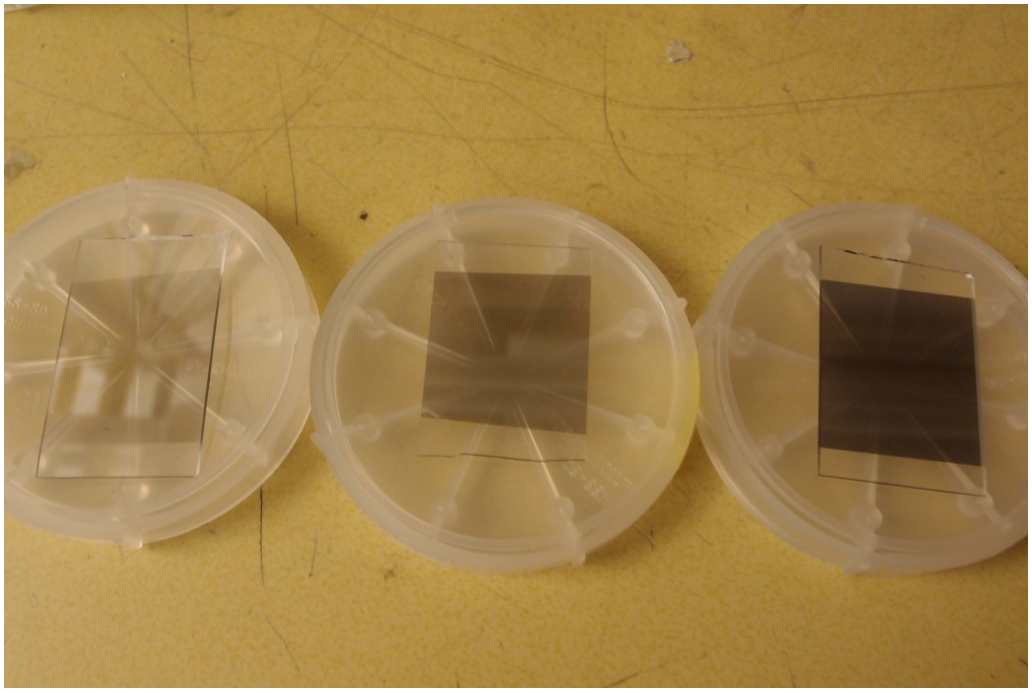

Figure A.2: shows picture of fabricated Cr/a-Si:H/ITO/sample. The device is based on a silica wafer, with ITO and a-Si:H layer deposited on top. The brown area is a-Si:H film, while top left corner exposes the bottom ITO layer for electric contact. The dark square in the central area is Cr thin film deposited on on a-Si:H layer. The thickness configuration for different layers is Cr(8nm)/a-Si:H(300nm)/ITO(40nm)

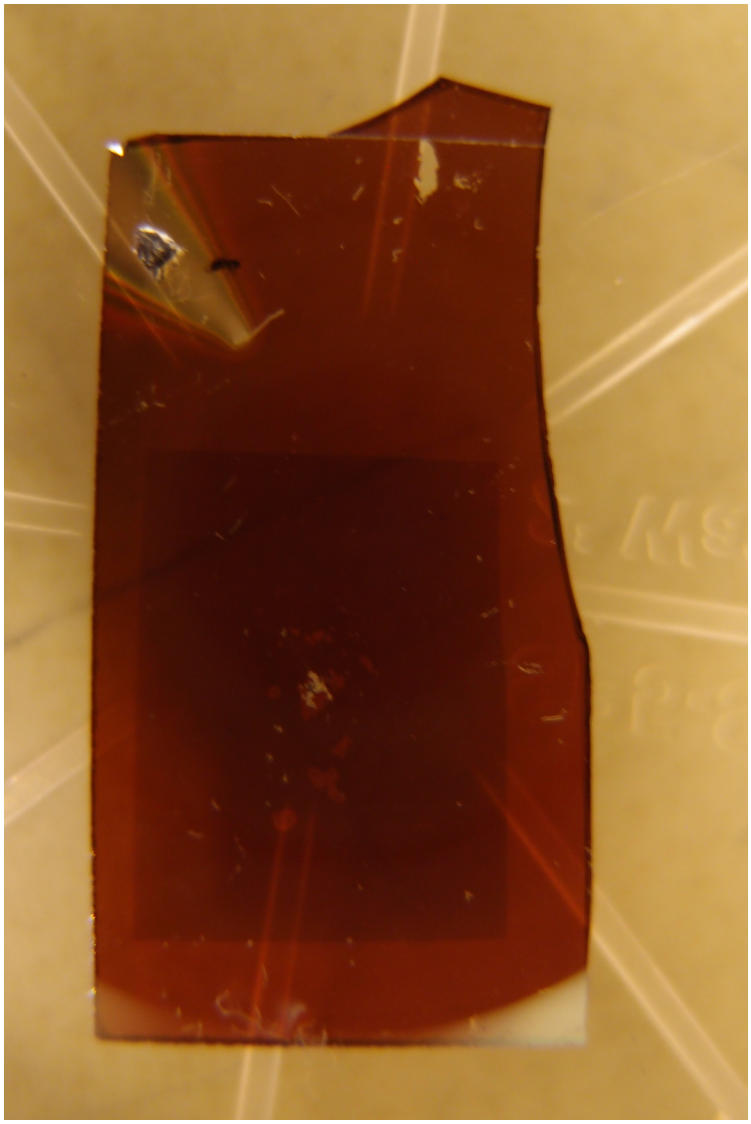

Figure A.3: shows measured JV curve on Cr/a-Si:H/ITO sample. This JV curve obeys back-to-back diode behavior.

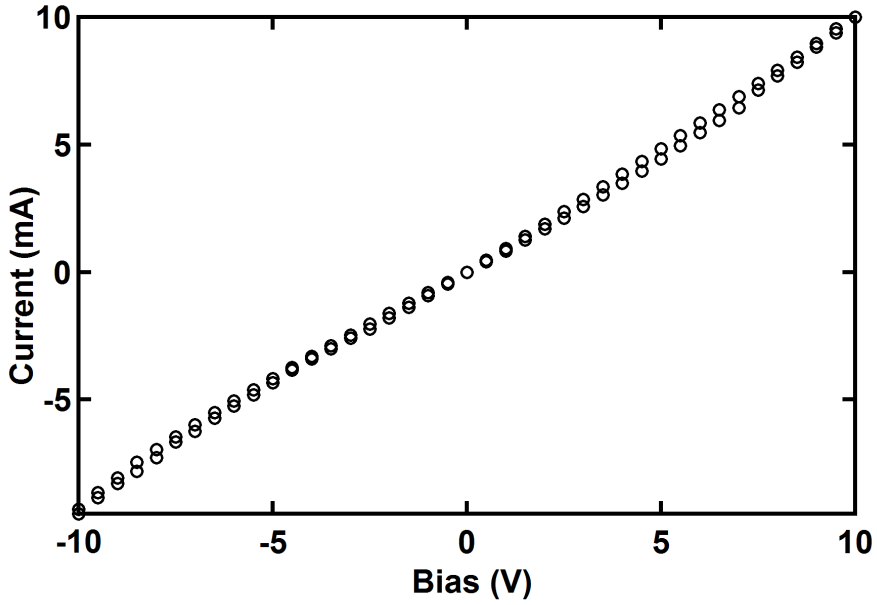

Figure A.4: shows SHG intensity of pP geometry vs bias. It clearly indicate the linear SHG relationship in the reverse bias region. The open circles with errors bar are the SHG intensity data; the solid line is the fitting curve for pP SHG according to Equation (4.2)

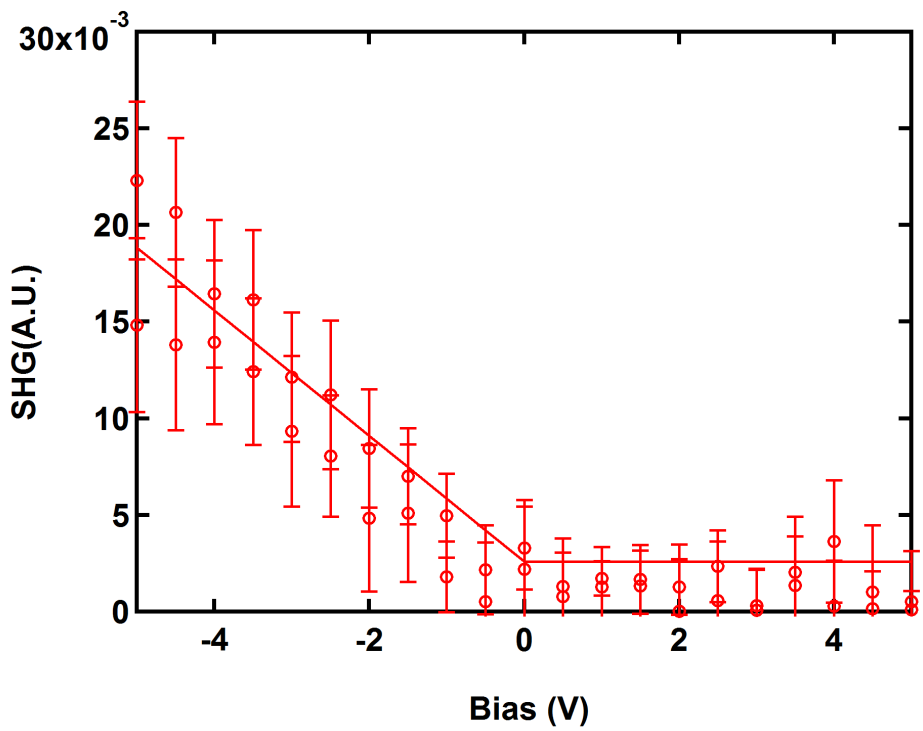

Appendix B

More ITO/a-Si:H/ITO samples

In Chapter 4, I have describe the interference theory for quantitatively understanding the SHG data from ITO/a-Si:H/ITO tri-layer device. In this appendix, I show more SHG data from different tri-layer devices, and demonstrate the ability for the interference theory to explain various SHG data.

As shown in Figure 4.2, 4 X 4 circular trilayer samples are fabricated on silica wafer. For sample type B with 70 nm thick top ITO layer, the SHG data from each of particular circular trilayer device show different interference pattern, due to slightly different roughness and thickness of the top ITO layer. Meanwhile, those different patterns can still be quantitatively explained by SSHG and EFISH interference theory presented in Chapter 4. Each individual device is labelled with "XnYm" rule, while "n, m" are number to mark the device location on the mesa by counting from the top left corner. "X" represents the column number and "Y" represents the row number. For example, "X1Y2" is the first device on the second row. In the following diagrams, I show the "SHG vs Bias" data from four different devices on the wafer and the corresponding fitted curves.

Figure B.1: Second harmonic intensity in upper panel, relative phase in mid panel, and current in bottom panel as a function of applied bias voltage. In upper panel, the SHG intensity is shown for different input laser polarizations: red circles: pP, blue squares: sP, green point-up triangles: $mixP$, black point-down triangles: $mixS$. Mid panel shows the phase difference between the mixP and mixS SHG signal. Bottom panel shows the I-V curves. Solid lines are fits to Equations (4.2) to (4.4), as described in the text. The resulting fit parameters are listed in Table B.1. The increasing SHG signal for $V_A > 5$V cannot be explained by the physics underlying the fit equations and so is not fitted.

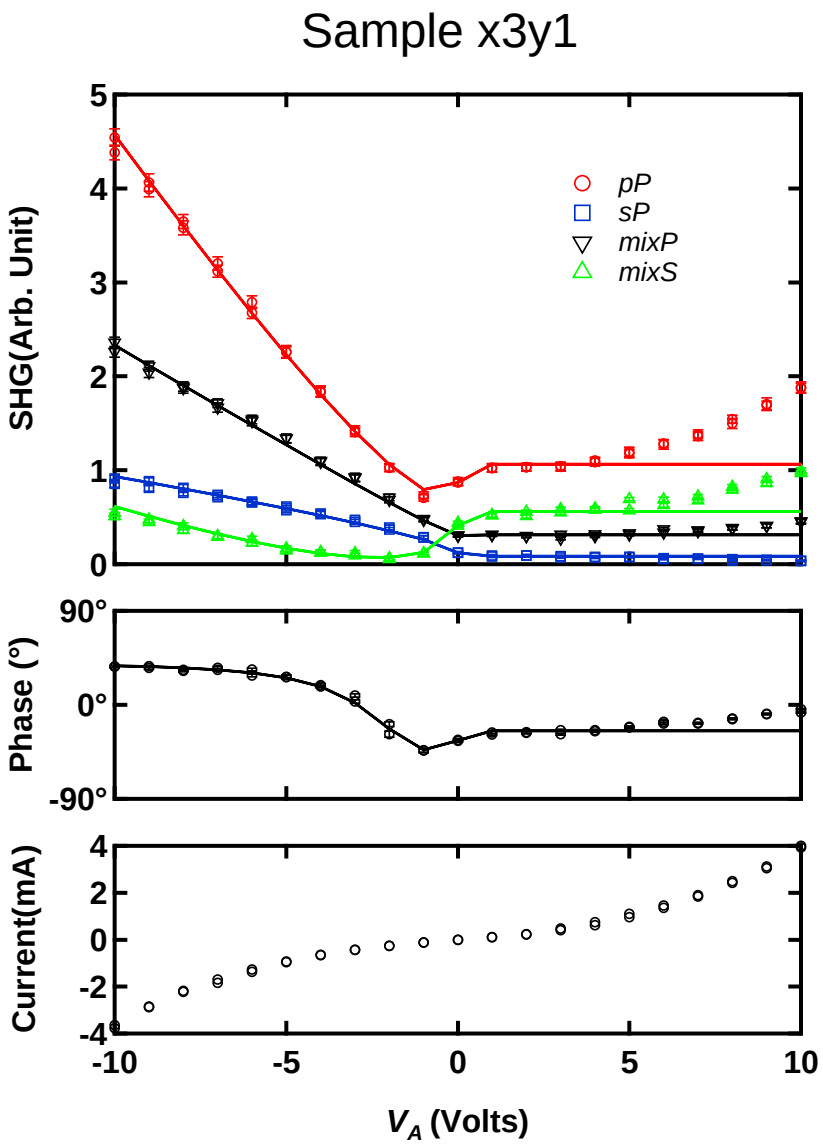

Figure B.2: Second harmonic intensity in upper panel, relative phase in mid panel, and current in bottom panel as a function of applied bias voltage. In upper panel, the SHG intensity is shown for different input laser polarizations: red circles: pP, blue squares: sP, green point-up triangles: $mixP$, black point-down triangles: $mixS$. Mid panel shows the phase difference between the mixP and mixS SHG signal. Bottom panel shows the I-V curves. Solid lines are fits to Equations (4.2) to (4.4), as described in the text. The resulting fit parameters are listed in Table B.1. The increasing SHG signal for $V_A > 2$V cannot be explained by the physics underlying the fit equations and so is not fitted.

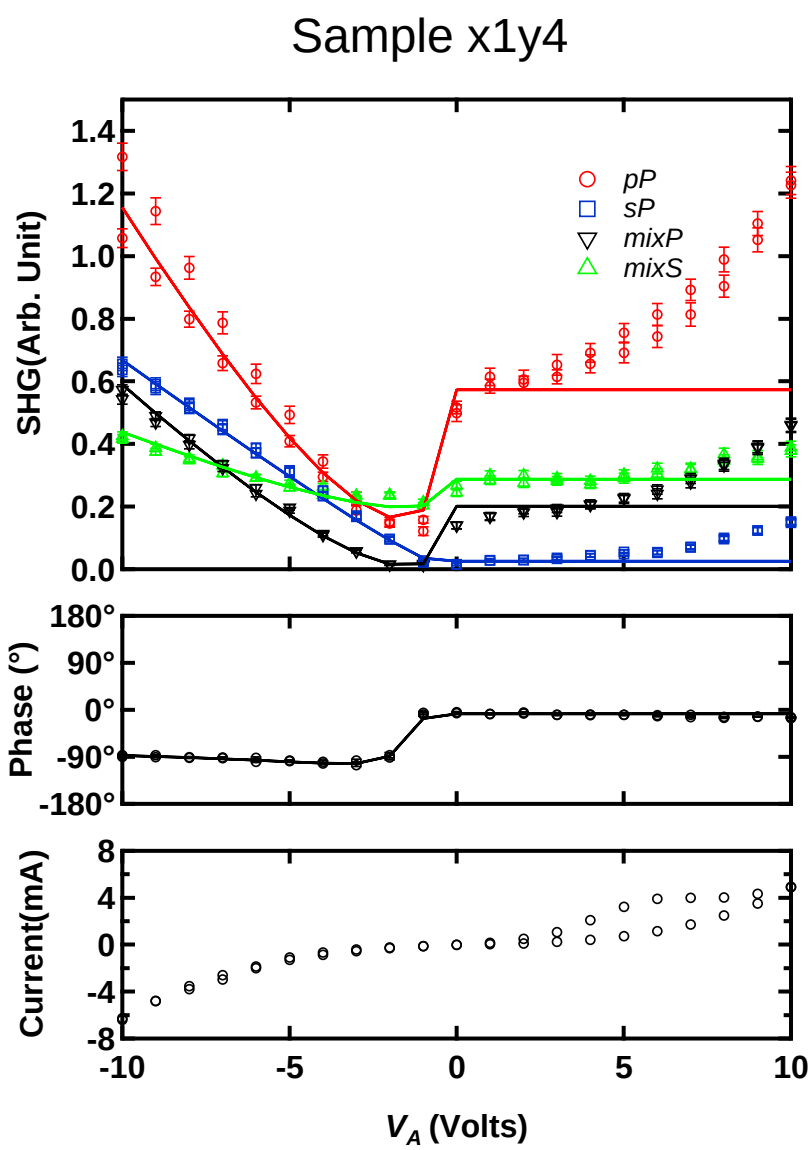

Figure B.3: Second harmonic intensity in upper panel, relative phase in mid panel, and current in bottom panel as a function of applied bias voltage. In upper panel, the SHG intensity is shown for different input laser polarizations: red circles: pP, blue squares: sP, green point-up triangles: $mixP$, black point-down triangles: $mixS$. Mid panel shows the phase difference between the mixP and mixS SHG signal. Bottom panel shows the I-V curves. Solid lines are fits to Equations (4.2) to (4.4), as described in the text. The resulting fit parameters are listed in Table B.1. The increasing SHG signal for $V_A > 5$V cannot be explained by the physics underlying the fit equations and so is not fitted.

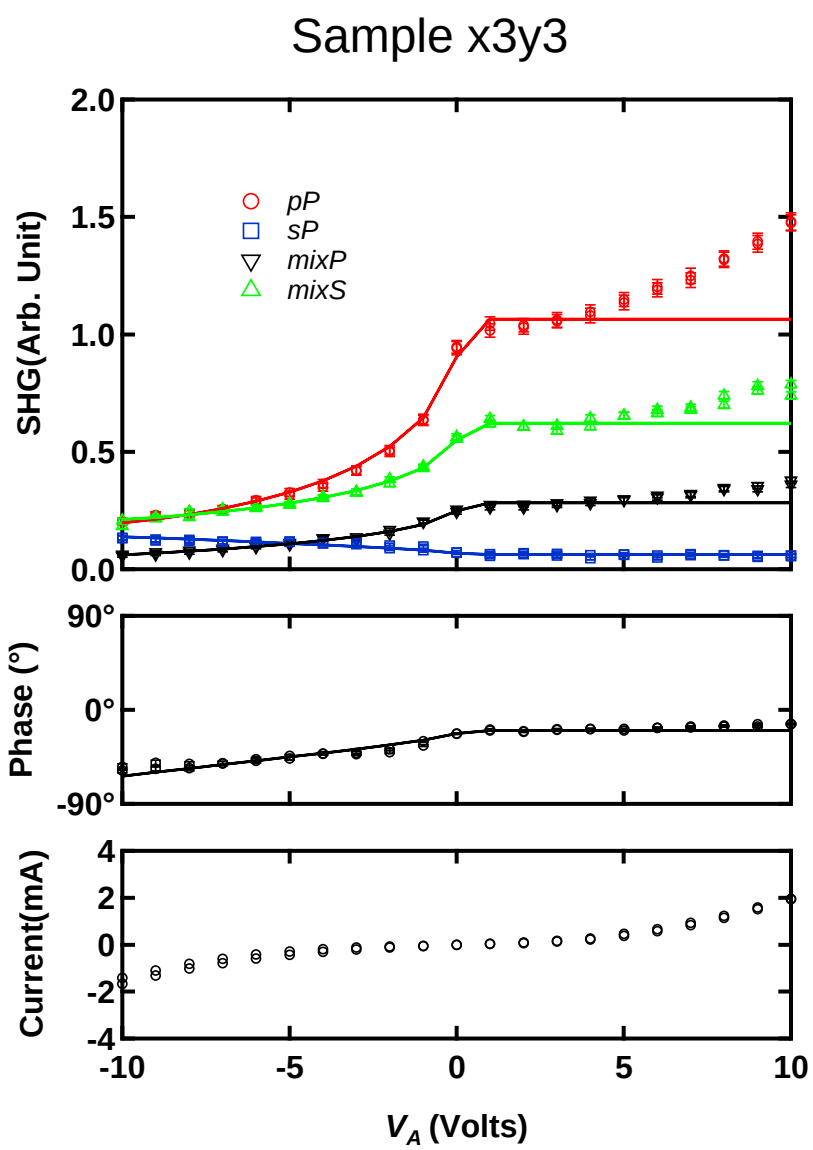

Figure B.4: Second harmonic intensity in upper panel, relative phase in mid panel, and current in bottom panel as a function of applied bias voltage. In upper panel, the SHG intensity is shown for different input laser polarizations: red circles: pP, blue squares: sP, green point-up triangles: $mixP$, black point-down triangles: $mixS$. Mid panel shows the phase difference between the mixP and mixS SHG signal. Bottom panel shows the I-V curves. Solid lines are fits to Equations (4.2) to (4.4), as described in the text. The resulting fit parameters are listed in Table B.1.

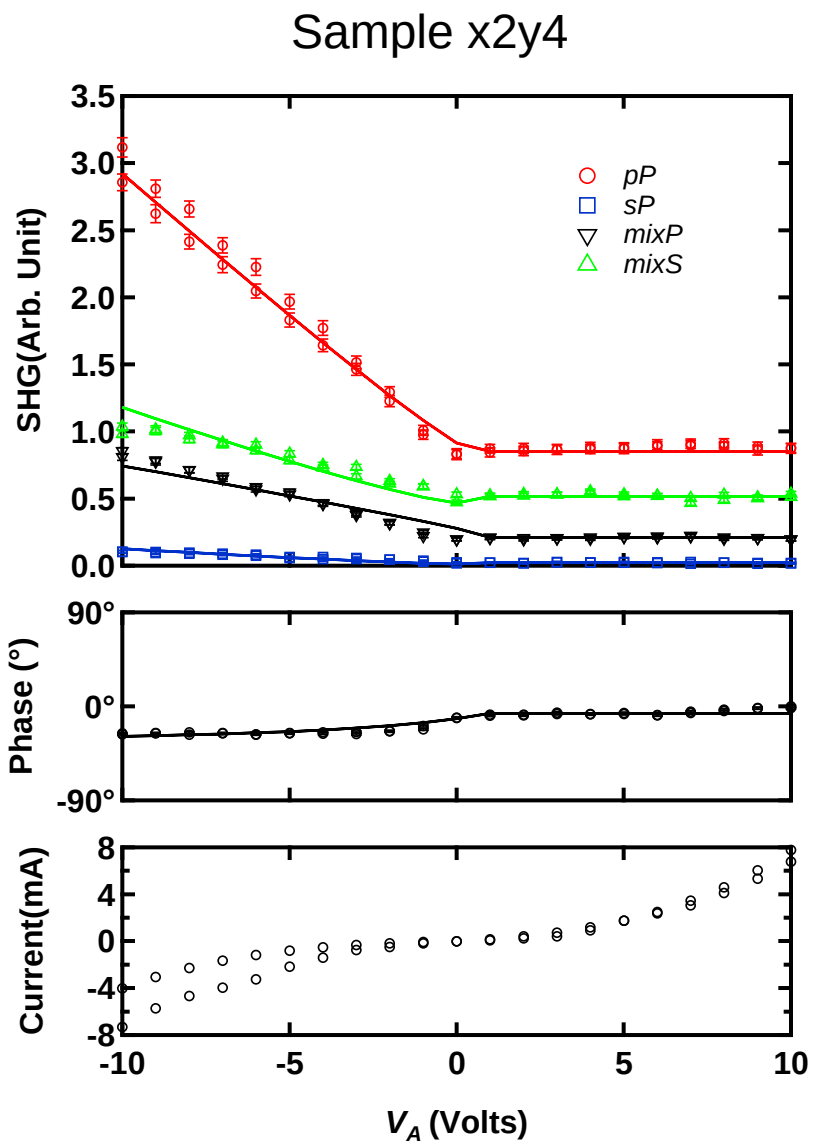

Table B.1: Resulting fit parameters from least squares fitting of the SHG data to Equations (4.2) to (4.4). The solid lines in Figures B.1 to B.4 show the fit results.

	Parameter	Sample X3Y1	Sample X1Y4
Magnitude(arb. unit) / Phase(Degree)	$\overrightarrow{pP}_{idler}$	1.030 ± 0.006 / 0 °	0.7564 ± 0.0043 / 0 °
	$\boldsymbol{\overrightarrow{pP}_{EFISH}}$	**0.799 ± 0.006 / -124.0 °±0.7 °**	**0.5223 ± 0.0029 / -148.0 ° ± 0.5 °**
	$\overrightarrow{SP}_{idler}$	0.2872 ± 0.0044 / -81.4 °±2.2 °	0.1574 ± 0.0041 / 31.1 ° ± 4.1 °
	$\boldsymbol{\overrightarrow{SP}_{EFISH}}$	**0.2139 ± 0.0027 / -76.4 °±4.2 °**	**0.2956 ± 0.0027 / 169.1 ° ± 1.5 °**
	$\overrightarrow{mixS}_{idler}$	0.7473 ± 0.0039 / 10.08 °±0.42 °	0.5351 ± 0.0036 / 12.8 ° ± 0.7 °
	$\boldsymbol{\overrightarrow{mixS}_{EFISH}}$	**0.4540 ± 0.0030 / -150.0 °±0.5 °**	**0.2519 ± 0.0025 / -111.3 ° ± 0.8 °**
V_{BI} (V)		0.0669 ± 0.008	0.164 ± 0.032

	Parameter	Sample X3Y3	Sample X2Y4
Magnitude(arb. unit) / Phase(Degree)	$\overrightarrow{pP}_{idler}$	1.0315 ± 0.0042 / 0 °	0.9220 ± 0.0041 / 0 °
	$\boldsymbol{\overrightarrow{pP}_{EFISH}}$	**0.239 ± 0.005 / -157.0 °±0.8 °**	**0.492 ± 0.006 / 101.3 ° ± 1.3 °**
	$\overrightarrow{SP}_{idler}$	0.2481 ± 0.0041 / 90 °±1.6 °	0.1407 ± 0.0035 / 98.7 ° ± 2.8 °
	$\boldsymbol{\overrightarrow{SP}_{EFISH}}$	**0.0568 ± 0.0038 / 28.4 °±4.1 °**	**0.1338 ± 0.0026 / -40.0 ° ± 1.9 °**
	$\overrightarrow{mixS}_{idler}$	0.7880 ± 0.0026 / 33.34 °±0.30 °	0.7173 ± 0.0027 / 15.46 ° ± 0.29 °
	$\boldsymbol{\overrightarrow{mixS}_{EFISH}}$	**0.153 ± 0.005 / 180.9 °±1.2 °**	**0.327 ± 0.0045 / 124.8 ° ± 1.1 °**
V_{BI} (V)		0.137 ± 0.022	0.99 ± 0.12

Appendix C

Code for Fitting functions

In this appendix, I present the actual code for the fitting functions introduced in the main text with in the Igor programming environment.

C.1 Stokes Fitting Function

The derivation of this fitting function is given in section 2.2.1. The following code is the major structure of the fitting function to be compiled in the procedure window. The actual fitting function will be available to use in the "Curve Fitting" tools window.

```
Function StokesFit_General(w,x) : FitFunc
Wave w; Variable x

Wave polarizer
polarizer={{.5,.5,0,0},{.5,.5,0,0},{0,0,0,0},{0,0,0,0}}
Wave SH_Beam
SH_beam={w[3]+sqrt(w[0]^2 + w[1]^2 + w[2]^2),w[0],w[1],w[2]}
Variable pos=4*pi*(x-w[4])

Wave QWPlate,QWRot,QWRotBack,LPRot,LPRotBack
QWPlate={{1,0,0,0},{0,1,0,0},{0,0,cos(w[5]),sin(w[5])},
```

```
            {0,0,-sin(w[5]),cos(w[5])}}
    //waveplate of retardance w_5, algined with fast axis parallel to p
QWRot={{1,0,0,0},{0,cos(pos),-sin(pos),0},
            {0,sin(pos),cos(pos),0},{0,0,0,1}}
QWRotBack={{1,0,0,0},{0,cos(-pos),-sin(-pos),0},
                {0,sin(-pos),cos(-pos),0},{0,0,0,1}}

LPRot={{1,0,0,0},{0,cos(w[6]),-sin(w[6]),0},
            {0,sin(w[6]),cos(w[6]),0},{0,0,0,1}}
LPRotBack={{1,0,0,0},{0,cos(-w[6]),-sin(-w[6]),0},
            {0,sin(-w[6]),cos(-w[6]),0},{0,0,0,1}}

MatrixOp/o endwave = LPRotBack x polarizer x LPRot
                        x QWRotBack x QWPlate x QWRot x SH_beam

Wave endwave
Return endwave[0]
//w0 is not the true Stokes S0.  instead S0=w0+sqrt(s1^2+s2^2+s3^2)
//S0: unpolarized, S1: PS coordinate,
    //S2: 45/-45 coordiante, S3: RCP.LCP coordinate
// w4: QWP offset
// w5: QWP retardance
//w6: LP position
End
```

C.2 Idler SSHG and EFISH interference theory

This fitting function is designed to separate the idle SSHG and EFISH signal by fitting the p, s state SHG and their relative phase at different input polarization state over a large bias range. The detailed mathematical description is introduced in section 4.2. This fitting function is designed as multi-variant function, needs four column variable corresponding to each data points to feed in. They are voltage bias, input polarization angle, data type indicator and data duplicate of SHG data. The SHG data array contains p, s state intensity and their relative phase. The data type indicator is set to 0 for p intensity, 1 for s intensity, 2 for the relative phase. The original data array is also feeded into the fitting functions. Only the relative phase is utilized to help the fitted phase term to select the right quadrant for minimizing error.

```
Function Idler_EFISH_Fit_general_c (w,x,y,z, dataCopy): FitFunc

Wave w
Variable x,y,z, dataCopy
y=y-w[12]
//w holds the parameters: w[0]=pP_Idler, w[1]=pP_EFISH, w[2]=pP_EFISH_phase
//w[3]=sP_Idler, w[4]=sP_Idler_phase,w[5]=sP_EFISH, w[5]=sP_EFSH
//w[6]=sP_EFISH_Phase, w[7]=mixS_Idler, w[8]=mixS_Idler_Phase
//w[9]=mixS_EFISH, w[10]=mixS_EFISH_phase, w[11]= built-in potential
//all the phase terms are referred to the pP idler in radians
//z will be 0 for the P intensity,  1 for S intensity , 2 for Delta(P-S)
//x will be voltage,  y will be input polarization angle in degree
//dataCopy is the duplicate of fit_data,
//it helps quadrant selection for phase term
```

```
variable/c E_P, E_S, E_pP, E_sP, E_mixS
E_pP = cmplx(w[0],0)    // pP Idler part
E_pP = E_pP+sqrt((x-w[11])*-1*((x-w[11])<0))*w[1]*cmplx(cos(w[2]),sin(w[2]))
                                                        //pP Idler + EFISH

E_sP =cmplx(w[3],0) * cmplx( cos(w[4]), sin(w[4]))    // sP Idler part
E_sP =E_sP+sqrt((x-w[11])*-1*((x-w[11])<0))*w[5]*cmplx(cos(w[6]),sin(w[6]))
                                                        //sP Idler + EFISH

E_P =(E_pP *cos(pi*y/180)^2 + E_sP * sin(pi*y/180)^2) // y is in degree

E_mixS =cmplx(w[7],0) * cmplx(cos(w[8]), sin(w[8])) // mixS Idler part
E_mixS =E_mixS
        +sqrt((x-w[11])*-1*((x-w[11])<0))*w[9]*cmplx(cos(w[10]),sin(w[10]))
                                                        // mixS EFISH part

E_S = E_mixS * 2 * cos(pi*y/180) * sin(pi*y/180)
//the 2 factor is intented for renormalize to E_mixS signal strength.

Variable result

Switch(z)
case 0:
result=magsqr(E_P)
break
case 1:
result=magsqr(E_S)
```

```
break
case 2:
If(magsqr(E_P*E_S) ==0)
result=0
else
result=imag(r2polar( E_P/E_S))
IF( abs(dataCopy-result) > pi )
result= result+sign(dataCopy-result)*2*pi
ENDIF
ENDIF
break
EndSwitch

Return result
END
```

C.3 Coupled Temporal Ordinary Differential Equation Fitting for Electrical Circuit

This following code is to realize the fitting function by numerically solving the temporal coupled ordinary differential equation (ODE). For the circuit model introduced in section 5.2, the electric response driven by arbitrary voltage wave is governed by ODEs described in section 5.3. We drive this circuit with imperfect square wave and measure the resulting current through the circuit. The current wave are fitted to determine the component values (resistance, capacitance) in the circuit. By solving the ODEs at each combination of circuit component values, the simulated current wave is generated and compared with the actual measured current data. By minimizing

the difference between the current solution and data, the circuit component values are optimized to explain the current data.

The following code contains two functional parts. The first part is to design the algorithm for solving ODEs. The second part is the actual fitting function. The reader should be careful to notice this fitting function uses the technique of "All-At-Once" provided by Igor. The details for this technique can be found in the manuals for Igor programming. When using this fitting function, it is important to setup the "Epsilon" column. This column can set the minimum gap for Levenberg-Marquardt algorithm to calculate the fitting error's derivative in the parameter space. Because the error profile in the parameter space for numerically solved current solution can be a very rough bowl with countless local minimum, it is necessary to avoid the fitting process being trapped by local minimum. The "Epsilon" column allows the fitting function to ignore the small pits in the parameter space. The relative large jump step size for the fitted parameter helps the fitting function to find the global error minimum in parameter space.

```
Function CircuitModel(pw, tt, yy, dydt)
Wave pw         // pw[0]=r0fit, pw[1]=r1fit
// pw[2]=c1fit, pw[3]=c2fit, pw[4]=vOffset
Variable tt
Wave yy // yy[0] = curr0, yy[1] = curr1
Wave dydt
Variable timestep=0.008


Wave voltData
Variable index = floor((tt-5)/timestep)
Variable volt = voltData[index]


//curr00'[t]==(voltageFunc[t] - curr00[t]*(50+r0fit)
```

```
//                 - curr11[t]*r1Fit)/(50*c2Fit/10^6*r0Fit)
//(curr00[t] + 50*c2Fit/10^6*curr00'[t]) ==
//                  (curr11[t] + r1Fit*c1Fit/10^6*curr11'[t]
dydt[0] =(volt- yy[0]*(pw[0]+pw[1]) - pw[0]*yy[1])/(pw[0]*pw[1]*pw[3]/10^6)
dydt[1] = dydt[0]*pw[1]/pw[2] - yy[1]/pw[2]/(pw[4]/10^6)

return 0
End
```

```
Function Circuit_ODE_Fit(pw, yw, xw) : FitFunc
Wave pw // normal fit coefficient wave    pw[0]=r0fit, pw[1]=r1fit
// pw[2]=c1fit, pw[3]=c2fit   pw[5]=voltOffset
Wave yw // output- the model results
Wave xw // input- data X values (may also be available from X scaling of yw)
Wave voltData
Wave Time_us
Make/n=(5000,2)/d/o temp
temp[0][0] = (voltData[0])/(pw[0]+pw[1])
                              // setting initial condition for integration
temp[0][1]=  0             //temp[0][0]

IntegrateODE /X=Time_us/M=1 CircuitModel, pw, temp
                       //selected integration function for "all at once" fitting
yw[0,4999]= (voltData[p] - temp[p][0]*pw[1] ) / (pw[0])*50 +pw[5]
                        // Current Fitting
```

```
yw[5000, 9999]= (temp[p-5000][0]*pw[1] - temp[p-5000][1]*pw[2]) * pw[6] +pw[7]
                        // SHG fitting from the voltage of C3
End
```